A Metastable Modular Structure Approach for Shape Morphing, Property Tuning and Wave Propagation Tailoring

by

Zhen Wu

A dissertation submitted in partial fulfillment
of the requirements for the degree of
Doctor of Philosophy
(Mechanical Engineering)
in the University of Michigan

2018

Doctoral Committee:

Professor Kon-Well Wang, Chair
Professor Carlos E. Cesnik
Professor Bogdan Epureanu
Professor Noel Perkins
Assistant Professor Bogdan Popa

Zhen Wu

wuzhen@umich.edu

ORCID iD: 0000-0002-8125-2407

Dedication

Dedicated to Jianping Wang and Chaoxing Wu, whose unconditional love and unwavering support will forever provide courage and strength

Acknowledgements

I would like to take this opportunity to thank those who have made this thesis possible.

I wish to thank several members of the faculty here at the University of Michigan. First and foremost, I would like to extend my gratitude to my advisor and mentor, Professor Kon-Well Wang. His continual support and guidance in both academic and life during the past few years has provided an excellent environment for me to mature as a better researcher as well as a better person, and for this I shall remain exceedingly grateful. I would also like to thank the members of my doctoral committee for their time and support during this exciting phase of my educational experience.

My family and friends have provided immeasurable support over the years, and to them I extend my deepest gratitude. Without the love, support, joy and excitement brought by them, I would not have been able to make it to this point. I would especially like to extend my gratitude to my parents who not only provided encouragement during this work, but also provided a refuge when I just had to get away, and to my roommate and best friend Yi Chen for his continuing encouragement and accompanying.

During the past few years at the University of Michigan, I have been rewarded with great opportunity to work with many smart people. In this regard, I would like to acknowledge my current and former Labmates and colleagues. Moreover, I would like to extend special thanks to Dr. Fabio Semperlotti, Dr. Harne Ryan, Dr. Hongbin Fang and Dr. Suyi Li for imparting their knowledge and expertise on many of the insightful discussions and suggestions.

Without financial support, I would not have been able to accomplish this research. Therefore, I would like to thank the Defense Advanced Research Projects Agency (DARPA), Air Force Office of Scientific Research (AFOSR) and Army Research Office (ARO) for their supports. I would also like to thank the Department of Mechanical Engineering and the College of Engineering at the University of Michigan for providing financial support.

Table of Contents

List of Figures

Abstract

The emerging concept of reconfigurable mechanical metamaterials has received increasing attention for realizing future advanced multifunctional adaptive structural systems partially due to their advantages over conventional bulk materials that are beneficial and desirable in many engineering applications. However, some of the critical challenges remain unaddressed before the concept can effectively and efficiently achieve real-world impacts. For instance, in the state-of-art, modules of mechanical metamaterials only reconfigure collectively to achieve global topology adaptation. As a result, the structure merely exhibits limited number of configurations that are discretely different from each other, which greatly undermines the benefits and impact of the reconfiguration effect. Additionally, most of the metamaterials investigations are focusing on the "materials" characteristics assuming infinite domain without considering the "structure" aspect of the systems. The effects of having finite domains and boundary conditions will generate new research issues and phenomena that are critical to real-world systems.

To address the challenges and fundamentally advance the state of the art of multifunctional adaptive structures, this dissertation seeks to create a paradigm shift by exploiting and harnessing metastable modular mechanics and dynamics. Through developing new analysis and synthesis methodologies and conducting rigorous analytical, numerical, and experimental investigations, this research creates a new class of reconfigurable metastructure that can achieve mechanical property and topology adaptation as well as adaptive non-reciprocal vibration/wave transmission.

The intellectual merit of this dissertation lies in introducing metastable modules that can be synergistically assembled and individually tuned to realize near continuous topology and mechanical property adaptation and elucidating the intricate nonlinear dynamics afforded by the metastructure. This research reveals different kinds of nonlinear instabilities that are able to facilitate the onset of supratransmission, a bandgap transmission phenomenon pertained to nonlinear periodic metastructure. In addition, utilizing this novel phenomenon, supratransmission, together with inherent spatial asymmetry of strategically configured constituents, the proposed metastructure is shown to be able to facilitate unprecedented broadband non-reciprocal vibration and wave transmission and on-demand adaptation.

Since the proposed approach depends primarily on scale-independent principles, the broader impact of this dissertation is that the proposed metastructure could foster a new generation of reconfigurable structural and material systems with unprecedented adaptation and unconventional vibration control and wave transmission characteristics that are applicable to vastly different length scales for a wide spectrum of applications.

Chapter 1

Introduction

1.1 Overview

The goal of this research is to create a paradigm shift for multifunctional adaptive structures by exploiting and harnessing metastable modular mechanics and dynamics to provide novel pathways for shape, mechanical property, vibration and wave energy transmission controls. The idea is based on the translation of modular architectures, which have been observed in many biological and atomistic systems in nature or implemented in artificial metamaterials [1] [2] [3] [4] [5] [6] [7] [8] [9] to the macroscopic structural scale. The following section first gives an overview of the field of metastructures and metamaterials followed by some concepts and methodologies pertaining to this thesis. Then, the motivations and research objectives are discussed and highlighted.

1.2 Metastructures and metamaterials

The mechanical properties of natural materials can span only a specific, limited parameter range and are often times coupled with each other. For instance, Poisson's ratio of most natural materials is positive [10] and elastic modulus and density for certain classes of materials are related to each other through a power law [7]. These constraints largely limit the design space and practical applications of natural materials. It is therefore desirable to develop structures/materials that could exhibit a chosen set of mechanical and physical properties. To engineer such structures/materials, large amount of research effort has been directed towards metastructures and/or metamaterials: structure/material with some form of spatial periodicity, either in its constituent material properties, internal micro architecture or boundary conditions. These systems comprised of repeating patterns, sometimes known as unit cells, are attractive, in part, because the purposefully designed micro-architectures can often give rise to global mechanical properties that are much different and more desirable than the material from which the structure is made.

Metastructures and metamaterials mainly exhibit two prominent advantages over its counterpart, conventional bulk materials and/or structures. First, these systems are invested with unprecedented adaptivity that can more effectively interact with a wide range of environmental variations and operating conditions. Such system-level multifunctionality can help minimize weight and maximize suitability to diverse missions and maneuvers, factors which are favorable, for example, in aerospace, automotive, and defense industries [11]. By periodic and cellular designs, the global properties of metamaterials have exhibited tunable Poisson's ratio [12] [13], negative stiffness [14], inverted compressibility [15], simultaneous high stiffness and low thermal expansion [16], as well as simultaneous low in-plane stiffness and very high out-of-plane flexural bending stiffness [17], just to name a few. See [18] [19] [20] for more detailed reviews on related topics.

Secondly, these spatially periodic structures also exhibit intriguing wave propagation characteristics, amongst which wave filtering is of particular interest in many engineering applications. The filtering property refers to the fact that metastructures/metamaterials only allows the propagation of wave energy with frequency content in a certain interval. The frequency band in which wave energy propagates through the chain is called passband [21]. All other frequency components are spatially attenuated with energy localized to the source of excitation and this interval is called stopband. The wave filtering properties of metastructures has also enabled an array of applications spanning from vibration isolation [22], wave steering [23], energy harvesting [24], acoustic wave signal processing [9], to even cloaking [25]. See [26] [27] [28] [29] for recent reviews on these topics.

1.3 Reconfigurable metastructure and metamaterial

Since the filtering properties depend highly on lattice geometry as well as stiffness and mass distributions [21], this poses a major limitation on linear metastructure, in which band structures, locations of passband and stopband, are fixed unless the overall structure or the periodicity is altered. To overcome this restriction a lot of research effort has been focused on systems with capability of in-situ changing lattice geometry or mechanical properties. One approach is to utilize continuous active actions. For instance, Goffaux and Vigneron [30] controlled phononic bandgaps by rotating a set of parallel solid square-section columns distributed in air. Wang et. al. [31] exploited different degrees of buckling of elastic beams to manipulate the wave propagation using an elastic matrix. Yeh [32] demonstrated tunable bandgaps by varying the applied electric field with electrorheological material, whose physical properties depend on the applied electric field. Robillard et.al [33] achieved controlling of bandgaps by varying applied magnetic field of a magneto-elastic periodic structure. For detailed discussions and other works related to this topic, see reviews in [18] [26] [34] [35] [36] [37] [38] [39]. In these investigations, physical parameters of the periodic structure are modified by constantly applying external sources of control such as magnetic or electric fields. These active approaches can theoretically achieve continuous changes in system properties but at the same time they require continuous external control power

Another approach to realize reconfigurable metamaterials is to take the advantage of coexisting multiple stable states (multistability); these are adaptive-passive methods often facilitate property changes without the need for continuous, active control intervention. Exemplary demonstrations of the adaptivity enabled by multiple stable states include the morphing capabilities of prestressed composite laminates [19] [40] or origami-inspired designs [41] [42] [43], such that the system topology may dramatically vary between the statically stable shapes. Engineered carefully, reversible adaptation on system properties can also be achieved switching amongst the equilibrium positions, which is desirable for wave filtering characteristics. For instance, Schaeffer and Ruzzene [44] studied multistable magneto-elastic lattice that exhibit different mechanical properties in each of their stable configurations. Haghpanah et. al. [45] designed a multistable architected structure based on building blocks encompassing fexible hinges and showed variable mechanical response enabled by multistability. Rafsanjani et. al. [46] presented a monolithic metamaterial whose tensile stress-strain curved can be tuned by harnessing snap-through instabilities. See [47] [48] [49] for recent reviews on related topics.

1.4 Nonlinear metastructure and metamaterial

Many of the aforementioned investigations on reconfigurable metastructures and metamaterials comprise unit cells that are bistable or multistable, which is inherently nonlinear [50]. This entails that, dynamically, when motion amplitudes are small, wave transmission is still dominated by linear dispersion relations. However, when amplitudes become large enough that nonlinear forces are no longer negligible, in the presence of nonlinearity, systems can exhibit rich nonlinear dynamical behaviors such as bifurcation phenomena, nonlinear resonances, and even chaotic vibrations just to name a few. Therefore, exploiting the nonlinear response of structures can reveal new phenomena and hidden design opportunities that otherwise not possible using only linear systems which can potentially accommodate broader design goals. In this section, we review some of the literature related to dynamical phenomena in nonlinear periodic metastructure and metamaterial.

One of the famous and well-known wave propagation phenomenon in continuous nonlinear systems is called solition [51] [52]. It describes a localized wave packets that is able to maintain their shape when traveling at a constant speed generated by a balance between nonlinearity and dispersion. More intriguingly, when two solitons travel in the same direction passing through each other, instead of obeying the superposition rule for linear waves, they maintain individual shapes with only a phase change [53]. For discrete systems, due to lack of arbitrarily translational invariance, solitions sometimes are prevented from propagating through the chain [54]. However, another type of localized, time-periodic dynamical energy in a perfect nonlinear lattice can be stabilized by the lattice discreteness and is known as intrinsic localized modes or discrete breathers [55]. Unlike solitons, collision between discrete breathers results in energy transfer from less localized breathers to more localized ones. Discrete breathers have been observed in many physical systems ranging from nonlinear crystal dynamics [56] [57], magnetic lattices [58] [59], electron-phonon systems [60] [61] to tailored optical materials [62] [63]. It should be also noted that when there exists damping in the system, external harmonic excitation is required to sustain the discrete breathers. For instance, both stationary and moving discrete breathers have been observed in micromechanical cantilever arrays that are believed to be important for future designs of microresonator arrays intended for signal processing, communication, and sensor applications in

MEMS devices [64] [65]. See [55] [66] for detailed reviews of related topics with other applications.

Besides discrete breathers, which mostly concerns the energy localization in nonlinear periodic structures subject to external uniform harmonic excitation, there are two other important classes of problems: pulse propagation and response to external point harmonic excitation in nonlinear periodic structures [67]. For pulse propagation, a large body of literature in nonlinear mechanics focuses on granular chains, in which, nonlinearity arises from the contact forces between adjacent units [68]. Detailed theoretical and experimental investigations on pulse wave propagation in both homogeneous and inhomogeneous granular medium with different pre-stresses have been studies by many researchers [69] [70] [71] [72] [73] [74] [75] [76] [77] [78] [79] [80]. For the situation where an external point harmonic excitation is applied to one unit cell of a nonlinear periodic structure, influence of nonlinearity on wave propagation characteristics are two folds. First, since resonant frequencies of the nonlinear system depend on the total energy of the system, which can be described by the vibration amplitude of the motion, dispersion characteristics of a nonlinear periodic structure is hence amplitude dependent [81] [82]. As a result, nonlinearity offers the opportunity to design metastructures and metamaterials with tunable wave filtering characteristic that can potentially enhance the performance over linear periodic structure [83] [84] [85] [86] [87]. Secondly, due to nonlinear resonance [88] or bifurcation phenomena [89] [90], nonlinear periodic structures offer a pathway to enhanced wave energy propagation. Nonlinear resonance can occur due to internal or combination resonances with harmonic excitation [91] [92] [93] and this may occur for frequencies inside or outside the linearized pass band. The latter mechanism, also known as nonlinear supratransmission, occurs when excitation frequency lies outside the pass band.

Supratransmission describes a sudden transmission of wave energy in periodic structure excited at one end with input frequency inside the linear bandgaps [94]. For small excitation amplitude, similar to a linear system, energy injected into the system is spatially attenuated away from the input and does not propagate through the chain. However, when input exceeds a threshold amplitude, even though the excitation frequency is still in the bandgaps, energy transmission becomes possible due to nonlinear instability [95]. Supratransmission was first studied in discrete periodic structures by Geniet and Leon [94] [95] and since then, this intriguing phenomenon has been observed and extensively investigated in many discrete nonlinear systems, such as sine-Gordon and Klein-Gordon chains of coupled oscillators [89] [96] [97] [98], Josephson junction parallel array [99], Fermi-Pasta-Ulam (FPU) nonlinear chains [100] [101] , granular crystals [102] [103] and periodic bistable chains [104] [105].

We are aware of the fact that there is also a large body of literature concerning nonlinear structures with disorder. Such disorder can be induced by adding nonlinearity to a linear system to achieve novel phenomena such as tunable broadband resonator [106], irreversible nonlinear energy sink [107] [108], and tunable nonlinear bandgaps [109] just to name a few. An alternative way of realizing disorder is by introducing defects on a nonlinear periodic structure [110]. Disorder in a periodic structure, either engineered intentionally or induced by manufacturing tolerance, can give rise to Anderson localization where response of a disordered periodic structure decays exponentially away from the source of excitation even though the excitation is within the passband of an otherwise periodic system [111] [112] [113] [114] [115] [116]. However, since the focus of this research is on dynamics of periodic nonlinear metastructures, we leave out on purpose a myriad of papers on the interplay between nonlinearity and disorder in periodic structures.

1.5 Motivations

As surveyed above, reconfigurable metastructures and metamaterials in general are desirable for engineered structural-material systems to achieve high performance, versatility, and multi-functionality in many mechanical, aerospace, and civil applications [12] [17] [19] [117] [118] [119] [120] [121] [122] [123] [124]. Particularly for the adaptive-passive approach [44] [48] [49], it has been demonstrated to be an effective and efficient method for creating multifunctional adaptive structural systems. On the other hand, there are still critical challenges to address and significant room for improvement before the concept can achieve real-world impacts. First, with current approaches, the modules reconfigure collectively to achieve global topology adaptation. As a result, the structure only exhibits limited number of configurations that are discretely different from each other, which greatly undermines the impact of the reconfiguration. In addition, since the current focus has been on achieving reconfiguration utilizing global external fields, independent changes of the individual modules are not possible or not explored. Such local module adaptation, on the other hand, can be very powerful to accomplish many more distinct configurations that can potentially enable near continuous changes for the adaptive-passive approach. Lastly, Most of the metamaterials investigations are focusing on the "materials" characteristics assuming infinite domain without considering the "structure" aspect of the systems. The effects of having finite domains and boundary conditions will generate new research issues and phenomena that are critical to real-world systems.

In the pursuit of novel vibration and wave transmission control, the notion of non-reciprocal or one way wave energy propagation through a lattice has been found to be useful and achieved in various energy forms [102] [125] [126] [127] [128] [129] [130] [131]. For instance, Fleury et al. presented an acoustic circulator based on angular-momentum biasing through a circulating fluid [132]. Swinteck et al. demonstrated bulk waves with unidirectional backscattering-immune topological states using superlattice with spatial and temporal modulation of the stiffness [133]. Wang et al. proposed an all-optical optical diode via a "moving" photonic crystal to control the flow of light [134]. Liang et al. coupled a nonlinear medium with a supperlattice and accomplished unidirectional acoustic wave propagation by exploiting second-harmonic generation (SHG) of the nonlinear medium together with frequency selectivity of the linear lattices [129]. Popa and Cummer characterized an active acoustic metamaterial coupled to a nonlinear electronic circuit and demonstrated an isolation factor of >10 dB [135]. Recently, studies on non-reciprocal waves in systems with bistable elements have also received attentions [136] [137] for their intriguing nonlinear behavior [138]. See [28] [139] for reviews on recent developments for this unique wave propagation characteristics. While many of these and other previous studies pivot on the realization of unidirectional energy transmission are intriguing, investigations on systems capable of on-demand tuning of such non-reciprocal wave propagations that are beneficial in many applications [28] [139] are still limited. Boechler et al. illustrated that taking advantage of the localized defect mode, tunable rectification could be achieved by adjusting the static load of a defected granular chain [102]. They demonstrated the one-way wave propagation phenomenon experimentally for selected frequencies below and close to the defect frequency. Chen and Wu presented a tunable topological insulator through both analysis and numerical experiments using a 2D phononic crystal [140]. They showed the existence of the topologically nontrivial bandgaps by actively inducing airflow and frequency ranges that exhibit one-way wave propagation can be tuned by varying airflow velocity as well as lattice geometry. However, once the static load [102] or air flow rate

[140] is fixed, both studies showcased the non-reciprocal harmonic wave propagations only for a limited frequency range. For transition waves, Raney et al. realized a tunable soft mechanical diode capable of one-way solitary wave propagation in elastomeric bistable lattices [141]. They observed unidirectional pulse propagation using a heterogeneous chain composed of a region with soft connectors combined in series with a region with stiff connectors and discovered that the propagation speed can be tuned by varying the beam end-to-end distance. While all these studies [102] [140] [141] demonstrate tunable non-reciprocal wave propagation, such adaptation can only be induced by the change of global topology or constraint. The reconfiguring of the numerous internal modules/components individually and synergistically for a given global confinement, which can significantly expand the adaptation space and greatly benefit wave control, are not allowed with the current approaches.

1.6 Research objectives

With the aforementioned motivations, focus of this research is on the meso- and macro-scale metastructures with structural components beyond materials level and taking into account of having finite domains and boundary conditions that are more realistic for real-world applications. Objectives of this research are therefore to:

1. Devise unit module that can be synergistically assembled and individually tuned to facilitate multifunctional reconfigurable structures with unprecedented adaptivity for mechanical property, vibration and wave transmission control.
2. Develop analytical methods to evaluate system properties of the assembled metastructure and investigate the adaptivity afforded by the reconfiguration of individual module.

3. Investigate the dynamical response of the structure and propose analytical methods to assist analyzing and synthesizing system with desired vibration and wave transmission properties.
4. Explore the opportunity to achieve adaptive nonreciprocal wave transmission using the proposed metastructure and further the understanding of the phenomenon by uncovering the underlying mechanisms.
5. Validate analytical findings for both static and dynamic analyses by constructing testbeds and performing experimental investigations.

1.7 Thesis outlines

The rest of this work is organized in six main chapters. We start in Chapter 2 by presenting the proposed metastable module and a proof of concept experiment setup. We derive the analytical formulation for metastructure assembled from metastable modules in parallel and perform parametric study on a two-module assembly both analytically and experimentally. Motivated by the promising results, in Chapter 3, we seek to build upon previous foundational concept by redesigning the mechanical module in such a way as to investigate how the favorable system-level adaptivity and performance of modular metastructures should be tailored with the assembly of many metastable modules. We perform both analytical and experimental investigations on harnessing transitions amongst metastable states for shape change and system property adaptation and develop Genetic Algorithm (GA) optimization routine to synthesize system with desired property profiles. In Chapter 4, we start to investigate the dynamical characteristics of a single metastable module. We derive analytical estimation on the response of the module under harmonic excitation using harmonic balance (HB) method and perform numerical and experimental study to verify the analytical findings. In Chapter 5, we study the dynamics of metastructure assembled from metastable modules in series for on-demand reconfiguration of band structures and present experimental and numerical evidence on opportunity of realizing non-reciprocal wave propagation. We discover that this unique phenomenon is achieved by exploiting the nonlinear supratransmission property of a spatially asymmetric metastructure. In Chapter 6, we further the analysis by discovering intricate dynamics affordable by the metastructure and elucidating different kinds of nonlinear instabilities that facilitate the onset of supratransmission. We then propose a localized nonlinear-linear model to analytically estimate the input threshold amplitude required to trigger supratransmission. We conclude in Chapter 7 by summarizing the contributions of this work and providing suggestions for future work and research opportunities.

Chapter 2

Metastable Modular Metastructure: Analysis and Experiments

2.1 Chapter overview

This chapter introduces the metastable modular structure as a platform to illustrate the unprecedented adaptivity. In complement but in contrast to previous investigations, we demonstrate in depth that through the bottom-up procedure, each metastable module can be engineered and tuned independently and the proposed integrated systems termed as metastructures can exhibit exceptional adaptive characteristics resulting from a synergy of the constituents. Analytical and experimental results demonstrate that when metastructures are prescribed a global shape/topology, the systems may yield unique properties adaptation including variation in reaction force magnitude and direction and may realize orders of magnitude change in stiffness. The metastructures also exhibit numerous global statically-stable topologies, the number of which may multiply exponentially. The influences of important parameters on tailoring the displacement range of coexistent metastable states are investigated to provide understanding of how the assembly strategy governs the intriguing versatility and functionality which may be harnessed. The findings suggest that these metastructures represent a major leap forward in adaptive structural-material systems and introduce new concepts for phase-transition structures.

2.2 Proof-of-concept metastable module

A passive, mechanical modeling of muscle's microscale contractile systems, sarcomeres, has suggested that its building blocks, nanoscale cross-bridges [1], are a critical source for muscle's intriguing passive macroscopic functionalities observed in biological data [2] [142]. In the mechanical representation, the cross-bridge was shown to exhibit coexistent metastable states for the same sarcomere length [2] [142]. The metastable configurations represent the cross-bridge in either pre- or post-power stroke during the sarcomere contraction cycle which is the origin of contractile force. The study modeled the passive cross-bridge as bistable and linear springs in series [2], thus identifying equivalent structural constituents that emulate the essential ingredients of muscle's manifestation of metastability. Recent study further reveals that responses of such mechanical model are fundamentally different in hard (displacement controlled) and soft (force controlled) loading devices [143]. To harness the cross-bridge modeling insight [2], this research seeks to create and explore a concept for engineering passive-adaptive metastructures from the development and strategic integration of mechanical metastable modules. The term "metastable module" denotes that the module exhibits coexistent metastable states like the cross-bridge pre- and post-power stroke configurations for a prescribed sarcomere length and "metastructures" denotes that the global structural/material systems are invested with unprecedented characteristics derived from the synergy of their constituents. Although we are inspired by muscle, our goal is not bio-mimicry. Instead, we seek to uncover and elucidate the advanced functionalities and versatility invested in passive-adaptive engineered systems when a metastable module building block is translated upwards from the nanoscale.

Following the cross-bridge model [2] adapted here as shown in schematic in Figure 1(a), we devise and create a metastable module composed of bistable and linear springs in series. It is important to note that although the module includes a bistable spring, the capacity for multiple coexistent metastable states that is empowered by the metastable module composition sharply differentiates our module from a strictly bistable system which cannot realize multiple states for one displacement constraint [144]. Also, contrasting the previous modeling of the cross-bridge which utilized a bilinear/bistable spring [2] [142] [143], metastable module employs a continuous bistable spring characterized using a continuous, cubic polynomial expression for the spring restoring force, given by $F_b = k(x-a)(x-2a)$. Here, x is the displacement of bistable spring which we refer to as the internal coordinate; k is a stiffness coefficient; and a is the distance between the bistable spring unstable equilibrium and a stable equilibrium. Note that this force expression indicates symmetry between the statically-stable equilibria of the bistable spring and the central unstable position. In Figure 1(a), the potential energy of the bistable spring restoring force is illustrated as the classical, double-well potential energy, within which the internal coordinate is located. This bistable spring is connected in series to a linear spring which exhibits a restoring force expressed by $F_L = k_L(z-x)$ where z denotes the global end displacement and k_L is the spring stiffness. These are the essential components of our metastable module which is employed in the assembly of metastructures in later investigations.

To fabricate proof-of-concept metastable modules, frame-mounted bistable springs, realized using compressed and buckled spring steel beams fixed into supporting PMMA frames, are connected in series to a linear compression coil spring, aligned to translate uniaxially, Figure 1(c). The coil springs is attached to the center point of the buckled beam and is acted upon by a prescribed global topologies/displacements z on the opposing end. For single-module experimentation, the opposing coil spring end is attached to a load cell which is attached to a quasi-statically actuated electrodynamic shaker. Shaker displacement or global topologies/displacements z is measured using a laser interferometer. Stiffness is determined by the derivative of the force-displacement profiles. The supporting frames measure 0.15 m 0.15 m by 6.5 mm with an interior cavity of 0.1 m by 0.1 m. Thus, 0.1 m is the spring steel beam length prior to applying axial compression to buckle the beam. The spring steel beams are 0.127 m wide by 0.18 mm thick. Axial beam compression is accomplished via micrometer adjustments against a sliding end of the beam clamping fixture inside the frame. The straightforward design of the fabricated metastable modules captures the essential, passive mechanical ingredients of the cross-bridge, and, indeed, is advantageous so that investigations can be focused on the new phenomenological behavior without potential misdirection by nonessential elements. In Figure 1(a,b) and (c,d), the two coexistent metastable states are illustrated for the metastable module model and experimental system, respectively, showing that for one prescribed global end displacement z, the internal state (coordinate) x may rest at one of two metastable configurations. Such coexistence of metastable states for our module is the key feature derived from our cross-bridge inspiration.

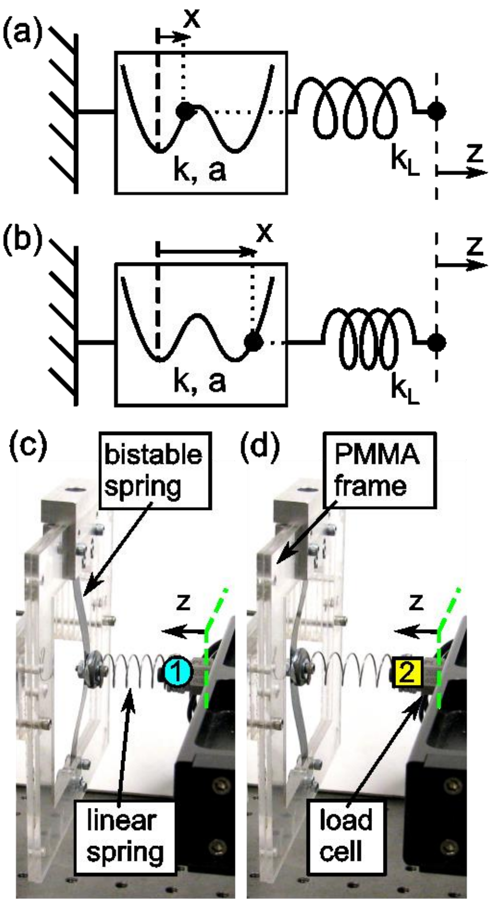

Figure 1. (a) Mechanical model of the metastable module of bistable and linear springs in series. The potential function of the bistable spring is shown as a double-well potential energy within which the internal coordinate is located. Between (a) and (b), the coexistent metastable states for a prescribed end displacement, z, are illustrated. (c,d) Proof-of-concept, experimental metastable module, illustrating comparable coexistent metastable states as shown in (a,b), respectively.

2.3 Exploration of single metastable module mechanical properties

To illustrate the novelty and advantageous feature of the metastable module, this section explores a preliminary study of a single module with parameters $k = 1$ N/m3, $a = 1$ m, $k_L = 0.3$ N/m. Detailed analytical work will be presented in next section. Results show that the coexistence of multiple metastable states yields notable adaptation of global structural features, including potential energy, reaction force, and stiffness, as shown in Figure 2(b,c,d) respectively. When the coexistent metastable states exhibit distinct potential energies, like that shown across the metastability range, defined as the range of global displacements z within which multiple metastable configurations coexist, for our module in Figure 2(b), it is known that a system may exhibit adaptive or non-natural characteristics while the external shape/structure remains fixed [15] [145] [146] [147] [148] [149] [150], which helps support the premise of the modular metastructural development. Analytical and experimental results, Figure 2(c,d) respectively, reveal multiple static equilibria topologies, indicated by the global displacements satisfying zero force. Moreover, the results in Figure 2(c,d) show magnitude and direction adaptation of module reaction forces is possible via switching between coexistent metastable states. The connections between metastable state realization and corresponding reaction force behaviors are exemplified by the markers labeled 1 and 2 shown in Figure 1(c) and Figure 2(d). The variation in reaction force direction is a particularly unique adaptivity. For example, when length z is fixed, the module will exert either resistive or assistive forces at the global end depending on which metastable configuration is realized. Such capacity is not possible using a bistable system alone, because a bistable system cannot realize multiple reaction forces for one displacement constraint. Consequently, the metastable module is more analogous to a phase-transition structure since the shape remains constant while its reaction to the environment drastically alters via change between coexistent metastable states. Such phase-transition characteristics may manifest into large energy dissipation when actuated amongst statically-stable equilibria. To exemplify this, a dynamical model is also derived with bistable mass $m = 1$ kg and damping $b = 0.5$ N/(m/s), Figure 2(a). The global end displacement z is quasi-statically actuated back and forth at a rate of 0.5mm/s starting from one of its stable position (yellow circle) covering the range from -2m to 4m, Figure 2(c). The corresponding force displacement profile shown in thick solid cyan, Figure 2(c), clearly depicts the large hysteresis loop formed by encompassing the two statically stable equilibria/zero force positions.

Over the metastability range, we find that modules may also exhibit one of two stiffnesses corresponding to the respective metastable states. Between these two states, experimentally and analytically we observe orders of magnitude in stiffness variation may be effected, Figure 2(e,f). The global topologies for which stiffness adaptations are most dramatic are seen to occur near the extremes for which the respective metastable configurations occur. For example, measurements reveal more than four orders of magnitude stiffness change by switching between metastable configurations when the global displacement is fixed at z=10 mm (86.71 N/m to 0.02799 N/m), Figure 2(f). Moreover, analytical and experimental results find that the module may realize negative stiffness at the extremities of the metastability range, Figure 2(e,f). Due to the global end displacement constraint for the module, it has been shown that negative stiffness may in fact be "stabilized" [151]. To summarize, the module-level theoretical and experimental results show that exploiting multiple coexistent metastable states in the structural module cultivates considerably advanced adaptation features.

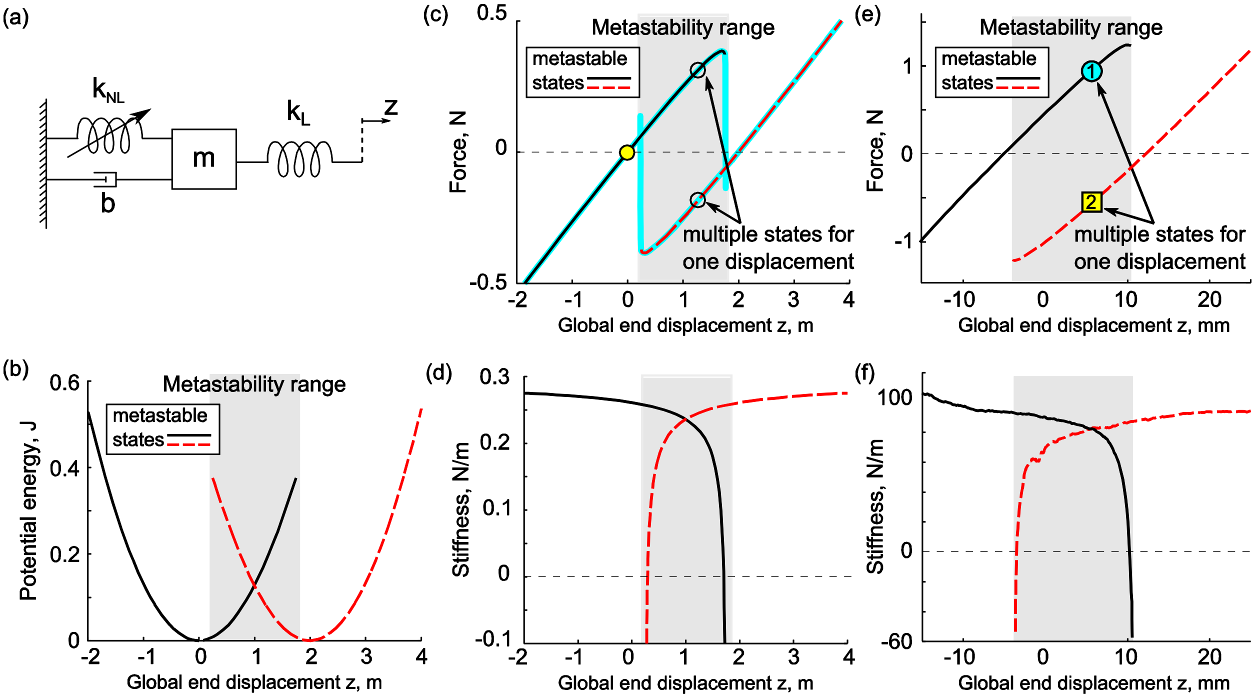

Figure 2. (a) Schematic of single-module for quasi-static dynamical analysis. Single-module analytical results of (b) potential energy, (c) reaction force, and (d) stiffness as functions of global displacement. Single-module experimental measurements of (e) reaction force and (f) stiffness. Markers regarding coexistent forces/displacements in (e) correspond to coexistent metastable configurations in Figure 1(c). Light shading denotes metastability range where structural adaptation is realized, and each line indicates a metastable state.

2.4 Mathematical formulation for metastructures assembled from metastable modules in parallel

In this research, one dimensional metastructures are assembled via metastable modules in parallel with a common, global end displacement. The assembly strategy follows the biological architecture where sarcomeres are assemblies of cross-bridges in parallel [1]. In this way, we emulate the fundamental mechanical phenomena and organization of the biological inspiration using our mechanical metastructure. A schematic of an assembled metastructure is shown in Figure

3. For this system, n modules are arranged in parallel with respect to a common global end displacement z. Within each module, a bistable spring with restoring force

$$F_{ib} = k_i x_i (x_i - a_i)(x_i - 2a_i) \qquad \text{(Eq. 1)}$$

is connected in series to a linear spring having restoring force $F_{iL} = k_{iL}(z - x_i)$, where x_i is the i^{th} module internal displacement representing the deformation of the bistable spring from the static equilibrium $x_i = 0$; a_i is the i^{th} bistable spring span which denotes the distance between the unstable and stable equilibrium positions of the bistable spring; and k_i and k_{iL} are stiffnesses. The total potential energy of the metastructure is then expressed by

$$U = \sum_{i=1}^{n}[\tfrac{1}{2}(2a_i^2 k_i + k_{\mathrm{i}L})x_i^2 - a_i k_i x_i^3 + \tfrac{1}{4}k_i x_i^4 - k_{iL} z x_i + \tfrac{1}{2}k_{iL} z^2] \qquad \text{(Eq. 2)}$$

which is a function of internal coordinates x_i as well as the global end displacement z. A metastable internal state/configuration for a fixed global topology z of the metastructure must satisfy $\partial U/\partial x_i = 0$ and $\partial^2 U/(\partial x_i \partial x_j) > 0$, where the latter indicates that the Hessian matrix is positive definite [152]. The former constraint leads to a series of force balance equations, one for each module in the assembly:

$$k_i x_i^3 - 3a_i k_i x_i^2 + (2a_i^2 k_i + k_{iL})x_i - k_{iL} z = 0;\ \forall\, i = 1,2,\ldots,n \qquad \text{(Eq. 3)}$$

The solutions to equation (3), i.e., the roots of the cubic polynomials, are then substituted into the Hessian matrix to evaluate for positive definiteness. Since the system is assembled from modules in parallel, the modules are decoupled. Therefore, non-zero entries of the Hessian matrix only occur on the diagonal and determination of positive definiteness is equivalent to inspecting $\partial^2 U/\partial x_i^2 > 0, \forall\, i = 1,2,\ldots,n$. From equation (3), the cubic polynomial may have at most three stationary points, and at most two which are stable via $\partial^2 U/\partial x_i^2 > 0$. Thus, for each module in the metastructure, there are at most two configurations satisfying both of the constraints. The two real roots of the i^{th} cubic polynomial require that the discriminant of equation (3) satisfies:

$$\Delta_i = 54k_i^2 a_i k_{il}(2a_i^2 k_i + k_{iL})z - 108k_i^3 a_i^3 k_{il} z + 9k_i^2 a_i^2 (2a_i^2 k_i + k_{iL})^2 - 4k_i(2a_i^2 k_i + k_{iL})^3 - 27k_i^2 k_{iL}^2 z^2 \geq 0 \qquad \text{(Eq. 4)}$$

Equation (4) can be rearranged into a quadratic polynomial inequality in terms of global end displacement z:

$$C_{i2}z^2 + C_{i1}z + C_{i0} \leq 0 \qquad \text{(Eq. 5)}$$

Here, coefficients $C_{i2} = 27k_{iL}^2 k_i^2$, $C_{i1} = -54a_i k_{iL}^2 k_i^2$ and $C_{i0} = k_i(4k_{iL} - a_i^2 k_i)(k_{iL} + 2a_i^2 k_i)$ are functions of system spring stiffnesses and the bistable spring span. Therefore, end displacements leading to multiple coexistent metastable states for each module can be explicitly derived as a function of system parameters from equation (5) and satisfy the following criterion.

$$\frac{-C_{i1} - \sqrt{C_{i1}^2 - 4C_{i2}C_{i0}}}{2C_{i2}} \leq z \leq \frac{-C_{i1} + \sqrt{C_{i1}^2 - 4C_{i2}C_{i0}}}{2C_{i2}};\ \forall\ i = 1,2,\dots,n \qquad \text{(Eq. 6)}$$

Consequently, the extent of the metastability range for the metastructure assembled from n modules is determined using

$$\cup_{i=1}^{n}\left[\frac{-C_{i1} - \sqrt{C_{i1}^2 - 4C_{i2}C_{i0}}}{2C_{i2}}, \frac{-C_{i1} + \sqrt{C_{i1}^2 - 4C_{i2}C_{i0}}}{2C_{i2}}\right] \qquad \text{(Eq. 7)}$$

Having determined the metastable states of the metastructure, the total end (reaction) force at global topology z is found using $F_{end} = \sum_{i=1}^{n} k_{\mathrm{iL}}(z - x_i)$. The stiffness of the metastructure at each global end displacement is obtained by Hooke's law

$$k_a = \frac{\partial F_{end}}{\partial z} = \sum_{i=1}^{n} k_{iL}(1 - \partial x_i/\partial z) \qquad \text{(Eq. 8)}$$

where $\partial x_i/\partial z$ can determined implicitly from equation (3).

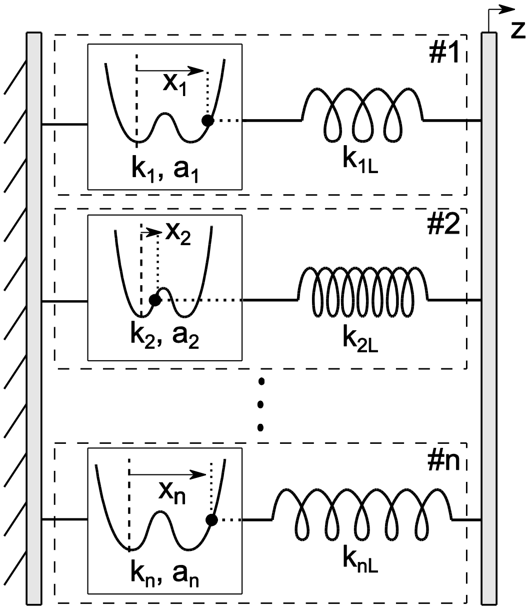

Figure 3. Schematic of the modular metastructure with *n* metastable modules assembled in parallel

2.5 Analytical and experimental case studies

2.5.1 Analytical case study for a two-module metastructure

In this section, a preliminary analytical study of a two-module metastructure is performed to investigate representative structural characteristics invested in the system via the coexistence of metastable states for each module. The two modules are different in design parameters, and hence in structural features. The specific parameters used in the analysis are $k_1 = 1$ N/m^3, $a_1 = 1$ m, $k_{1L} = 0.3$ N/m and $k_2 = 16/81$ N/m^3, $a_2 = 3/2$ m, $k_{2L} = 8/45$ N/m. The parameter values indicate that the stable equilibria of the two bistable springs of the modules are located at (0,2) m and (0,3) m. We note that these parameters are chosen arbitrarily and are thus used for representative purposes in deriving first insights pertaining to the primary features of the metastructures. Using the equations from the mathematical formulation, the metastable states of the two-module metastructure are determined and the corresponding global end forces and stiffnesses are plotted in Figure 4. Throughout this work, in the profiling of force and stiffness as end displacement is varied, the distinct line styles represent different combinations of metastable internal configurations. Here, AA is used to indicate that the attachments between linear and bistable springs of both modules remain at positions with displacements greater than the unstable static equilibria, i.e., in this case study satisfying $x_1 > 1$ m and $x_2 > 1.5$ m, respectively. Conversely, the label BB means that these spring connections remain at positions with displacements less than the unstable static equilibria, and thus satisfy $x_1 < 1$ m and $x_2 < 1.5$ m, respectively. The mixed labels AB and BA denotes the corresponding mixed cases of internal module configurations. Lastly, for completeness, we add that if the internal coordinate of a metastable module maintains the unstable equilibrium position of the bistable spring for fixed end displacement z (here, the internal coordinates would satisfy $x_1 = 1$ m or $x_2 = 1.5$ m), this indicates that the metastable module design is such that coexistent metastable states are not realized and the module is equivalent to a bistable spring directly acted upon by the end displacement, implying $x_{1,2} = z$. This trivial limiting case does not occur in the following investigations.

Figure 4(a) shows that the two-module metastructure exhibits multiple distinct force profiles, one representing each metastable configuration set of the system. The plot also reveals four global displacements yielding zero reaction force, i.e., statically-stable equilibrium positions. As identified using the analytical model, the number of metastable topologies of the metastructures may increase exponentially according to the number n of modules employed. In other words, an n-module metastructure may exhibit at most 2^n stable configurations: this is evidently a synergy due to the assembly of the strategically designed metastable modules. This is exemplified by a representative force-displacement profile in figure 4(c) for a six-module metastructure. Using an example set of parameters, 64 (N=6 and thus 2^6=64) statically-stable equilibria topologies are found along a broad metastability range. When prescribed an end displacement, figure 4(c) shows that significant and near-continuous force magnitude/direction adaptivity (and hence stiffness) is effected via the switching amongst coexisting metastable states. Note that an exponentially multiplying number of statically-stable equilibria can't be realized using traditional bistable systems in parallel, which clearly indicates the enhanced benefits of the metastructural assembly of metastable modules.

As shown in Figure 4, for this representative case, the metastability range spans from approximately $z = 0.25$ m to $z = 2.17$ m. Shown in the force profile, Figure 4(a), when the end displacement z is prescribed, at most four different reaction forces can be realized for this metastructure. For example, at $z = 1$ m, the metastructure can react differently as its internal metastable configurations are changed which, similarly to single-module, for some transitions in metastable states, leads to a change in force magnitude as well as direction. In other words, when the metastructure originally requires one to pull the system to maintain length $z = 1$ m, a metastable state transition may require one to push the metastructure to hold the system at the same length. Likewise, when actuated amongst the four statically stable equilibria, large hysteresis loop can be formed, Figure 4(a). Detailed investigation on tailoring the amount of energy dissipation per cycle for a metastructure will be presented elsewhere. The unique adaptability of reaction force is made possible owing to the fact that our metastable module is bi-valued in displacement for one force as well as bi-valued in force for one end displacement. This characteristic contrasts that of traditional bistable systems which are only bi-valued in displacement for one force value. Thus, even though the metastable module includes a bistable spring, its global properties are significantly distinct from those of traditional bistable systems.

In addition to changes in reaction force, by Hooke's law Figure 4(b) shows that the two-module metastructure exhibits large and continuous adaptability in stiffness when the global shape/displacement is held constant. In fact, orders of magnitude of stiffness variation may be achieved by switching among the internal states when global end displacement is fixed, e.g., at $z \approx 1.7$ m. The change of sign of metastructure stiffness is an indicator that the specific internal configuration is destabilized and would transition into a new metastable configuration set if the global end constraint is removed [151]. Large stiffness adaptation is an important structural feature to enhance numerous engineering systems due to the multifunctionality it may enable, such as for shape morphing, wave-guiding, actuation concepts, vibration control, just to name a few applications [19] [123] [122] [153] [154] [155] and the giant adaptation of stiffness afforded by the metastable module is an attractive capability to leverage. The ability for assemblies of metastable modules to realize such drastic stiffness tailoring over a broad metastability range of global topology indicates these metastructures empower a high versatility.

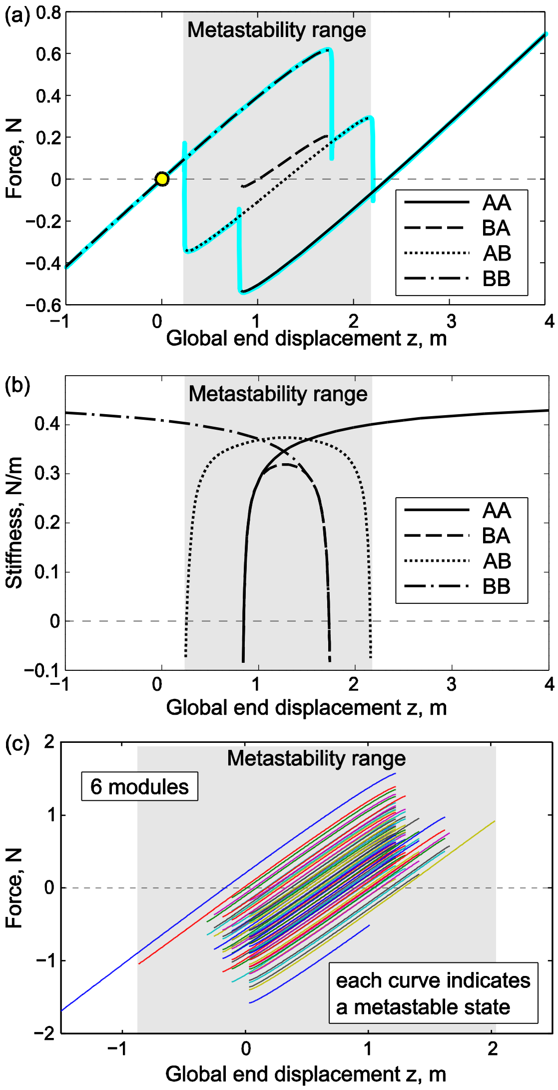

Figure 4. Analytical profiles for two-module metastructure as global end displacement is varied: (a) end force and (b) stiffness. Different line styles denote different metastable configurations. Thick solid cyan line in (a) represents the force displacement profile of the metastructure from quasi-static actuation. (c) Analytical force profiles for six-module metastructure as global end displacement is varied.

2.5.2 Experimental case study for a two-module metastructure

Following the analytical case study, we employ our proof-of-concept experimental system to verify the primary trends of the analysis which revealed that the metastructure could realize a multitude of statically-stable equilibria across a broad metastability range and could enable significant adaptation of mechanical properties for prescribed global shapes. Figure 5 shows the experimental setup of a two-module metastructure, where the modules are labeled using I and II. Similar to single module, the bistable springs are realized via compressed spring steel beams of 0.18 mm thickness, 0.127 m length, and 0.013 m width, which are clamped into PMMA frames. The linear springs are realized by coil springs which are attached to the bistable beams at the center points. The other end of the coil springs are attached to a common rigid connecting bar which is connected to a shaker. The shaker moves uniaxially so as to constrain the global end displacements z to one-dimension. Experiments are conducted by quasi-statically displacing the shaker while global end (reaction) force and global end displacement are recorded using a force sensor and laser interferometer, respectively. Due to the coexistence of metastable states, we perform multiple measurements by starting from all statically-stable global topologies to measure the force profiles related to the potential sets of metastable configurations of the assembled modules. As a result, the experiments are conducted to reconstruct the profiles satisfying the conditions that: (AA) both modules' bistable beam displacements remain to the right of the unstable equilibrium positions with respect to a central, vertical, pre-buckled configuration; (BB) both bistable beam displacements remain to the left, as shown in Figure 5; (AB) the bistable spring displacement of module I remains right and that of module II remains left; and (BA) the bistable spring displacement of module I remains left and that of module II remains right.

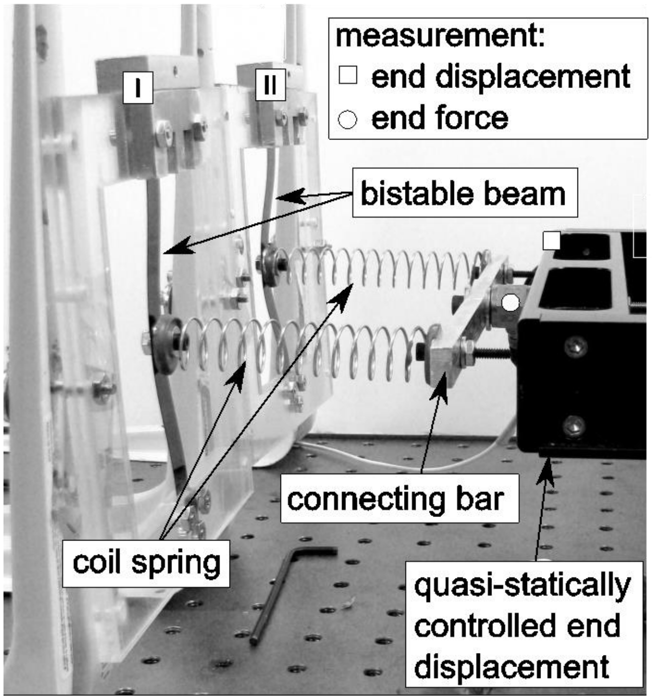

Figure 5. Photograph of a two-module metastructure.

Figure 5(a) presents the measured force profiles of a two-module metastructure as end displacement varies. In agreement with trends predicted analytically in Figure 4(a), the measurements shown in Figure 5(a) reveal four distinct force profiles depending on the metastable configurations exhibited within the metastructure. In this case, each profile exhibits one global topology/displacement satisfying zero reaction force; thus, each metastable configuration set induces a different statically-stable global topology. The measurements show that when the metastructure is prescribed a global displacement, switching amongst internal configurations may change amplitude and direction of the reaction force, which is also in agreement with analytical predictions. For example, as seen in Figure 5(a), when the global displacement is 0.01 m, depending on the metastable configuration, the reaction force may take on four amplitudes, two in each direction. Similar to the analytical results presented in Figure 4(b), the experimental results plotted in Figure 5(b) indicate extreme change in stiffness may be realized by switching amongst the metastable configurations while the global end displacement is fixed. The maximum stiffness variation is seen to occur close to the limits of stability for each metastable state, thus close to the displacements for which the stiffnesses may become negative.

Because the metastructure mechanical properties may adapt while the global end displacement (or constraint) remains fixed, these first analytical and experimental results suggest that metastructures assembled from metastable modules still exhibit features similar to phase-transitions: the global constraint remains fixed while the reactions to the environment vary. The collective results of Figure 5(a) and (b) verify the primary trends of the analysis and clearly demonstrate that the metastructures can yield dramatic mechanical properties adaptivity for constant global topology, induce a multiplying number of statically-stable equilibria across a broad metastability range of global displacement and potentially forming large hysteresis loops when actuating amongst these statically-stable equilibria.

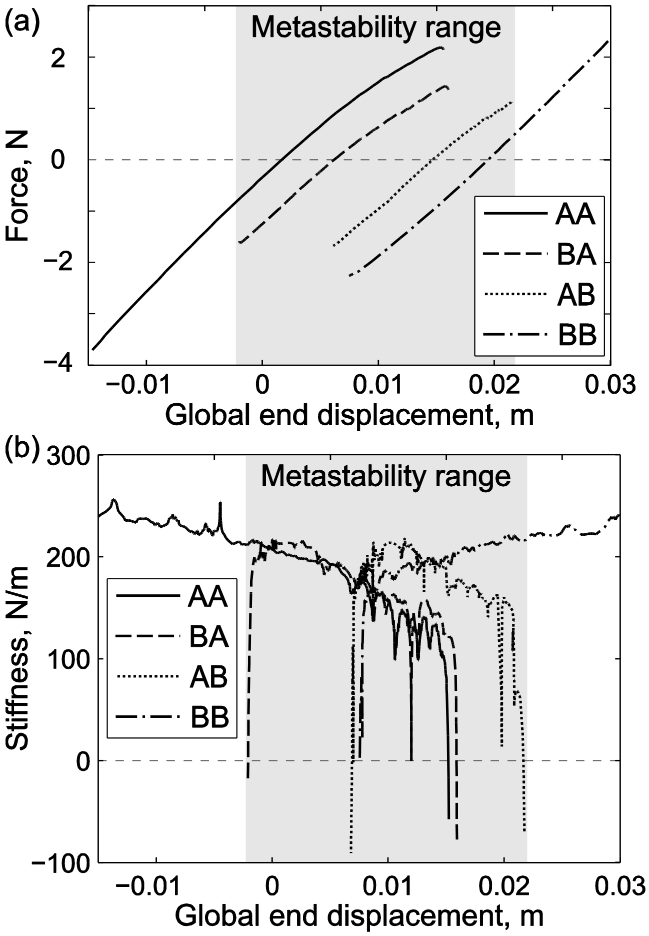

Figure 6. (a) Force and (b) corresponding stiffness profiles of the two-module metastructure as global end displacement is varied.

These analytical and experimental results suggest that switches amongst the metastable states provide immediately reversible properties adaptation or change of global metastructure shape. To provide experimental evidence of the reversible topology changes using metastable state switching, we examine another two-module metastructure that dynamically undergoes transitions of the metastable configurations. First, Figure 6(a) plots the force profiles of the system, once again uncovering the characteristic multitude of unique mechanical properties which may be realized depending on the metastable configuration set of the assembled modules. The four statically-stable equilibria are labeled 1 to 4 in Figure 6(a) and highlighted via the circle points. Then, in Figure

6(b) we plot the time history of the global end displacement while the various metastable configurations are changed via fast manual actuations upon the attachments between module bistable and linear springs. In the experiment, both modules start at positions to the right of the unstable equilibrium of the bistable beams (AA) with respect to the pre-buckled configurations. Therefore, without constraint on global end displacement, the metastructure starts from the position labeled 1 in Figure 6(a), which is the statically-stable topology corresponding to the metastable configuration AA. By switching the internal coordinate of module I to the left of the bistable beam unstable equilibrium, realizing the BA configuration, without an external constraint the global end position immediately changes to the topology labeled 2 in Figure 6(a). The corresponding time history of global displacement at the point of the metastable state switch is shown in Figure 6(b) at time around 6 s, and the reversible switch back to topology 1 occurs around time 15 s. This process is repeated for the changes in topology 1 to 3 to 1, and 1 to 3 to 4 to 1. Note that during the experiments, the global end displacement z is not constraint and free to move therefore instead of following any of the force displacement profiles, end displacement z will naturally settle down at corresponding zero force positions when metastable configuration/internal coordinate switches. This experimental demonstration of metastable state transitions verifies the reversibility of switching amongst the metastable configuration sets as means to realize repeatable and consistent changes in statically-stable global topologies. Because the number of such statically-stable equilibria may increase exponentially as the number of metastable modules increases within the assembly, the global shape change may become nearly continuous, empowering large, smooth compliance for the one-dimensional metastructure.

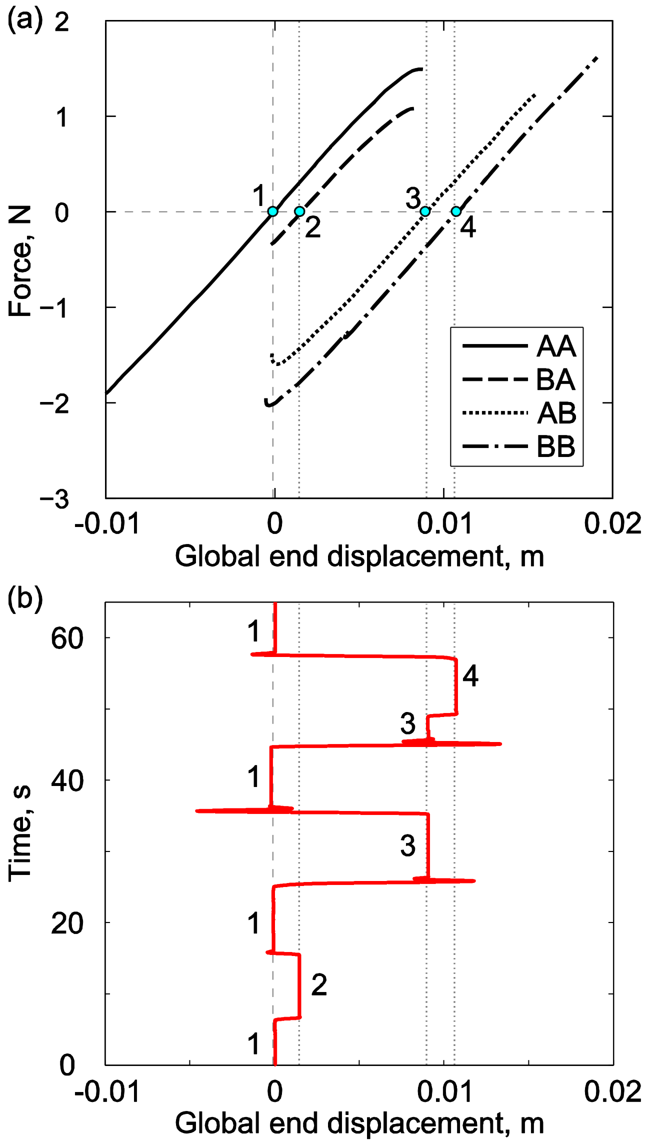

Figure 7. (a) Force profiles of the two-module metastructure as end displacement is varied. (b) Time history of global end displacement as metastable configuration is changed.

2.6 Parametric study for two-module metastructure

The unique adaptation of shape and mechanical properties observed from the prior case studies show that these metastructures may provide high potential for engineering applications for which such versatility is advantageous [19] [119] [120] [123] [153] [156]. To take greatest advantage of these features, the sensitivity of the metastructure properties is now evaluated as key design parameters are changed. In this research, excepting the number of modules in the parallel assembly, all of the design parameters are at the module-level. Thus, in the following sections, we examine the influence on the overall system characteristics as individual metastable module design parameters are changed.

2.6.1 Analytical study of change in bistable spring span a_2

In this section, we use the analytical model to investigate the influence on metastructure characteristics by changing the span between the statically-stable equilibria of the bistable spring of the second module, denoted by parameter a_2. The other system parameters for the following study are $k_1 = k_2 = 1$ N/m^3, $k_{1L} = k_{2L} = 0.5$ N/m, $a_1 = 1$ m, and $a_2 = [0.8\ 1.2\ 1.6]$ m. The top row of Figure 8 plots the global end force as a function of global displacement, while the bottom row of Figure 8 depicts the corresponding stiffness profiles. The labeling convention for the metastable configurations is the same as was employed in the case studies. From left to right, the bistable spring span a_2 increases from 0.8 to 1.2 to 1.6 m.

As clearly shown in Figure 8, the metastability range increases as the bistable spring span a_2 increases. This is due to the fact that as the bistable spring span of the second module increases, according to equation (1) the corresponding peak force amplitudes of the second module bistable spring are increased at the displacements which transition from positive to negative stiffness values (for reference, the feature here discussed is explicitly observable in Figure 10 in the following experimental studies). This in turn makes it possible to stabilize the metastable states over progressively increasing ranges of global displacements because larger forces from deformation of the linear spring (and hence of the global end displacement) are required to counterbalance the increasing bistable spring forces.

To investigate the influence of metastability range on damping capacity of the metastructure, two-module metastructures are actuated quasi-statically at a rate of 0.5mm/s starting at the same statically stable equilibrium marked by yellow circle with corresponding force displacement profiles plotted in thick gray lines, Figure 8(a-c). The actuation range, from -1m to 4m, is chosen such that it encompasses every possible statically stable equilibria for all three cases. As clearly depicted in Figure 8(a-c), hysteresis loop increases as metastability range increases. Specifically, with damping $b = 0.5$ N/(m/s) and mass $m = 1$ kg for both modules, energy dissipation per cycle of the metastructure increases from 0.42 J to 1.70 J to 6.65 J as a result of increase in bistable span. Such more than 10 times increment in energy dissipation capacity is another testimony of the extreme tailorablility of the proposed metastructure as well as a valuable justification of exploring the influence of system parameters on metastability range.

It is also observed that the change of bistable spring span a_2 has little effect on the stiffness profiles at very small and large displacements of the two-module metastructure, as shown in Figure 8(d-f). On the other hand, increases in the second module bistable spring span parameter are seen to gradually increase the location at which the static equilibrium position of the AA metastable configuration occurs. Finally, we see that as the bistable spring span a_2 increases, considering the columns of Figure 8 from left to right, the ranges of displacements over which the metastable configurations AB and BA occur also increase. This effect is especially prominent for configuration AB, where the range is almost non-existent considering the case of shortest bistable spring span, Figure 8(a,d), yet it seen to extend over a majority of the total metastability range for the largest bistable spring span, Figure 8(c,f). The latter finding is important because each metastable state provides for a unique force and stiffness profile, which the metastructure may favorably harness for adaptation of mechanical properties. Thus, a wider range of displacements across which each unique metastable configuration profile exists provides for a broader range of global topologies that are empowered with advantageous adaptivity.

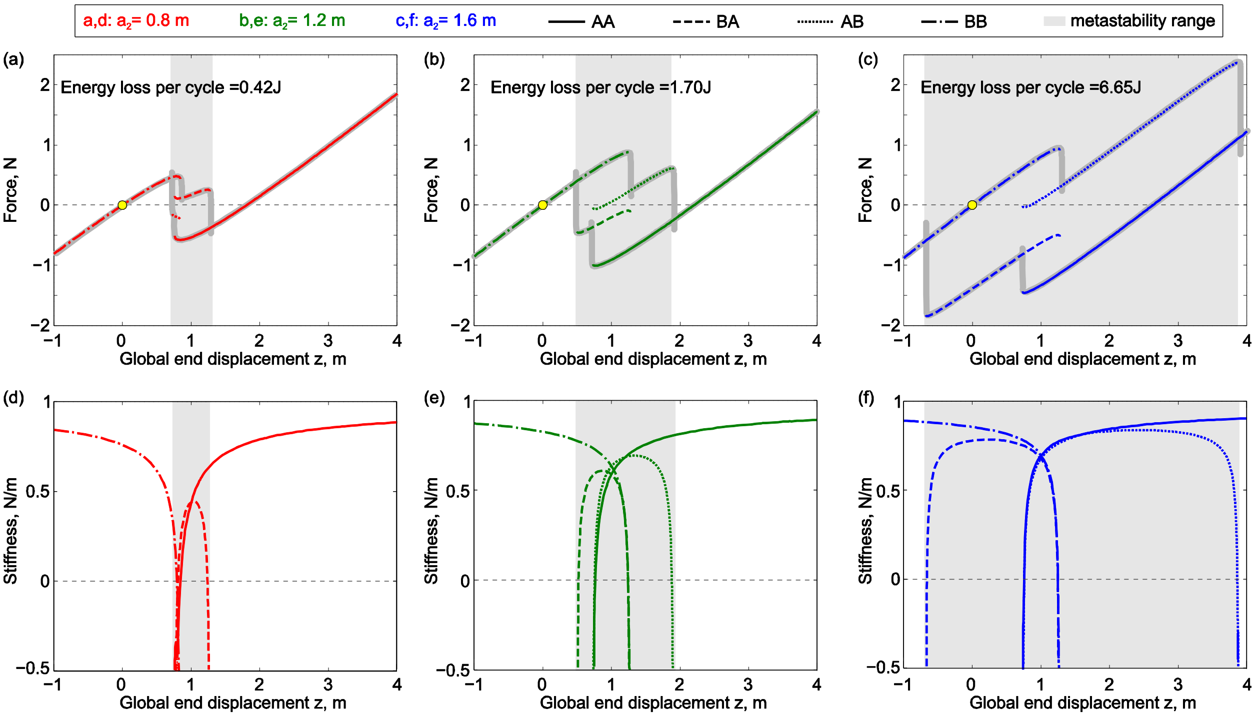

Figure 8. Profiles of (a,b,c) end force, and (d,e,f) stiffness as global end displacement is varied for the two-module metastructure. From left to right for both rows, the bistable spring span a_2 of the second module increases.

2.6.2 Analytical study of change in linear spring stiffness k_{2L}

Then, we utilize the model to explore how characteristics of the two-module assembly are influenced due to changes in linear spring stiffness k_{2L}. The parameters for the study are $k_1 = k_2 = 1$ N/m^3, $k_{1L} = 0.5$ N/m, $a_1 = 1$ m, $a_2 = 1.25$ m and $k_{2L} = [0.4\ 0.8\ 1.2]$ N/m. Similar to the plotting convention in Figure 8, the top row of Figure 9 presents the end force profiles together with hysteresis loop formed by quasi-static actuation while the bottom row shows the corresponding stiffness profiles for the two-module metastructure. In both rows of Figure 9 from the left-most column to the right-most column, the linear spring stiffness k_{2L} increases from 0.4 to 0.8 to 1.2 N/m. For the range of the linear spring stiffnesses k_{2L} employed in this parametric study, all three cases preserve the characteristic four distinct force profile paths per two-module assembly, as shown in Figure 9(a-c). As the linear spring stiffness k_{2L} increases, two primary trends are observed. First, the metastructure stiffnesses for very small or very large end displacements are seen to increase, Figure 9(d-f); this is in sharp contrast to the observations in the prior section that metastructure stiffness variation is negligibly influenced for the extreme end displacements as bistable spring span is changed. Yet, for displacements within the metastability range, the trends of global stiffness change are more intricate as linear spring stiffness is tailored. For example, as the linear spring stiffness k_{2L} increases, the metastable configurations labeled as AB exhibit broader spans of end displacement having very small positive or negative stiffness values, as shown in Figure 9(d-f) by considering the plots from left to right. These trends may be explained by considering that the effective stiffness of two springs in series is determined by the weaker link. Therefore, as the linear spring stiffness k_{2L} increases, the "negative stiffness" characteristic of the bistable spring constituent has greater influence on the module-level stiffness profiles, which is reflected in the profile for the two-module metastructure.

The second primary trend is that the metastability range decreases as linear spring stiffness k_{2L} increases. This finding is intuitive if we consider the limiting case in which the linear spring k_{2L} becomes extremely stiff. In this situation, the global end displacement is effectively connected directly to the bistable spring internal coordinate of the second module. Consequently, the metastability range for the second module will be zero, although, there is still the possibility of a finite metastability range of the two-module metastructure but this depends on the design parameters of the first module according to equation (7). Lastly, same as previous findings, hysteresis loops/energy dissipation per cycle decreases as metastability range decreases.

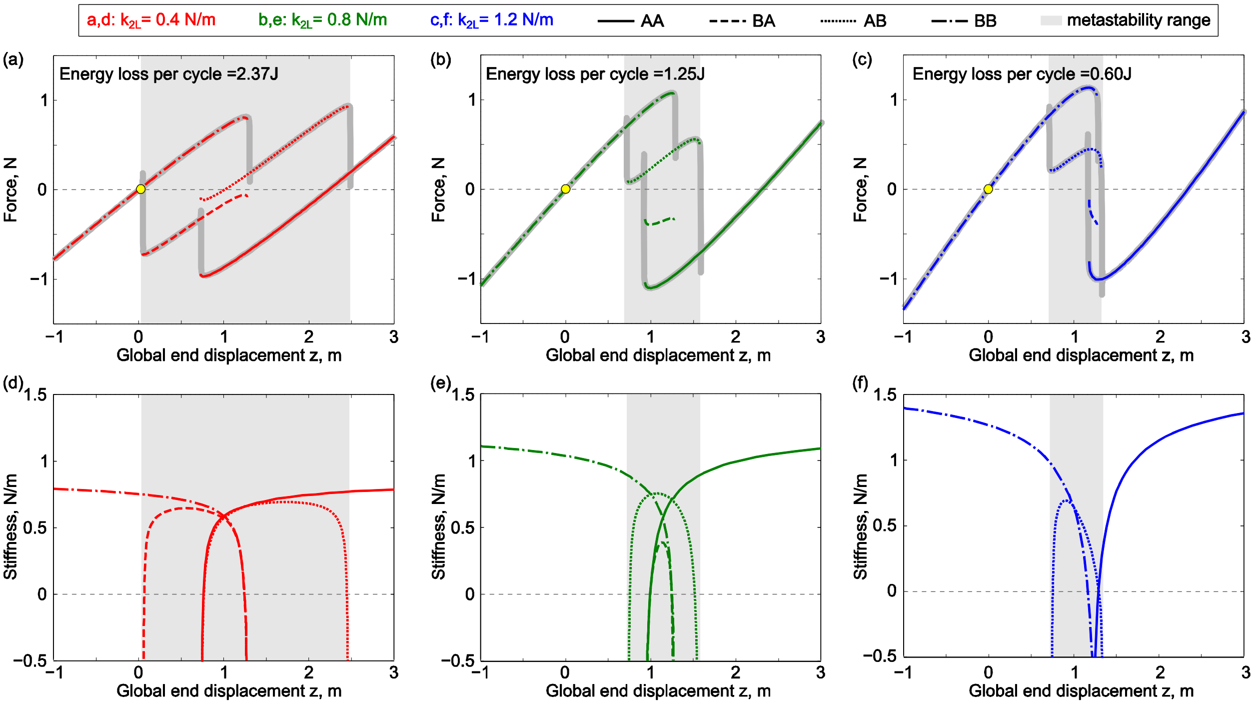

Figure 9. Profiles of (a,b,c) end force, and (d,e,f) stiffness as global end displacement is varied for the two-module metastructure. From left to right for both rows, the linear spring stiffness k_{2L} increases

2.6.3 Experimental parametric study

We employ an experimental two-module metastructure to examine the influences of changing the parameters that were investigated in the prior sections: linear spring stiffness and bistable spring span of one of the modules. The experimental studies are intended to verify the primary analytical observations as well as to gather meaningful insight about practical factors involved in assembling metastructures from our current proof-of-concept modules.

To begin, a series of experiments are conducted by varying the bistable spring span of module II while all other parameters of the metastructure remain constant. The span is changed by adjusting the compression distance on the buckled beam in module II. The measured force profiles for the four cases of bistable springs used bistable in module II are presented in Figure 10, showing that from case 1 to case 4, the span gradually increases. For completeness, Figure 10 also shows the relation of the spring span for module I with respect to those considered for module II in the following parametric study. In addition, note the feature that was discussed in the analytical parametric study which indicated that the peak force amplitude prior to the transition to negative stiffness gradually increases as the static equilibria span of the bistable spring of module II is progressively increased.

In Figure 11, the end force (top row) and stiffness (bottom row) profiles of the two-module metastructure are presented for all four cases of bistable spring span, as it is gradually increased from case 1 to case 4 considering the figure columns from left to right. In agreement with the analytical trends shown in Figure 8, we find that as the bistable spring span of module II increases from cases 1 to 4, the range of existence for metastable configuration AB noticeably increases. Due to the experimental constraints in realizing the metastable states from statically-stable configurations, the absence of the AB metastable configuration in Figure 11(a,b,e,f) does not necessarily indicate the AB configuration set does not exist, but rather that the AB profile does not include a statically-stable configuration that experiments could begin quasi-static profiling around. Considering Figure 11 further, also in agreement with analytical findings we find that the change in bistable spring span does not appreciably affect the stiffness of the metastructure for very small or very large end displacements, as seen in Figure 11(e-h): the maximum stiffness for such displacements remains around 300 N/m for all cases. However, the increase in the bistable spring span is observed to shift the location of the statically-stable equilibrium of configuration AA to higher values of displacement, from approximately 7.5 mm to 10 mm as shown in Figure 11. Each of these findings is in very good agreement with the observations made in the analytical parametric study by employing our mathematical model.

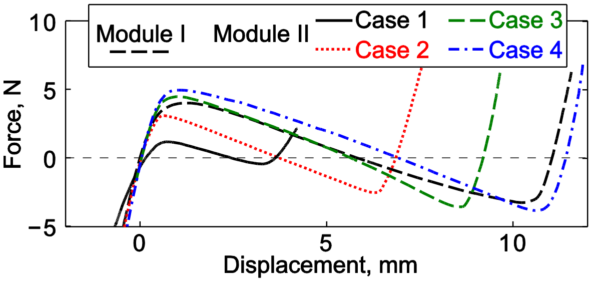

Figure 10. Force profiles of the bistable springs of modules I and II as the bistable spring displacement is varied. The dashed curve corresponds to the bistable spring force profile for module I, whereas the remaining curves are those employed for module II. The spans of the bistable springs used for module II increase from 1 to 4 as labeled in the plot.

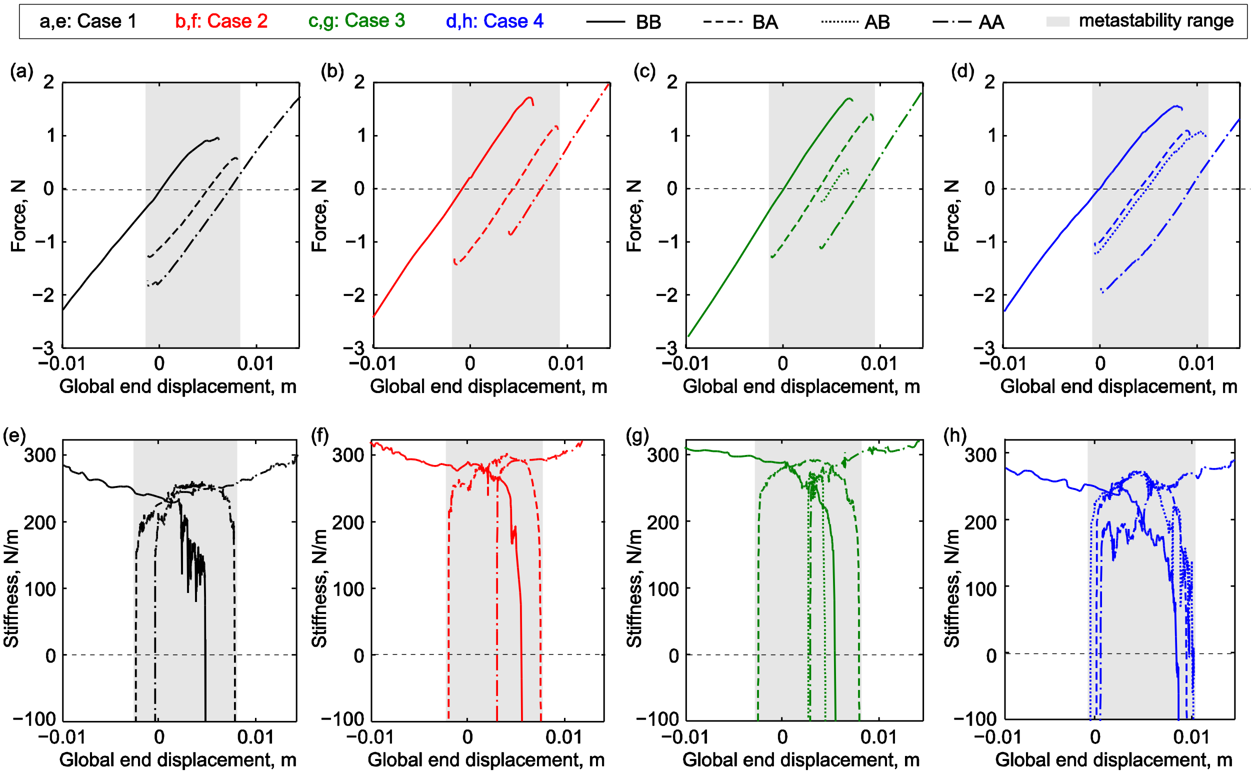

Figure 11. Measured profiles of (a,b,c,d) end force, and (d,e,f,h) stiffness as global end displacement is varied for the two-module metastructure. From left to right for both rows, the bistable spring span of module II increases from example 1 (far left) to example 4 (far right).

Experiments are then performed to investigate the influence of changing the linear spring stiffness of module II using the coil spring stiffnesses of 54 N/m, 77 N/m, 98 N/m, and 122 N/m, denoted here as cases 1 through 4, respectively, while all other metastructure parameters remain the same.

For comparison, the linear spring stiffness of module I was 122 N/m throughout the following evaluations. Figure 11 quantifies the trends observed in the measurements on how the metastability range of the two-module metastructure is affected as linear coil spring stiffness (solid bars/blue) and bistable spring span (dashed bars/red) of module II are varied. Cases 1 through 4 correspond to either increase in linear coil spring stiffness or increase in bistable spring span, where the latter results were considered in full detail via Figure 11. As depicted in Figure 11, the general trend is that the metastability range of a two-module metastructure increases as the linear spring stiffness decreases or as the bistable spring span increases. These findings are in accordance with the analytical observations described in the analytical and experimental parametric studies and examined in Figures 8 and 9. To maximally harness the mechanical properties adaptivity of the metastructure, a multitude of coexistent metastable states must be realized over a broad range of end displacements. The results of the parametric studies indicate that the linear spring stiffness and the span between bistable spring static equilibria are critical towards governing the breadth of the metastability range. Moreover, the findings indicate that even one module of a multi-module assembly may play a lead role in determining the metastructure properties by the adjustment of a single module-level constituent.

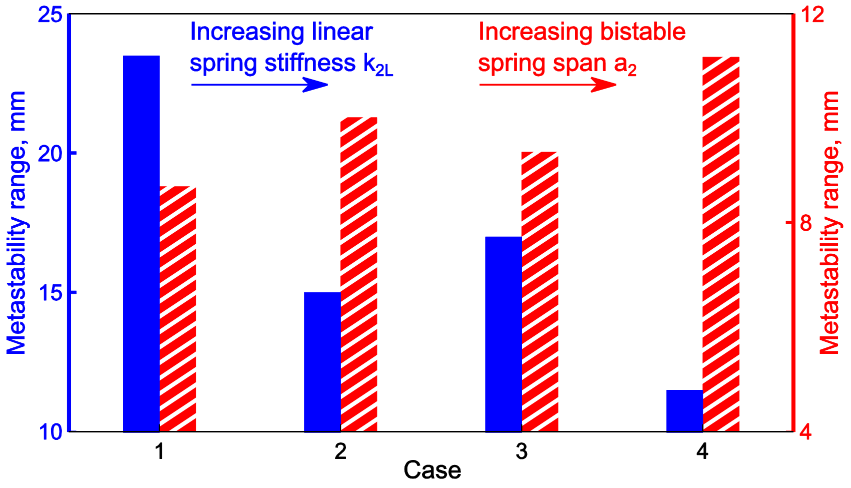

Figure 12. Metastability range as linear coil spring stiffness (solid/blue) and bistable spring span (dashed/red) varies.

Chapter 3

Harnessing the Metastable States of A Modular Metastructure for Programmable Mechanical Properties Adaptation

3.1 Chapter overview

Previous studies on periodic metamaterial systems have shown that remarkable properties adaptivity and versatility are often products of exploiting internal, coexisting metastable states. Motivated by this concept, in this chapter we seek to build upon previous foundational concept by redesigning the mechanical module in such a way as to investigate how the favorable system-level adaptivity and performance of modular metastructures should be tailored with the assembly of ***many*** metastable modules. In so doing, this presents the opportunity to explore how to best design such modular metastructures for a given set of targeted macroscopic characteristics. Thus, this research begins to establish a new local-global design framework whereby the local modules are designed such that a targeted global synergy is effected once the modules are assembled into modular metastructures. In the process of exploring this local-global framework, answers to several design-based questions are sought. These questions include (i) what degree of parametric heterogeneity is permissible or desirable towards realizing the target adaptivity performance, (ii) what types of heterogeneity are to be considered, and (iii) are such conclusions extensible to metastructures composed of any number of metastable modules?

To accomplish the research objective and explore the local-global design framework, a series of tasks are performed and discussed in the following sections. First, the experimental module created to facilitate the assembly of many such modules into metastructures is introduced, and gives evidence that the product of this design strategy may be a remarkable synergy at the macroscopic level. Then, a theoretical study provides insights to the qualitative persistence and evolution of metastable states and property adaptivity. Next, additional experimental evaluations elucidate how modularity can be exploited to invest metastructures with direct means for massive property change such as reaction force variation and tunable hysteresis. Finally, a genetic algorithm routine is developed and investigated to probe the parametric sensitivities exhibited with respect to achieving specific properties adaptivity goals, thus establishing rational means to locally design the metastable states of modules to realize targeted global metastructure performance once the modules are thereafter assembled.

3.2 Experimental module, assembly strategy, and exemplary properties adaptivity

Prior researchers have shown that inducing coexisting metastable states in mechanical systems is fundamentally accomplished using a bistable (negative stiffness) spring in series with a positive stiffness spring [2] [151] [157], Figure 13(a). Properly designed, the two, local minima of potential energy of the bistable component enables the module to possess two metastable states, whereby the macroscopic topology, z in Figure 13(a), remains the same while the reaction force F_i (and related properties such as stiffness) may be adapted. A module employing a bistable spring alone is insufficient to induce coexisting metastable states because the additional positive stiffness series spring introduces the means to equalize the macroscopic load at two coexisting internal configurations, which is the essential adaptation mechanism [151]. In this study, building upon the authors' prior study of assembling two such archetypal metastable modules together, a new one-dimensional metastable module is created and investigated so as to facilitate the assembly of many modules together into metastructures. This enables the evaluation of how the macroscopic properties of the metastructure are tailored due to the design and switching among the many metastable states, as sketched in Figure 13(b).

A schematic of the new module created here is given in Figure 13(c). The essential components for effecting metastable states are retained: a bistable spring in series with a positive stiffness spring. The bistable spring is generated by geometric constraints: four spring steel beams are bonded between an acrylic/PMMA housing and shuttle such that the distance between the housing and shuttle ($\delta \approx$13 mm) is less than the beam lengths prior to bonding ($\ell \approx$14 mm). In series with the bistable spring is a spring that connects the bistable shuttle, displaced by x, to the PMMA facing element which is acted upon by the end displacement z. This series spring force is due to tensioned elastic bands that interface the shuttle and facing components. Parallel assemblies are created by stacking and constraining the modules at the housing ends using alignment rods while a common, rigid guide rod governs the resulting metastructure end displacement z, as shown in Figure 13(c). Photographs of one experimental proof-of-concept module and multi module metastructure assembly are given in Figure 13(c) and (d), respectively.

Experiments are undertaken with the housing ends of assembled modules secured to an optical table (Newport RS 3000) while the guiding end displacements z are governed by a motion controller/stage system (Newport IMS500CC) moving at a rate of 100 μm/s with displacement resolution of 1.25 μm. The same experimental routine applies whether capturing data for an individual module or for a multi module metastructure. Measurements are taken for the one-dimensional end displacement z using a potentiometer (Novotechnik TR-100) and for the resulting reaction force F using a load cell (Measurement Specialties ELAF-TIE-100L) at the end displacement location. The load cell measurements pass through an analog, fourth-order low-pass Butterworth filter (DL Instruments 4302) at 10 Hz at the point of acquisition while all data is post-processed using a digital, second-order low-pass butterworth filter at 1 Hz.

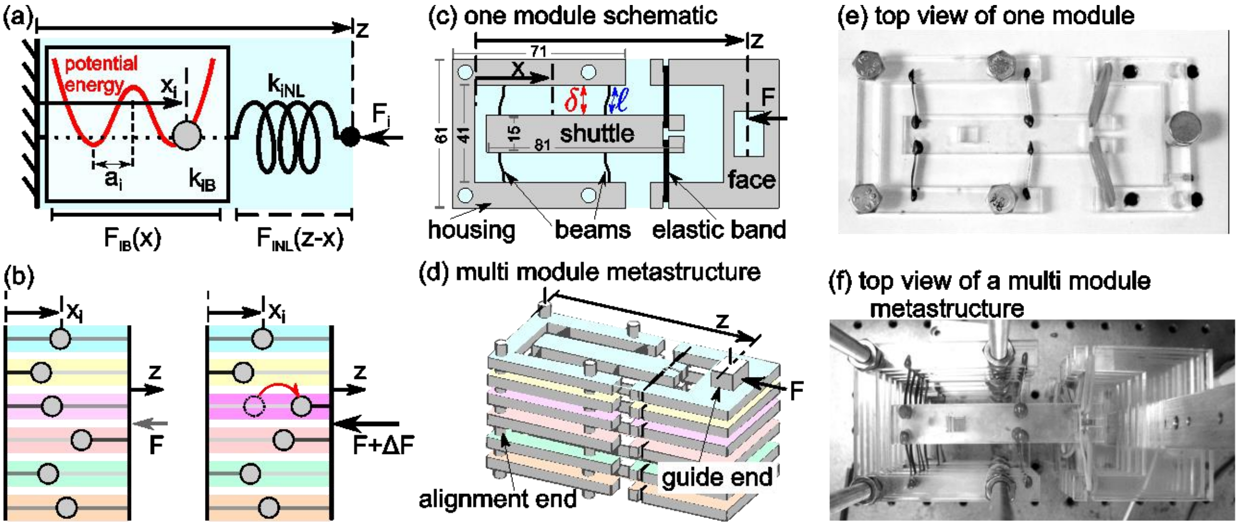

Figure 13. (a) Model schematic of bistable spring (double-well potential energy profile) in series with positive stiffness spring acted upon by end displacement. (b) Illustration of reaction force F adaptation when a one metastable module of a multi module metastructure transitions from one to another metastable state: the force is modified to $F+\Delta F$ while end displacement z is constant. (c) Schematic of experimental, mechanical metastable module. Dimensions are given in mm. (d) Schematic of multi module metastructure assembly and experimental implementation. (e) Top view photograph of one experimental module and (f) a multi module metastructure.

To first evaluate the efficacy of the new module design towards realizing coexisting metastable states and possibility for adaptivity growth in metastructure assemblies, experiments are conducted using the methods detailed above for an individual module, and then for metastructures assembled from two, four, and six modules in parallel. Figure 14 presents exemplary measurements of normalized reaction force as the end displacement is varied quasi-statically. Each curve indicates a metastable state; when multiple states are discovered, multiple experiments are conducted to measure them all. To measure each state, data collection is begun at an end displacement approximately halfway along the full range considered and then two measurements are taken where one involves reducing end displacement values and the other uses increasing end displacements from this interior starting point. The reaction force normalization used in plotting is with respect to the largest absolute force measured for the six module metastructure, which occurs around an end displacement z = 22 mm.

For the individual module results shown in the top panel of Figure 14, over a range of end displacements there are two coexisting metastable states that induce unique macroscopic mechanical properties. In other words, for topologically identical end displacements, the module may provide two distinct reaction forces. The metastable module design investigated here therefore meets the requirements for properties adaptation by effecting such necessary metastable states. Then, Figure 14 shows that modular metastructures of increasing number of modules produce a massive increase in the number of possible coexisting metastable states. In spite of a significant heterogeneity from module-to-module, the measurements uncover 4, 16, and then 64 coexisting metastable states for the two, four, to six module metastructures, respectively, which suggests that heterogeneity may play an important role to realize the many coexisting states. The consequence of the many metastable states is that near-continuous properties adaptivity is effected for particular macroscopic topologies. For example, the bottom panel of Figure 14 shows that around 8 mm end displacement for the six module metastructure, the reaction force may be tailored amongst an enormous number of values spanning the range from about -0.08 to 0.11 normalized force. As Figure 13(d) illustrates, the effort required to achieve such properties adaptation is the switching of internal metastable states amongst the assembled modules from initial to desired, final states/properties. Once the final state is realized, no additional active effort is needed to maintain the new macroscopic property unlike many active materials that require persistent electrical, temperature, or other interventions to sustain the tailored property. In addition, for these examples Figure 14 shows that each module and modular assembly effects more than one stable equilibrium (zero reaction force), which is a statically stable shape. The bottom panel of Figure 14 shows that the large number of metastable states and stable topologies for the six module metastructure gives rise to near-continuous stable shape change over a certain displacement range. In contrast to zero-stiffness structures that undergo large free displacements due to a lack of restoring forces [158], the modular metastructures retain viable stiffness at each stable topology, providing a means to "lock" in shape once the new stable form is realized. In a way, this property is similar to a reversible plasticity [159] realized using a strategic combination of elastic constituents. These results exemplify that effective module design -- providing coexisting metastable states -- leads to exceptional, synergistic properties adaptivity on the metastructural scale following strategic assembly, justifying the design concept and motivating closer investigation.

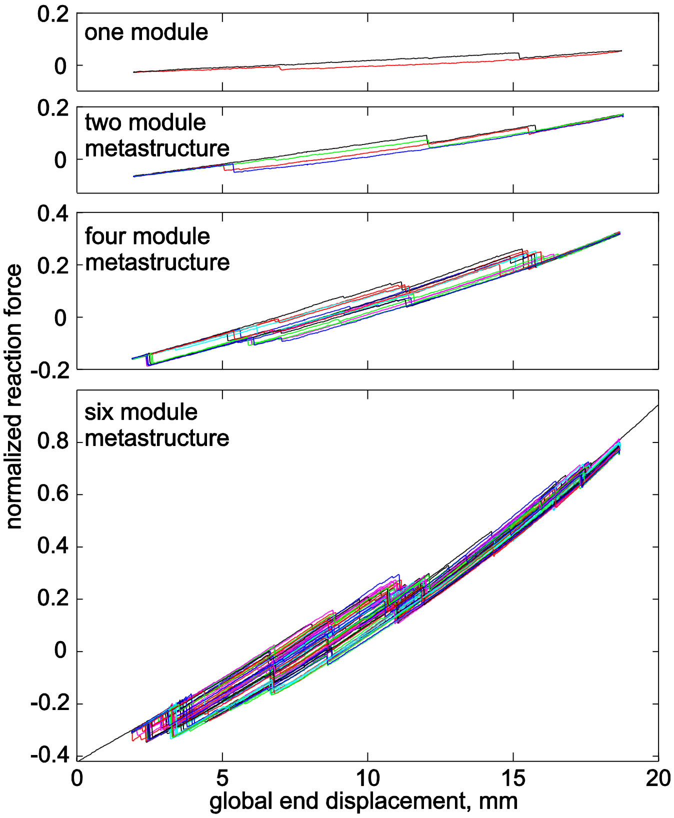

Figure 14. Normalized experimental reaction force as end displacement is varied. From top to bottom panels, measurements of one module, and then of two-, four-, and six module metastructures. Each curve is a metastable state.

3.3 Theoretical formulation and study

An analytical model of modular metastructures is formulated to verify and validate the intriguing experimental trends and, in Sec. 3.5, to explore characteristics of the metastructure design concept not currently accessible via the experimentation. Similar to previous analysis, for the ith module of an n module metastructure, the bistable spring force is approximated using $F_{iB} = k_{iB}x_i(x_i - a_i)(x_i - 2a_i)$ where the displacement of the shuttle is x_i, the stiffness coefficient is k_{iB}, and the distance between the stable equilibria is $2a_i$, denoting the "span" by a_i as the distance between one stable equilibrium and the central unstable internal configuration. Although this is an inexact expression for the true spring force exhibited between the guided-fixed beams and the shuttle, the cubic polynomial formulation is still qualitatively comparable to the exact profile [160] and usefully enables an analytical determination of the numerous metastable, force-displacement profiles without the need for nonlinear equation solvers or finite element modeling [161]. The forces exerted in the axis of end displacement by deforming the elastic bands are purely nonlinear [144], and are expressed using $F_{iNL} = k_{iNL}(z - x_i)^3$. Using the same theoretical formulation discussed in Sec. 2.4, analytical investigations can likewise be performed for the new system.

From the top to bottom panels, Figure 15 presents exemplary analytical results of the normalized reaction force F as the end displacement z is varied quasi-statically for an individual module, and then for two, four, and six module metastructures, respectively. To compute these results, the bistable spring stiffness coefficient values k_{iB} and span distances a_i are arbitrarily selected (k_{iB}= 2 N/m^3, a_i= 0.5 m) so as to emulate the qualitative trends of the measurements for the sake of illustration. The remaining coefficients include notable heterogeneity. Specifically, stiffness coefficients k_{iNL} are randomly selected from a normal distribution of values having standard deviation of 1 N/m^3 and mean of 0.6 N/m^3; the attachment offset distances d_i are likewise randomly selected where standard deviation is 0.07 m and mean is 0 m. For a given module, these random variations influence the extent of end displacements across which coexisting metastable states occur which is the most apparent distinguishing factor among fabricated modules once assembled.

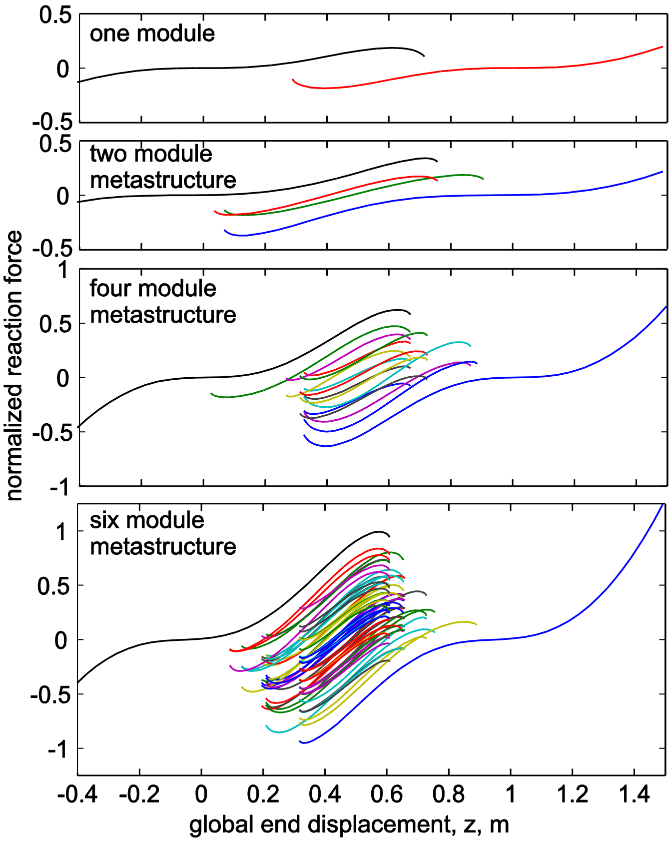

Figure 15. Theoretical predictions of normalized reaction force *F* as end displacement *z* is varied. From top to bottom panels, results for one module, and then of two-, four-, and six module metastructures. Each curve is a metastable state.

The trends observed in Figure 15 are in overall good qualitative agreement to the measurements in Figure 14 with respect to the exponential growth of the total number of coexisting metastable states as greater numbers of modules are assembled together. For theoretical exploration purposes at the current phase of concept development, this level of agreement is sufficient; future model formulations of the current platform may account for the precise bistable spring behavior which is slightly more intricate that the cubic polynomial expression employed here [160]. According to the theory, at most 2^n coexisting states are possible for an n module metastructure. Indeed, the analytical results show that the growth of the total number of metastable states is robust to the appreciable heterogeneity applied via coefficient perturbations from nominal values. Comparable to measurements, the bottom panel of Figure 15 shows that a metastructure assembled from six modules effects a capability for near-continuous mechanical properties adaptivity and shape change, both over a given extent of values. These features are specifically enabled by the modularity of the system. In contrast with periodic metamaterial systems which may possess large multistability but have limited means to exploit or explicitly realize the various states to tailor properties, modular metastructures (composed of even only a few modules) facilitate the direct creation of a vast number of metastable states that represent unique mechanical properties useful for adaptation purposes. It is clear that by developing a suitable module possessed with coexisting metastable states, the assembly of such constituents promotes a synergistic growth of structural adaptivity, even accounting for considerable parametric heterogeneity.

3.4 Harnessing transitions among metastable states for properties adaptation

Enormous properties adaptivity and stable shape change are desirable features for many advanced engineering systems, including for morphing aircraft [124] and for structures with dramatic dynamics-based energy transfer features [162] [163]. Beyond the favorable static characteristics of the modular metastructures exhibited in Sec. 3, here experiments are conducted by subjecting a six module metastructure to slow, periodic excitation to explore intelligent passive-adaptation capabilities in response to time-varying external influences. For example, such valuable transformations include maintaining a constant global topology while an applied force changes or maintaining a constant reaction force while an applied end displacement is varied.

To illustrate the prior, Figure 16(a) plots the reactions forces from 13 trials of transitioning an experimental six module metastructure from a common initial metastable state (0-0-1-0-1-0) to a common final state (1-0-0-1-0-1), where 0s and 1s indicate the bistable springs are buckled away from or towards the facing ends, respectively. The experiments are conducted by maintaining an 8 mm end displacement while sequential, manual actuations (by direct point force application) upon the shuttles induce switches amongst internal configurations, and hence amongst global macroscopic properties. For example, one experiment follows the transition series (0-0-1-0-1-0), (0-0-1-0-0-0), (0-0-0-0-0-0), (0-0-0-1-0-0), and so on until the state (1-0-0-1-0-1). The unique plotted curves, Figure 16(a), are therefore the reaction forces generated for 13 different trials of transitions from common initial to common final states, and therefore common reaction forces. The curve shading from light to dark indicates increasing mean value of force with respect to the 13 trials. Reaction forces are normalized to initial common values, while time is normalized according to the number of discrete, sequential transitions. For these experiments, five discrete transitions are executed, leading to six stages for each trial.

The results in Figure 16(a) make clear that modularity invests a significant opportunity for reacting to applied forces in unique ways that maintain global metastructure topology. In this example, transitioning from common initial to common final reaction forces may be undertaken using an enormous number of possible series of reaction force variations. Thus, considering the applied force conditions with respect to maintaining a desired global topology, an appropriate transition series may be selected. For instance, an increasing/decreasing applied force may be best reacted to using the transition series shown as the darkest curve, whereas a decreasing/increasing applied force may be best reacted against using the lightest curve transition path. In this way, the metastructure may most effectively adapt to different environment loading conditions while the global topology is fixed. Indeed, assessing the combinatorics of the permutations [164], the number of possible adaptable transition series for metastructures undergoing g discrete transitions from common initial to common final reaction forces is g! (here, 5! = 120).

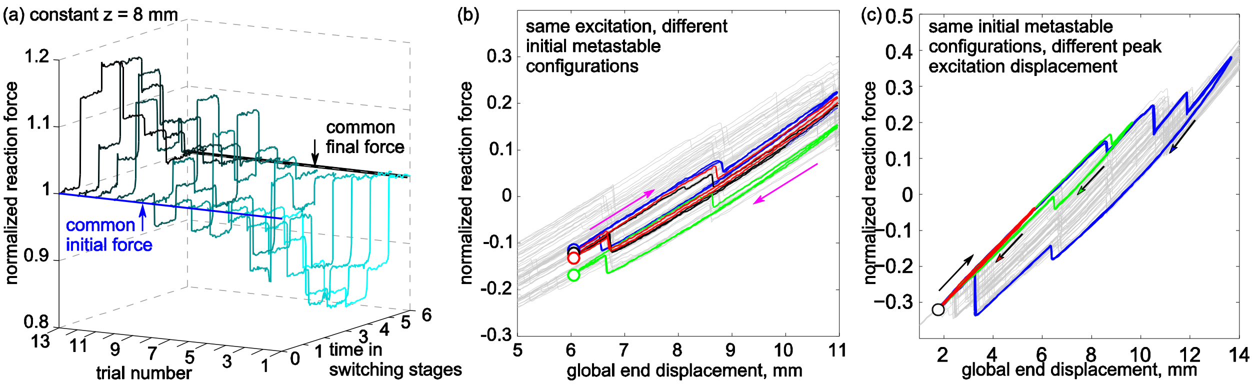

Figure 16. Experimental measurements. (a) Transitioning a six module metastructure from common initial to common final states via different orders of transitions. Light to dark line shading indicates increasing mean value of reaction force with respect to all trials. (b) Distinct hysteresis loops having common minimum and maximum global end displacements, but unique sets of metastable states throughout slow actuation cycles. (c) Distinct hysteresis loops having common starting end displacement but qualitatively distinct unloading paths due to different maximum end displacement. In (b,c), background grey curves are quasi-static reaction force measurements; thick curves (colored) show two cycles of data, indicating repeatability to the measurements; circles indicate starting points.

When the end displacement of the metastructure is guided periodically, the resulting loops of hysteresis are found to be unique based upon the switches in state that are effected due to loss of stability from one metastable state to the next. The measurements in Figure 16(b) from a six module metastructure exemplify the case in which the same loading and unloading end displacement is prescribed but different starting sets of internal metastable configurations lead to different hysteresis over the course of the slow (near quasi-static) actuation cycle. In this example, the measurements begin for an end displacement near 6 mm (circle points). During the slow actuation cycles, distinct, steady-state hysteresis loops are uncovered, four of which are shown in Figure 16(b) by the thick curves plotted over the thin, light grey plot of the static measurements of the six module metastructure mechanical properties (previously given in Figure 14). The hysteresis loops are seen to vary in terms of the energy loss per cycle (area enclosed in the Lissajous curves) as well as in terms of the mean value of reaction force, which extends the properties adaptivity potential of recent advancements in metamaterials [165]. Thus, by exploiting these "hidden" degrees-of-freedom [166], the macroscopically-observable hysteresis of the metastructure may be leveraged in novel ways.

Figure 16(c) presents measurements when the six module metastructure is slowly actuated by an end displacement starting near 2 mm. Different amplitudes of actuation are applied from the common starting position, before the unloading half cycle. The results show that the coexistence of many metastable states leads to distinct hysteresis based upon which internal transitions are induced during the cyclic loading. Thus, rather than rely solely upon conventional damping mechanisms such as Joule heating to dissipate the cyclic, actuation energies, the modular metastructures leverage a feature similar to a "reversible plasticity" wherein the internal instabilities promote tunable energy decay to "high frequency [dissipative] modes" even in the near quasi-static actuation scenario [159]. Comparable phenomena are observed in the experiments when metastructures are actuated starting from different initial end displacements. Collectively, enormous and adjustable hysteresis is effected based upon the initial end displacement and initial metastable state. Moreover, in spite of the considerable heterogeneity in the experimental metastructures, it is worth highlighting that the results in Figure 16(b,c) overlay two cycles of measurements which shows that the adaptable characteristics are repeatable and consistent.

3.5 Design of multi module metastructures

The results shown in Secs. 3.2 through 3.4 indicate that the static and quasi-static characteristics of modular, mechanical metastructures exhibit enormous potential for adaptivity. Even in this conceptual phase of development, questions could be raised as to the viability of realizing many metastable states that yield desirable property adaptation. For example, to "program" the desired adaptivity feature or its level in this local-global design framework, (i) what degree of parametric heterogeneity is permissible and/or desirable, (ii) what types of heterogeneity are permissible, and (iii) are these conclusions consistent for multi module metastructures of any number of assembled modules? In the face of near open-ended opportunity for parameter selection, a design methodology is needed to take this structural/material assembly concept beyond a seminal phase. To explore these parametric influences, a genetic algorithm (GA) is devised based upon the analytical model foundation. According to the formulation, the model uses the most reduced set of design variables possible to describe the salient factors that govern the macroscopic properties of the metastable modules: the bistable spring span a_i, the stiffness of the bistable and attachment springs, k_{iB} and k_{iNL}, respectively, and the attachment offset distance d_i. The genetic algorithm is first composed to evaluate and optimize performance measures by manipulating and evolving the bistable spring stiffness k_{iB} and span a_i design variables over the course of 50 generations each having a population of 100 individuals, where an individual is a six module metastructure. The algorithm is developed in-house and is devised upon an architecture described by Haupt and Haupt [167]. From one generation to the next, the selection/retention rate is 50% and the mutation rate is 20%, which together promote an aggressive search protocol useful for performance planes that exhibit multiple local minima.

3.5.1 Designing metastructures with equi-distant stable equilibria

Two, prominent adaptivity characteristics were uncovered in Secs. 3 and 4 regarding multi module metastructures: near-continuous change of stable topologies while reaction force is zero, or near-continuous change in reaction force while the global end displacement topology is prescribed.

Therefore, the GA is programmed to optimize relevant features of these adaptivity characteristics. In the following example, the first performance measure considered is the achievement of an equal spacing between adjacent statically stable equilibria of the six module metastructure, as illustrated in the top left panel of Figure 18. Thus, a metastructure with the best "fitness" possible would have exactly equi-distant adjacent stable equilibria (e.g., with stable equilibria locations at α_j where α is the spacing distance and $j = 1,2, \ldots$). Since each of the six modules possess stiffness and span parameters, this suggests that 12 design variables are required to evaluate this performance measure using the GA. To circumvent difficulties encountered with GAs using many free variables, a novel statistical approach of GA utilization is undertaken here. Thus, a large range of permissible values are initially prescribed for the selection of k_{iB} and a_i, but, for a given module, the precise parameter value is selected at random within the range. By this modification to traditional GAs, it is recognized that complete convergence is not ensured. On the other hand, the findings presented below show that important design-based knowledge emerges from the statistics of the steadily convergent results.

Figure 17 presents the results of the GA towards achieving six module metastructures designs having equally spaced adjacent statically stable equilibria. Each data point in Figure 17 is the statistic with respect to the mean value for all individuals of the generation (triangles) or the value computed for the best-fit individual of the generation (circles). Note that because each individual is a six module metastructure, each individual has a set of six bistable spring stiffnesses and six spring spans, and thus yields statistics that characterize those parameter value distributions. The top row shows how the mean value of the six (a) bistable spring stiffnesses and the (b) bistable spring spans relatively converge over the course of the GA routine. It is seen that the generation means of the mean bistable spring span values, Figure 17(b), converge towards a value around

0.28 m while the best-fit individual means converge towards a slightly smaller value nearer to 0.23 m. Together, these trends demonstrate the importance of appropriate selection of span values towards achieving equally spaced stable equilibria. In contrast, while the generation means of the bistable spring stiffness values, Figure 17(a), converge to around 1.7 N/m^3, the best-fit individual mean values are seen to vary considerably from one generation to the next. Such low correlation between the convergence of the mean values for the whole generation of individuals and the mean value represented by the best-fit individual indicates that the bistable spring stiffness plays little role towards successfully meeting the target performance measure of equi-distant stable equilibria. The fact that the generation mean itself converges simply illustrates a conventional fact of statistics that large, randomly selected variables from uniform distributions of continuous values exhibit common means when the range of permissible parameter values is bounded [168]. Similarly as with the mean itself, Figure 17(c,d) find that the mean difference among the ordered parameter values is loosely correlated for the bistable spring stiffness but strongly correlated for the bistable spring span, which supports the prior conclusions.

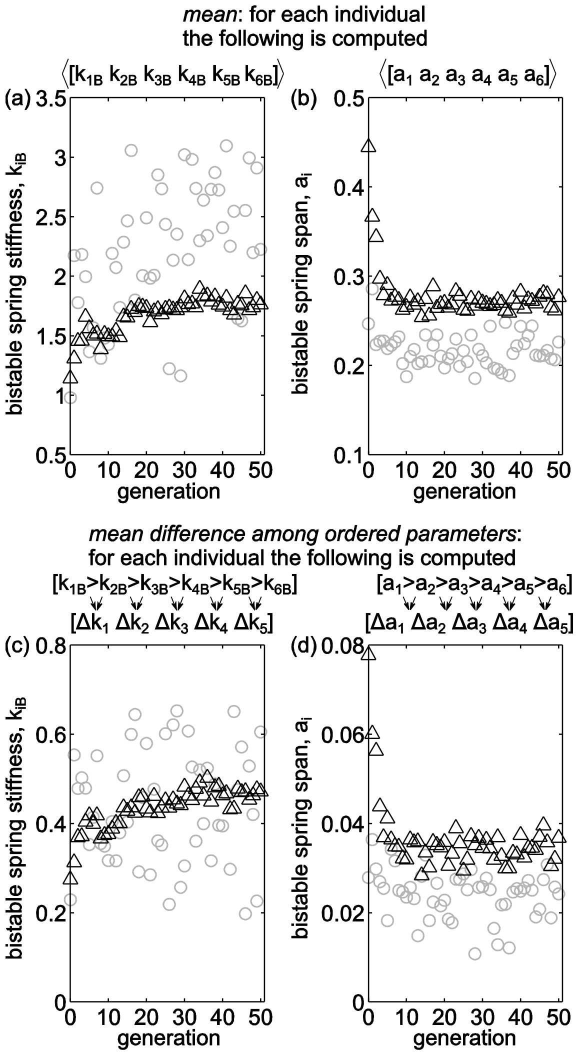

Figure 17. GA results for equi-distant stable equilibria. Design variable statistics, showing triangles as the mean statistics for a given generation whereas circles are the statistics according to the best-fit individual of that generation. (a) The mean of the six bistable spring stiffnesses, (b) the mean of the six bistable spring spans, (c) the mean difference among the ordered values of bistable spring stiffness and the corresponding statistic in (d) for the bistable spring span.

Figure 18 plots the statistics of the design variable (a) range, (b) mean, and (c) ordered difference for all individuals of the final generation as produced by the GA. The horizontal axes show the respective statistics computed for the bistable spring stiffnesses, whereas the vertical axes are those statistics for the bistable spring spans. Each data point is the statistic computed for one of the 100 individuals of the final generation and the data point shading varies from light to dark for increasing fitness of the individual. From this evaluation throughout Figure 18(a,b,c), the concentrations of parameter values for the bistable spring spans (i.e., concentrations along vertical axes), notably for higher-fitness individuals, exemplify that particular range, mean, and mean difference among the ordered spring span design variables of the six module metastructure are needed to ensure that the stable equilibria are as equally spaced apart as possible. In contrast, the assessment in Figure 18(a,b,c) verifies the observation from Figure 17 that the bistable spring stiffness value selection is not as important towards achieving this particular performance objective. Therefore, by the utilization of the genetic algorithm in such a novel, statistical manner, important insights may be derived to make design decisions that result in the sought-after performance and properties adaptivity of multi module metastructures.

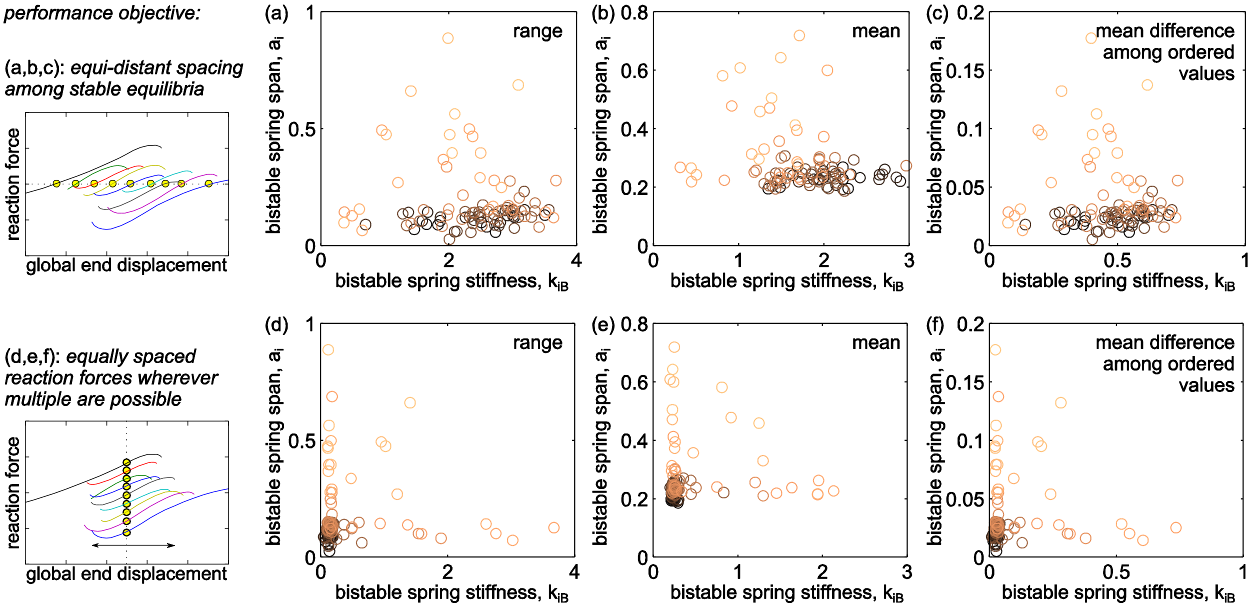

Figure 18. In (a,b,c), the performance objective is equi-distant spacing among stable equilibria of a given six module metastructure. In (d,e,f), the objective is equally spaced reaction forces while the global end displacement is fixed. The left-most panels illustrate the performance objectives according to the particular mechanical properties shown as circle points on the full profiles. In (a-f), design variable statistics of all 100 individuals in the final generation produced by the GA. Shading from light to dark shows increasing fitness towards achieving the performance objective. (a,d) Range, (b,e), mean,

and (c,f) mean difference among the ordered design variable values as plotted in terms of the bistable spring stiffness and bistable spring span.

3.5.2 Designing metastructures with equally incremented reaction force levels

Then, considering the second performance measure, the GA is programmed to optimize the mechanical properties by pursuing an equal spacing between adjacent reaction force levels of a multi module metastructure when the global end displacement is prescribed, illustrated for clarity in the bottom left panel of Figure 18. In other words, for any global end displacement of z_0 where multiple metastable states occur, the GA aims to identify a metastructure design having adjacent reaction forces equally spaced by a consistent force increment ΔF. The design variables and GA settings are the same as those described above, and the results of the algorithm for a six module metastructure are shown in Figure 19. In contrast to simply achieving equi-distant stable equilibria, the findings in Figure 19 indicate that both the bistable spring span and the bistable spring stiffness are essential design variables to strategically select towards realizing equally incremented levels of metastructure reaction force. Figure 19(a,b) show that the generation mean values of the bistable spring stiffness and span, respectively, both converge to respective values as the GA optimization proceeds. Likewise, the results of Figure 19(c,d) find that the ordered parameters are also required to exhibit certain mean differences, as evidenced by the statistical convergence of the generation mean values over the course of the GA evolutionary computations. Figure 18(d,e,f) presents the set of statistics produced by the final GA generation towards achieving equally spaced reaction forces across the range of end displacement for which multiple forces are possible. The higher performing individuals (darker shaded data) of this last generation are seen to cluster to particular statistical regimes for both design variables in agreement with the overall evolutionary results shown in Figure 19. These results indicate that the selection of bistable spring stiffnesses k_{iB} and spans a_i, among the six modules of a given metastructure, must comply with particular statistical properties in order to achieve the preferred equal spacing between adjacent reaction forces. Thus, more stringent design variable control is needed to realize this performance measure when compared to the design variable sensitivities involved towards effecting equi-distant stable equilibria.

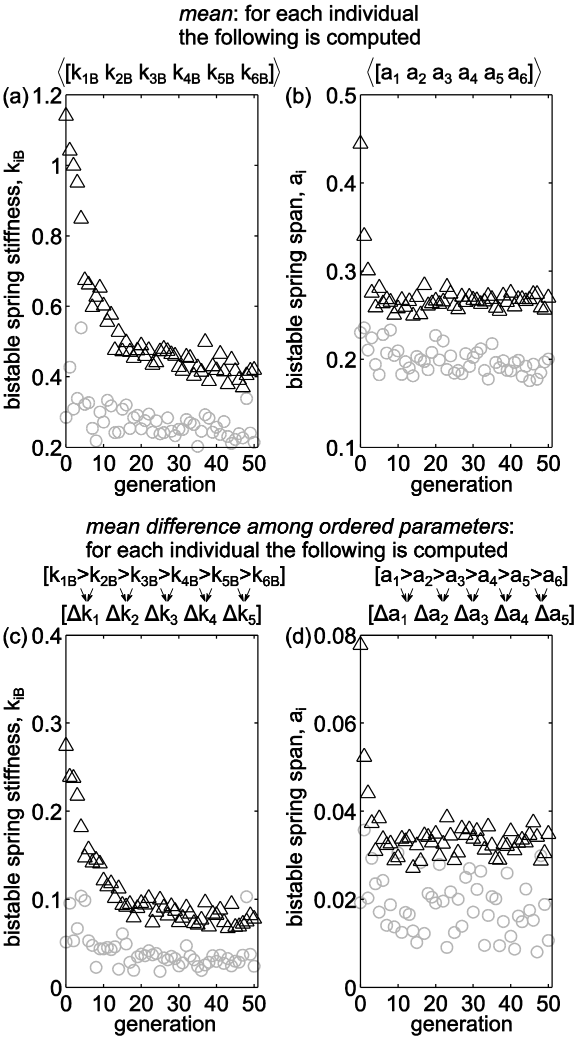

Figure 19. GA results for equally spaced reaction force levels. Design variable statistics, showing triangles as the mean statistics for a given generation whereas circles are the statistics according to the best-fit individual of that generation. (a) The mean of the six bistable spring stiffnesses, (b) the mean of the six bistable spring spans, (c) the mean difference among the ordered values of bistable spring stiffness and the corresponding statistic in (d) for the bistable spring span.

3.5.3 Influence of the number of assembled metastable modules

The findings in Secs. 3.5.3 and 3.5.2 elucidate the roles of two key design variables towards achieving target properties adaptivity or topological variation in six module metastructures. Yet, it may be asked how general such conclusions are, namely whether they are extensible to metastructures assembled from any number of metastable modules. To assess such an influence of scalability, the second performance metric of equally spaced levels of reaction force is re-evaluated by the GA, considering six and twelve module metastructure platforms. Based on preliminary results, it was determined to introduce an additional design variable to the optimization routine, namely the attachment offset distance d_i, while the GA algorithm again considered 100 individuals in each of 50 evolutionary generations.

Figure 20(a,b) plots the values of the design statistics for the range and mean, respectively, of the mean generation result for the six module metastructure, while Figure 20(c,d) presents the corresponding data for the twelve module metastructure. The shading of the line from first (triangle) to last (circle) generation is indicated by increasing darkness to highlight the trajectory of the GA over the course of the evolutionary routine. It is seen that the strategic selection of bistable spring stiffnesses and spans plays an appreciable role towards realizing this performance metric for the six module platform. This is evident in Figure 20(a,b) based on the observation that the statistics for the range and mean values of bistable spring stiffness and span converge as the GA routine proceeds, while in contrast the attachment offset distance statistics exhibit poor consistency in value from one generation to the next (i.e., much greater variation in the trajectories in the vertical axis).

Yet, considering the findings for the twelve module metastructure as shown in Figure 20(c,d), a different conclusion may be drawn. In fact, from these results, the role of the attachment offset distance is apparent since the GA trajectories exhibit undeniable convergence in the statistics for all three design variables. Because the final generation mean values of the statistics for the bistable spring stiffness and span are nearly identical when comparing the six and twelve module metastructures, the role of the number of assembled modules is therefore to introduce an important, new design variable influence in terms of the attachment offset distance. Collectively, the discoveries of this section reveal important sensitivities of multi module metastructure design towards achieving performance measures, such as prescribed stable topological change and preferred adaptation in reaction force by transitioning among the many metastable states. Although the concept of utilizing an assembly of metastable modules to create metastructures may potentially introduce an open-ended design problem, it is found that strategic design variable selection -- in a statistical sense -- is an effective means to realize target adaptation performance. Future efforts of this research will pursue further insights on the interplay between statistics and design as it relates to the development of modular metastructures possessing target performance and functionality.

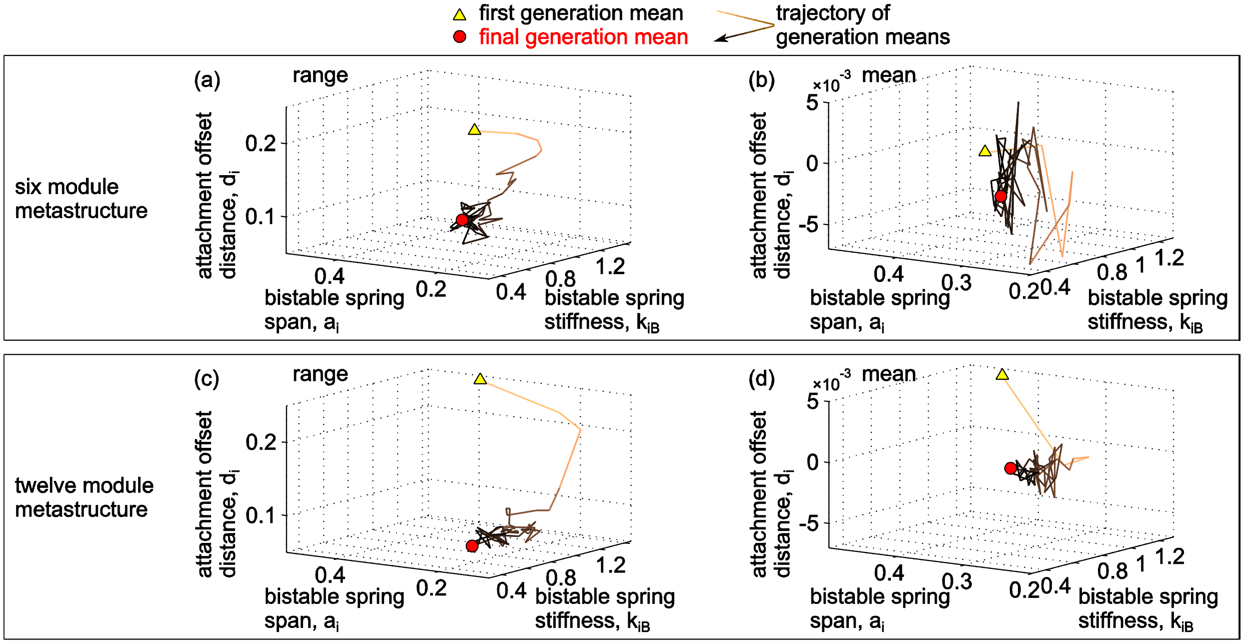

Figure 20. Generation mean design variable statistics over the course of 50 evolutionary generations. Shading from light to dark shows increasing generation number. Results in (a,b) are for the six module metastructure while those in (c,d) are for the twelve module metastructure. In (a,c) are the design variable ranges, while (b,d) show the design variable means.

The design concept presented here suggests that great potential is effected by the assembly of metastable modules into mechanical metastructures. This paper presents one exemplary realization of a fully-functional (i.e., adaptable) module, but it is recognized that combining a bistable spring/elasticity in series with an additional non-negative stiffness spring/elasticity has many possible module-based embodiments. This includes magnetoelastic interactions within structural materials [44] or architected material systems [46] [169] [170], and material-type building blocks with voids [165]. These recent innovations exploit periodic designs and the potential for internal instabilities in the periodic arrangements to result in macroscopic adaptivity. In contrast, the approach established here is to design the modules at the local level to facilitate a prescribed global synergy in performance and functionality once thereafter assembled. By the design investigation of Sec.3.5, it is seen that this method facilitates macroscopic features in a rational way useful for engineering design purposes. In summary, this investigation shows that modularity in an assembled structural system invests direct means to create and harness the metastable states of metastructures for programmable properties adaptivity. Experimental and analytical results exemplify that near-continuous properties adaptivity and stable topology change are effected as the number of assembled modules increases. The measurements also uncover opportunities to realize adjustable hysteresis (hence, energy dissipation) by harnessing the vast number of metastable states. Although the development of multi module metastructures poses interesting design-based challenges, the incorporation of the analytical model into a novel genetic algorithm routine demonstrates that the achievement of target global metastructure performance characteristics are met for preferred statistical distributions of key design variables at the local level, thereby closing the open-ended-ness of the design problem and guiding future assembly strategies. Altogether, this research shows that a new concept using building blocks having an essential variation of mechanical properties (coexisting metastable states) promotes enhanced and synergistic adaptivity via assembled, modular metastructures, which leverage design variable heterogeneities to achieve target performance measures.

Chapter 4

Dynamics of Metastable Module: Analysis and Experiment

4.1 Chapter overview

Previous investigations focus on mechanical properties adaptation afforded via metastability. Next research question we'd like to address is what are the dynamical responses of the assembled metastructure. To that end, we first study the vibration of a unit metastable module consists of a linear oscillator coupled with a bistable oscillator. The method of harmonic balance and perturbation analysis are used to predict the existence and stability of the bistable device interwell vibration. The influences of important parameters on tailoring the system response are investigated. We demonstrate analytically that for excitation frequencies in a bandwidth less than the natural frequency of the uncoupled linear oscillator having net mass that is the combination of the bistable and linear bodies, the bistable oscillator dynamics may be substantially intensified as compared to a single (individual) bistable oscillator. In addition, the coupled metastable module may introduce a stable out-of-phase dynamic around the natural frequency of the uncoupled linear oscillator, providing a second interwell response not possible when using a single bistable oscillator. Key analytical findings are confirmed through numerical simulations and experiments, validating the predicted trends.

4.2 Mathematical formulation of the unit metastable module

4.2.1 Governing equations

A bistable oscillator of mass m_1 is coupled to a linear oscillator of mass m_2 which is harmonically excited through base excitation $\ddot{z}(\tau) = -Z_0 \cos(\Omega\tau)$, as depicted in Figure 21. The governing equation for the system can be expressed as

$$m_1(\ddot{x} + \ddot{y} + \ddot{z}) + d_1\dot{x} - k_1x + k_3x^3 = 0 \qquad \text{(Eq. 9)}$$

$$m_2(\ddot{z} + \ddot{y}) + d_2\dot{y} + k_2y - d_1\dot{x} + k_1x - k_3x^3 = 0 \qquad \text{(Eq. 10)}$$

where x is the relative displacement between the linear oscillator mass and bistable inertial mass, and y is the relative displacement between the linear oscillator and base. The double well potential of the bistable device can be expressed as $U(x) = -\frac{1}{2}k_1x^2 + \frac{1}{4}k_3x^4$, where x is measured from the unstable equilibrium of the bistable device.

After substitution of equation (10) into equation (9) and nondimensionalization, the governing equations become

$$x'' + (1+\mu)f\gamma_1x' - (1+\mu)f^2x + (1+\mu)f^2\beta x^3 - \gamma_2y' - y = 0 \qquad \text{(Eq. 11)}$$

$$y'' + \gamma_2y' + y - \mu f\gamma_1x' + \mu f^2x - \mu f^2\beta x^3 = p\cos\omega t \qquad \text{(Eq. 12)}$$

where the parameters are defined as

$$\omega_1^2 = k_1/m_1;\ \omega_2^2 = k_2/m_2;\ \mu = m_1/m_2; f = \omega_1/\omega_2; p = Z_0/\omega_2^2$$

$$\gamma_1 = d_1/m_1\omega_1;\ \gamma_2 = d_2/m_2\omega_2;\ \ \omega = \Omega/\omega_2\ ; \beta = k_3/k_1; t = \omega_2\tau$$

and the operator (●)' represents derivative with respect to nondimensional time t.

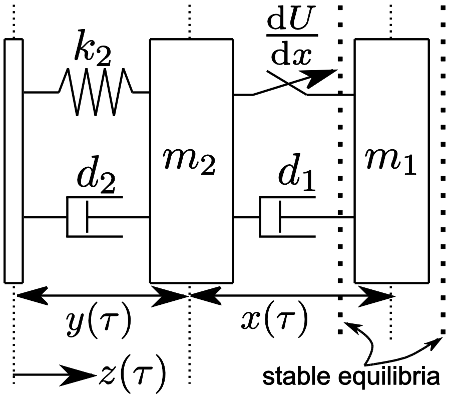

Figure 21. Base-excited linear-bistable metastable module.

4.2.2 Solution formulation by harmonic balance

Harmonic balance method (HB) is one of the mostly used method for analyzing nonlinear systems. It's also known as the Fourier-Galerkin method, since it consists in the application of the Galerkin method with Fourier basis functions. The main idea behind the method is to "balance" the different harmonics terms arising in the equations of motion due to nonlinearities. The main advantage of HB is when low orders of approximation are sufficient to obtain an accurate solution, which usually holds for smooth nonlinearities. The concept "harmonic balance" was first introduced by Kryloff and Bogoliuboff [171] by performing linearization of nonlinear dynamical equations with single harmonic term approximation. Later on, in the 1960s, Urabe [172] demonstrated the convergence of the method for Fourier approximations truncated to several harmonic. Since then, several adaptation and extension of the method have been proposed by researchers such as incremental HB [173], adaptive HB [174] as well as coupling HB with continuation schemes [175], just to name a few. Due to the effectiveness, HB balance and its extensions found their success on numerous applications. In electrical engineering, Kundert and Sangiovanni-Vincentelli [176] discussed its advantage over time-domain simulations for nonlinear circuits; Genesio and Tesi [177] derived analytical expressions for regions of chaotic behaviors of Lur'e systems; Stanton et.

al. [178] analytically predicted the existence, stability, and influence of parameter variations on the intrawell and interwell oscillations of bistable piezoelectric inertial generator; and Fang [179] applied HB method on a class of switched linear system which are commonly find in DC-DC converters and derived critical conditions to trigger bifurcation phenomena. In aerospace engineering, HB method was successfully applied to aeroelastic systems: Shen [180] analyzed the wing-control surface flutter; Liu and Dowell [181] studied the response of a two-dimensional airfoil including a control surface with freeplay placed in an incompressible flow; Lee et. al. [182] investigated limit cycle oscillations of a two-degree-of-freedom airfoil motion with cubic nonlinearity in the restoring forces; Dimitriadis [183] provided a comparative review of HB method applied to nonlinear aeroelastic systems. For aerospace engineering, HB method is also used to analyze fluid dynamics with unsteady nonlinear flows [184] with applications for nonsynchronous vibrations in turbomachinery [185] and helicopter rotors [186]. In mechanical engineering, HB method is applied in nonlinear vibration analysis for many examples as well, including nonlinear multi-harmonic vibrations of bladed disks [187], vibro-impact systems [188], vibrations of buckled beams [189] or twin-well potential systems [190] just to name a few. For metastructures consist of periodic nonlinear unit cells [191] or linear unit cells with nonlinear attachments [85] [192], HB method also find its applications in successfully predicting the amplitude dependent dispersion relations.

Due to its success in analytically predicting the response of nonlinear systems, particularly for highly nonlinear systems, method of harmonic balance is selected here and is applied to solve the governing equations (11) and (12). To capture the most fundamental dynamics, the response of the bistable and linear oscillator can be modeled as

$$x(t) = c_1(t) + a_1(t)\sin(\omega t) + b_1(t)\cos(\omega t) \tag{Eq. 13}$$

$$y(t) = a_2(t)\sin(\omega t) + b_2(t)\cos(\omega t) \tag{Eq. 14}$$

with slowly varying coefficients. Substituting equations (13) and (14) and their derivatives into (11) and (12), eliminating higher order terms, and grouping the constant, $\sin(\omega t)$ and $\cos(\omega t)$ terms yield five governing equations for coefficients c_1, a_1, b_1, a_2, b_2.

$$-\gamma_1 c_1' = f\Lambda_c c_1 \tag{Eq. 15}$$

$$-\gamma_2 a_2' + 2\omega b_2' + \mu f\gamma_1 a_1' = (1-\omega^2)a_2 - \gamma_2\omega b_2 - \mu f^2\Lambda a_1 + \mu f\gamma_1\omega b_1 \tag{Eq. 16}$$

$$-2\omega a_2' - \gamma_2 b_2' + \mu f\gamma_1 b_1' = \gamma_2\omega a_2 + (1-\omega^2)b_2 - \mu f\gamma_1\omega a_1 - \mu f^2\Lambda b_1 - p \tag{Eq. 17}$$

$$\gamma_2 a_2' - (1+\mu)f\gamma_1 a_1' + 2\omega b_1' = -a_2 + \gamma_2\omega b_2 + \Sigma a_1 - (1+\mu)f\gamma_1\omega b_1 \tag{Eq. 18}$$

$$\gamma_2 b_2' - 2\omega a_1' - (1+\mu)f\gamma_1 b_1' = -\gamma_2\omega a_2 - b_2 + (1+\mu)f\gamma_1\omega a_1 + \Sigma \mathrm{b}_1 \tag{Eq. 19}$$

where the terms are defined as

$$\Lambda_c = -1 + \beta\left(c_1^2 + \frac{3}{2}r_1^2\right); \quad \Lambda = -1 + \beta\left(3c_1^2 + \frac{3}{4}r_1^2\right)$$

$$\Sigma = (1+\mu)f^2\Lambda - \omega^2; \; r_1^2 = a_1^2 + b_1^2$$

$$\Lambda_c = -1 + \beta\left(c_1^2 + \frac{3}{2}r_1^2\right); \quad \Lambda = -1 + \beta\left(3c_1^2 + \frac{3}{4}r_1^2\right)$$

$$\Sigma = (1+\mu)f^2\Lambda - \omega^2; \; r_1^2 = a_1^2 + b_1^2$$

The steady-state response of the system is determined by solving the coupled equations (15)-(19) with the condition that the time derivatives of the coefficients equal zero. From equations (16) and (17), a_2 and b_2 can be expressed in terms of a_1 and b_1. Substituting them into (18) and (19), squaring and summing resulted equations yields the characteristic equation for r_1^2

$$p^2[1+(\gamma_2\omega)^2] = \left\{\begin{matrix} [(f^2-(1+\mu)f^2\omega^2)^2 + (f^2\gamma_2\omega)^2]\Lambda^2 + [-2f^2\omega^2\{(1-\omega^2)(1-(1+\mu)\omega^2) + (\gamma_2\omega)^2\}]\Lambda + \\ \omega^2[(1-\omega^2)^2\omega^2 + (f\gamma_1)^2(1-(1+\mu)\omega^2)^2 + ((f\gamma_1\gamma_2)^2 + (\gamma_2\omega)^2 + 2\mu f\gamma_1\gamma_2\omega^2)\omega^2] \end{matrix}\right\} r_1^2 \tag{Eq. 20}$$

Equation (20) contains two unknowns c_1 and r_1^2. The constant term may be obtained by solving the steady-state response of equation (15). If the bistable device undergoes interwell oscillation, the corresponding c_1 is zero. If the response is intrawell oscillation, oscillation around one of its stable equilibria, c_1^2 is found to be

$$c_1^2 = \frac{1}{\beta} - \frac{3}{2} r_1^2 \qquad \text{(Eq. 21)}$$

Depending on the dynamics one is interested in, unique c_1 are substituted into Λ such that equation (20) is a function only of r_1^2. The roots of equation (20) can then be determined. Solutions are considered to be physically meaningful if the roots are positive, real numbers. Coefficients a_1 and b_1 are explicitly computed after obtaining r_1^2.

$$a_1 = \frac{p\omega}{\kappa}\{[(1+\mu)f^2\Lambda - \omega^2]\gamma_2\omega^2 + [1 - (1+\mu)\omega^2 + (\gamma_2\omega)^2]f\gamma_1\} \qquad \text{(Eq. 22)}$$

$$b_1 = \frac{-p}{\kappa}\{[1 - \omega^2 + (1+\mu)f^2\Lambda + (\gamma_2\omega)^2 + (1+\mu)(f\gamma_1\omega)(\gamma_2\omega)]\omega^2 - [1 + (\gamma_2\omega)^2]f^2\Lambda\} \qquad \text{(Eq. 23)}$$

where κ is defined as

$$\begin{aligned}\kappa = \{&[(f^2 - (1+\mu)f^2\omega^2)^2 + (f^2\gamma_2\omega)^2]\Lambda^2 \\ &+ [-2f^2\omega^2\{(1-\omega^2)(1-(1+\mu)\omega^2) + (\gamma_2\omega)^2\}]\Lambda \\ &+ \omega^2[(1-\omega^2)^2\omega^2 + (f\gamma_1)^2(1-(1+\mu)\omega^2)^2 \\ &+ ((f\gamma_1\gamma_2)^2 + (\gamma_2\omega)^2 + 2\mu f\gamma_1\gamma_2\omega^2)\omega^2]\}\end{aligned}$$

Coefficients a_2 and b_2 can be subsequently computed from

$$a_2 = \frac{1}{\Delta}[\Gamma_1 a_1 + \Gamma_2 b_1 + (\gamma_2\omega)p] \qquad \text{(Eq. 24)}$$

$$b_2 = \frac{1}{\Delta}[-\Gamma_2 a_1 + \Gamma_1 b_1 + (1-\omega^2)p] \qquad \text{(Eq. 25)}$$

where the terms are defined as

$$\begin{aligned}\Delta &= (1-\omega^2)^2 + (\gamma_2\omega)^2 \\ \Gamma_1 &= (1-\omega^2)(\mu f^2\Lambda) + (\gamma_2\omega)(\mu f\gamma_1\omega) \\ \Gamma_2 &= (\gamma_2\omega)(\mu f^2\Lambda) - (1-\omega^2)(\mu f\gamma_1\omega)\end{aligned}$$

Having computed all five coefficients, stability of the physically meaningful solution can be determined via perturbation analysis [12].

To take phase relationships into consideration, steady state responses of equations (13) and (14) can be alternatively expressed as

$$x = c_1 + r_1 cos(\omega t - \varphi_1) \qquad \text{(Eq. 26)}$$

$$y(t) = r_2 \cos(\omega t - \varphi_2) \qquad \text{(Eq. 27)}$$

additionally defining

$$r_2^2 = a_2^2 + b_2^2 \qquad \text{(Eq. 28)}$$

$$\tan(\varphi_1) = a_1/b_1\,; \tan(\varphi_2) = a_2/b_2 \qquad \text{(Eq. 29)}$$

The relative vibration amplitudes and phase lags between bistable and linear oscillator (r_1, φ_1) and between linear oscillator and base (r_2, φ_2) are evaluated by substituting equations (22) to (24) into equations (28) and (29).

4.2.3 Stability analysis

To determine the stability of physically meaningful solutions, equations (15) through (19) are cast into the form $\boldsymbol{A}\boldsymbol{x}' = \boldsymbol{F}(\boldsymbol{x})$ where vector $\boldsymbol{x}$ is defined by $\boldsymbol{x} = [a_1, b_1, c_1, a_2, b_2]^T$. Stability of response solutions may then be determined by assessing the eigenvalues of the Jacobian of $\boldsymbol{G} = \boldsymbol{A}^{-1}\boldsymbol{F}(\boldsymbol{x})|_{x=x_{ss}}$ [28].

4.3 Analytical investigation of coupling influences

4.3.1 Effect of bistable oscillator mass ratio

In this section, we investigate the influence of mass ratio μ on bistable oscillator response. The responses were determined using the system characteristics $p = 0.2, f = 0.25, \beta = 1, \gamma_2 = 0.001$, and mass ratio $\mu = [0.1,0.5,1]$. For comparison to the benchmark of the single bistable oscillator, we compute the single bistable device response from its governing equation nondimensionalized using the time of the coupled system $t = \omega_2 \tau$.

Figure 22 shows the response amplitude and phase between the bistable oscillator and linear oscillator, as well as the response amplitude and phase between the linear oscillator and base. The response of the bistable device on its own (without the linear oscillator) relative to base is also provided as a baseline for comparison. Figure 22(a) shows that the coupled system increases the response of the bistable oscillator above the baseline of the single bistable device for cases with large mass ratio μ, in a relatively broad frequency range below $\omega = 1$. Even for small mass ratio, there still exists a frequency bandwidth close to $\omega = 1$ where the coupled bistable oscillator outperforms the uncoupled device. One of the reasons for such an increase is due to the large vibration amplitude of the linear oscillator, depicted in Figure 22(d), which amplifies the input a bistable device experiences from base excitation. As the mass ratio μ increases from 0.1 to 1, the amplification of the bistable response for the coupled system becomes more substantial with the tradeoff that high-energy dynamics destabilize at lower frequencies. The reason for this result is indicated by the phase relationship. Figure 22(b) shows that as driving frequency nears the point at which high-energy dynamics are destabilized, the bistable and linear oscillators approach a 90° phase lag. Thus the system approaches an in-phase resonance, similar to the lowest mode of a classical linear 2DOF system. Likewise, as shown in Figure 22(a), the relative amplitude of the bistable device for stable in-phase response remains greater than 1 (greater than the amplitude between the two stable equilibria, determined to be $1/\sqrt{\beta}$ using the definitions from Sec.4.2), indicating a snap-through action as opposed to simply moving in-phase with the same response magnitude of the linear resonator. As the excitation frequency approaches this resonance feature, we find in Figure 22(b) that the coupled bistable and the linear oscillators exhibit greater and greater phase difference. With large relative displacements, Figure 22(a), the bistable oscillator requires large excitation levels in order to sustain such a snap through response. We find that the current excitation level becomes insufficient for this purpose and therefore stability of high-energy dynamics are lost.

As the excitation frequency approaches the linear oscillator natural frequency ($\omega = 1$), another branch of stable out-of-phase high-energy dynamics is predicted. Increasing mass ratio μ reduces the out-of-phase snap through response but broadens the stable frequency range. In contrast to the prior destabilization of in-phase system dynamics, the 180° phase difference between the oscillators is accompanied by a much smaller difference in relative displacement, as depicted in Figure 22(a). Thus, even though the two oscillators are out-of-phase with each other, the snap through dynamic remains stable. We observe that in some cases, the bistable oscillator amplitude is less than the amplitude between the stable and unstable equilibria $r_1 < 1$, for example Figure 22(a) lower amplitude stable branches around $\omega = 0.8$. Since the bistable oscillator exhibits such small snap through vibrations, this represents a stabilization of the unstable equilibrium position. Excitation-induced stability is also observed in other nonlinear systems, for example the parametrically excited inverted pendulum [14].

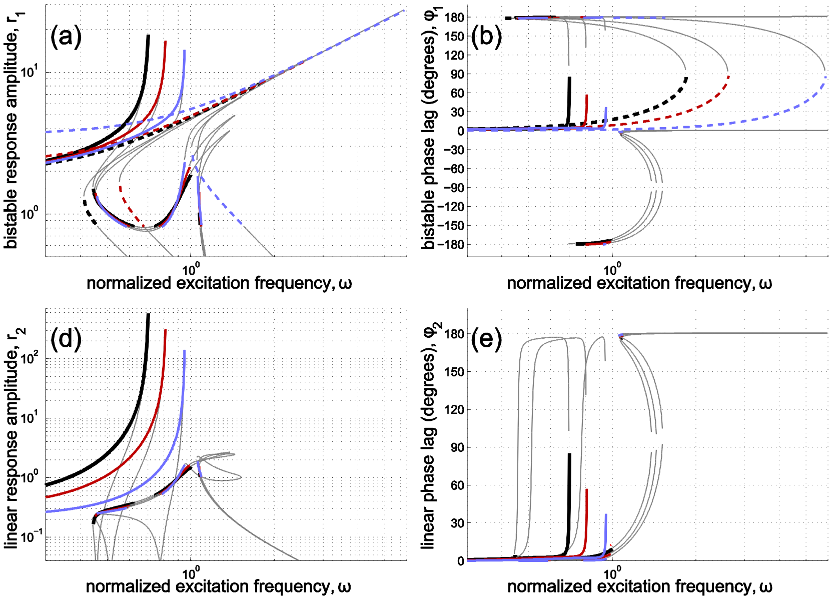

Figure 22. High-energy dynamics as mass ratio μ varies from (blue) 0.1, (red) 0.5, (black) 1. Solid curves correspond to response of the coupled linear-bistable system; dashed curves to the response of the single bistable device. Thin grey lines are unstable solutions. Top row: relative dynamics between bistable and linear oscillator (a) displacement amplitude (r_1); (b) phase lag (φ_1); Bottom row: relative dynamics between linear oscillator and base (d) displacement amplitude (r_2); (e) phase lag (φ_2).

4.3.2 Effect of bistable oscillator tuning ratio

To explore the influence of tuning ratio f, we retain parameters of the prior investigations but now consider $\mu = 0.3$ and $f = [0.1, 0.2, 1]$. Figure 23 presents the high-energy dynamics of the bistable oscillator with the responses of the corresponding single bistable device for comparison.

Figures 23(a) and (b) show that two distinct regions of stable high-energy dynamics can be identified: amplified bistable oscillator dynamics in a certain frequency region with ω less than $\omega = 1$ and out-of-phase response around $\omega = 1$. Regardless of the tuning ratio, the amplification effect induced by coupling is always observed to be most prominent from frequencies of approximately $0.6 < \omega < 0.8$ with system response destabilized at the same frequency. This suggests that the frequency at which the high-energy dynamics of the coupled system are destabilized is controlled by the mass ratio while the frequency ratio plays the role of determining the rate at which the response asymptotically grows prior to destabilization.

The tuning ratio is also an important parameter controlling the existence of out-of-phase dynamics around $\omega = 1$. As shown in Figure 23(a), the relative response amplitude between the bistable and linear oscillators of the out-of-phase dynamic decreases as tuning ratio f increases to the point that stable response is eventually not possible should tuning ratio become too great. For example, Figure 23(c) predicts that power generated by the out-of-phase dynamic near $\omega = 1$ is greatest for a tuning ratio of $f = 0.1$, less substantial for $f = 0.2$, but is not possible for $f = 1$ since the dynamic is no longer stable.

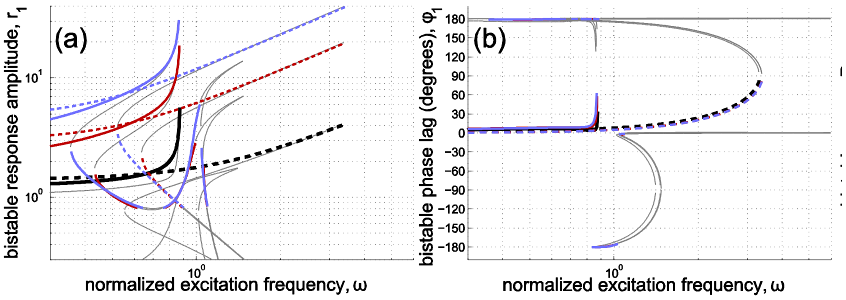

Figure 23. High-energy dynamics as tuning ratio f varies from (blue) 0.1, (red) 0.2, (black) 1. Solid curves correspond to response of coupled linear-bistable system; dashed curves to the response of the single bistable device. Thin grey lines are unstable solutions. Relative dynamics between bistable and linear oscillators (a) displacement amplitude (r_1); (b) phase lag (φ_1).

4.4 Interpretation of the induced frequency response

The coupled linear-bistable metastable module yields a frequency characteristic unique for a nonlinear 2DOF system. However, like a linear 2DOF system, two resonance phenomena are still observed when the second oscillator has a bistability: the in- and out-of-phase snap through features apparent in Figures 22(a) and 23(a) and. Section 4.3.1 gives evidence that the mass ratio μ plays a role in determining the frequency at which the first resonance feature appears and the second resonance seemed to be fixed, starting from the same frequency as the uncoupled linear system. Here, we confirm this intuition, develop guidelines for designing the frequency response characteristics of the linear-bistable metastable module, and also provide a new interpretation of the snap through phenomena.

Bistable snap through may be characterized as a non-resonant phenomenon because any form or frequency of excitation may induce a switching of the mass from one stable state to the other. From the perspective of the linear oscillator of natural frequency ω_2 as presented in Sec. 4.2, a non-resonant attachment of finite mass may be realized in one of two forms: when the attachment natural frequency approaches zero $(f \rightarrow 0/\omega_2)$ or when the attachment natural frequency is infinity $(f \rightarrow \infty/\omega_2)$. For the prior case, the attachment has an infinitesimally small natural frequency while in the latter case the attachment is infinitely stiff such that it appears as "dead weight" to the linear structure. Therefore, we may interpret the manner in which a bistable device interacts with a linear oscillator during snap through as being identical to a linear attachment of $f \rightarrow 0$ or $f \rightarrow \infty$ interacting with the primary linear structure.

These perspectives are supported by considering the limiting cases of the undamped linear 2DOF system [16]. The characteristic equation governing the split resonances of a linear oscillator with attached secondary linear oscillator is

$$\omega^4 - \left(1 + f^2(1+\mu)\right)\omega^2 + f^2 = 0 \qquad \text{(Eq. 30)}$$

where f is defined as the frequency ratio between the attached and host linear oscillators. Using equation $\omega 4 - \left(1 + f^2(1+\mu)\right)\omega^2 + f^2 = 0$ (Eq. 30), a comparable linear attachment of $f \to 0$ splits the original linear system resonance into normalized frequencies $\omega^* = 0$ and 1. Thus, interpreted as a linear oscillator attachment of zero natural frequency, the out-of-phase snap through response does not shift this particular response from the uncoupled resonance of the primary linear system, as has been indicated in Figure 22(a,d). Likewise, for the limiting case $f \to \infty$, only terms multiplied by f^2 in equation $\omega 4 - \left(1 + f^2(1+\mu)\right)\omega^2 + f^2 = 0$ (Eq. 30) are appreciable. There are no longer split resonances but one resonance associated with the composite mass: $\omega^* = 1/\sqrt{1+\mu}$ where μ is defined as the mass ratio between attachment and host oscillators. Therefore, in-phase snap through induces a resonance phenomenon associated with the composite mass of the system. Taken together, these two dynamic phenomena indicate the location in frequency at which a bistable attachment "splits" the uncoupled resonance of the linear structure, yielding one resonance feature at the uncoupled linear natural frequency $\omega^* = 1$ associated with out-of-phase snap through and a second due to the mass of the bistable attachment $\omega^* = 1/\sqrt{1+\mu}$ associated with in-phase snap through.

We validate this perspective by computing the system dynamics in the absence of damping with $p = 0.01$, $f = 0.25$, $\beta = 1$. Figure 24 shows the linear structure response with bistable attachments over a range of mass ratios μ. The frequencies at which the lower resonance characteristics occur are identical to those determined from the expression $\omega^* = 1/\sqrt{1+\mu}$, also confirming the observation in Sec. 4.3.1 that μ determines where this resonance feature appears.

This shows conclusively that for the coupled linear-bistable metastable module, snap through phenomena may be tailored for enhanced vibration compared to a single bistable oscillator by adjustment of the mass ratio μ for locating the in-phase high-energy dynamics. In a manner of speaking, the bistable attachment does induce frequency splitting to the primary linear system if we interpret bistable snap through as two simultaneous linear phenomena, $f \to 0$ and $f \to \infty$. Thus, the snap through phenomenon may be interpreted as both a resonance at zero natural frequency and a resonance at infinite natural frequency.

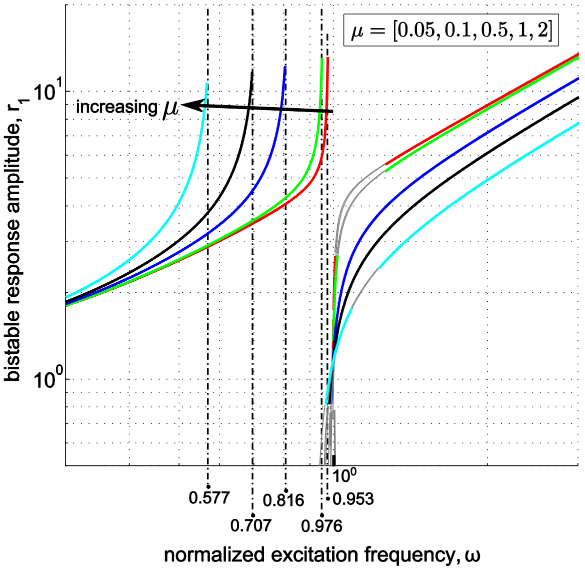

Figure 24. High-energy dynamics of undamped bistable oscillator for coupled system as mass ratio μ changes. Bold curves correspond to stable response and thin grey lines are unstable solutions. Dashed lines are predicted first resonant frequency.

4.5 Experimental validation

The results of Sec. 4.3 indicated that coupling of a linear oscillator to a bistable oscillator could (i) amplify low excitation levels to intensify snap through and also (ii) yield an out-of-phase snap through response around the linear oscillator uncoupled natural frequency. These two results enhance the vibration of the bistable system esting and were shown to be tailored for fixed excitation level by adjusting tuning ratio f and mass ratio μ. The tuning ratio was shown to be important in terms of generating the out-of-phase snap through dynamic unique to the coupled system. Here, we validate these key analytical trends by experiments which focus on the ability of an appropriately tuned, by f, linear-bistable metastable system to achieve the dynamic phenomena (i) and (ii) above.

A photograph of the test setup is shown in Figure 25. The linear oscillator mass is composed of the machined aluminum frame, bottom bearing mass, and bistable oscillator bearing guide rail. The bistable mass is composed of the bearing mass in the middle of the photograph along with the hardware necessary to affix the mass to a spring pre-compressed in its upright position. The bistable oscillator is developed by pre-compressing the spring (in its upright position) between the bistable inertial mass and a rotational pivot affixed to the linear oscillator. Therefore, the two stable equilibria for the bistable mass are to the right and left of the central unstable position. Guide rods are used to prevent the pre-compressed spring from bending or twisting as the inertial mass snaps from one stable state to the other. Both linear and bistable oscillators utilize low-friction linear slide bearings. The coupled system is mounted to an electrodynamic shaker table activated in the horizontal left-right direction. A number of spring connections are available to connect the linear oscillator mass to the shaker platform and consequently for tailoring the tuning ratio f of the system; we employ two resulting tuning ratios are such that $f_2 < f_1 < 1$ which are in a range that analyses predicted most favorable for inducing phenomena (i) and (ii) described above. A slowly swept sinusoid (+0.0092 Hz/second) is the input to the shaker such that response of the system is evaluated from 2 to 10 Hz. To compare the dynamics of a single bistable oscillator to the same input conditions, the linear oscillator is locked to the shaker platform by replacing the lower spring connection with a solid bar linkage. The displacement of the shaker platform is measured by a potentiometer while two accelerometers measure the dynamics of the linear and bistable oscillators.

Figure 26 plots the measured acceleration frequency response functions (frf). For the single bistable oscillator, this is computed as the ratio of accelerations of the bistable inertial mass to the shaker input acceleration; for the coupled system, this is the ratio of the relative acceleration between the bistable and linear elements to the shaker acceleration. The sweep test is conducted for three excitation levels which represent typical ambient structural vibration magnitudes [17]. Input acceleration of 0.98 m/s^2 is incapable of inducing in-phase snap through for either the individual device or for the system having tuning ratio f_1. However, at 2.75 Hz, the coupled system of f_2 exhibits in-phase snap through dynamics, increasing the frf by 94% over the level of the single bistable device. Figure 26 shows that increasing the input acceleration to 1.18 and 1.38 m/s^2 enables all of the bistable inertial masses to snap through in-phase with the linear oscillator. It also shows that the bistable frf magnitudes of the coupled systems are greater than the single bistable frf for the in-phase snap through dynamic but destabilize the high-energy dynamics at a frequency slightly less than the single bistable device can maintain. Figure 27(a) shows a photographic timeseries capture of one excitation period at 3 Hz for the coupled system using tuning ratio f_2. The red lines serve as fixed positioning references throughout the frames. It is evident that both oscillators exhibit substantial in-phase vibration. This confirms trends predicted by the analyses of Sec. 4.3.

While the single bistable system exhibits only low-energy dynamics for excitation frequencies greater than the maximum sustainable interwell oscillation frequency (3 to 4 Hz), the coupled systems undergo another energetic out-of-phase high-energy dynamics at higher frequencies. This can be verified by the timeseries captures in Figure 27(b) in which at the beginning of the period the linear oscillator is to the left while the bistable oscillator displaces to the right, and vice versa halfway through the excitation period. Contrary to the previous in-phase snap through where high-energy dynamics may be difficult to achieve based on excitation level, out-of-phase snap through can be induced for low levels of excitation like 0.98 m/s2. The out-of-phase resonance feature is achieved around 8 Hz for system with f_1 and 5.5 Hz for system with f_2. The system with f_2 undergoes greater amplitude out-of-phase snap through than the system with f_1 since $f_2 < f_1$, also verifying the trend predicted in Section 4.3.2. For maximum effectiveness and robustness, both in- and out-of-phase interwell dynamics should be exploited. Lastly, Figure 26 shows that the frf of the out-of-phase high-energy dynamics of the bistable attachment are on the same order as the in-phase snap through indicating that the experimental setup is actually moderately damped.

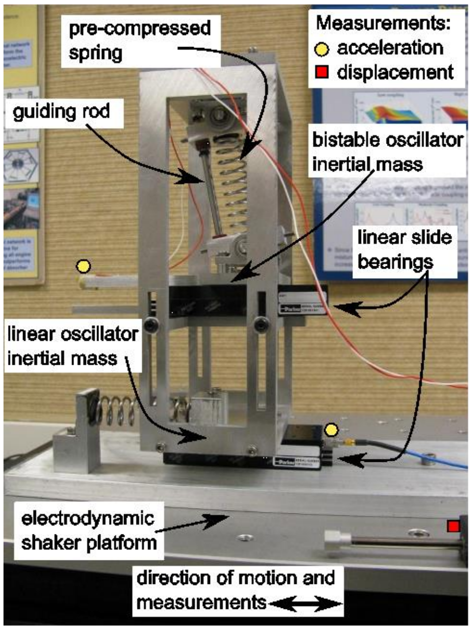

Figure 25. Photograph of linear-bistable coupled metastable system showing elements of configuration and test setup.

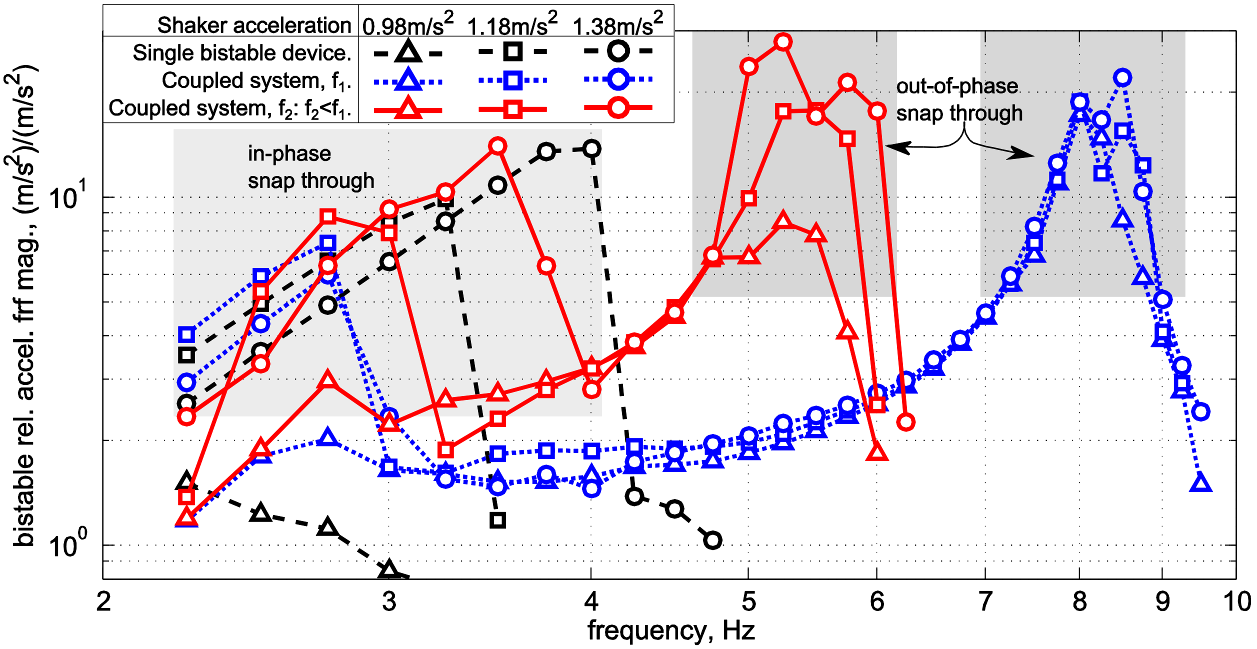

Figure 26. Acceleration frf of the bistable oscillator mass as a function of shaker input frequency for three input acceleration levels. Data presented for the single bistable system and two cases of coupling tuning ratio.

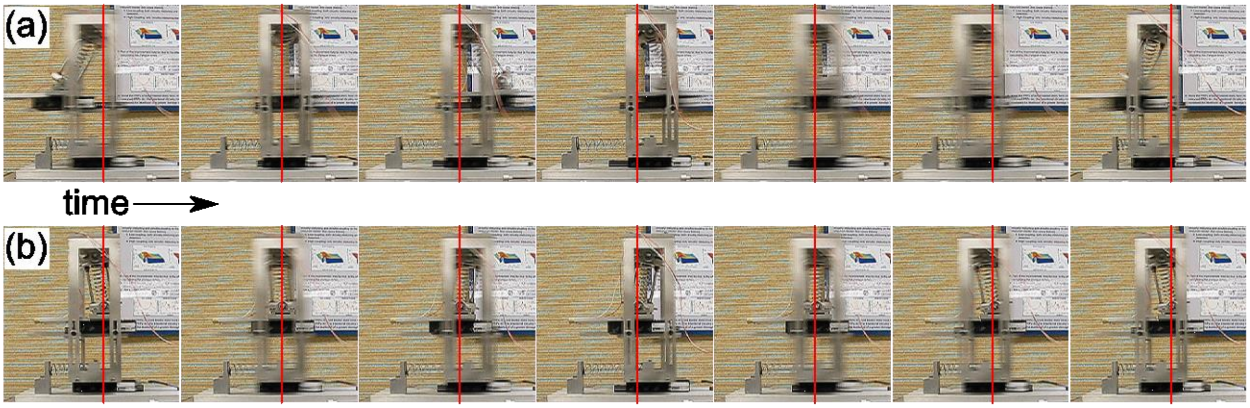

Figure 27. Frame by frame photographs of one excitation period for coupled system having f_2: a) in-phase response at 3 Hz; b) out-of-phase response at 5 Hz. Vertical red lines are identically positioned throughout the timeseries to serve as position references.

Chapter 5

Dynamics of Metastructures for On-Demand Reconfiguration of Band Structures and Non-Reciprocal Wave Propagation

5.1 Chapter overview

With previous understandings on dynamical response of the unit metastable modules, in this chapter, we present a novel approach to achieve adaptable band structures and non-reciprocal wave propagation by exploring and exploiting the metastable modular metastructures. Through studying the dynamics of wave propagation in a chain composed of finite metastable modules, we provide experimental and analysis results on non-reciprocal wave propagation and unveil the underlying mechanisms that facilitate such unidirectional energy transmission. In addition, we demonstrate that via transitioning amongst the numerous metastable states, the proposed metastructure is endowed with a large number of bandgap reconfiguration possibilities. As a result, we illustrate that unprecedented adaptable non-reciprocal wave propagation can be realized using the metastable modular metastructure. Overall, this research elucidates the rich dynamics attainable through the combinations of periodicity, nonlinearity, spatial asymmetry, and metastability, and creates a new class of adaptive structural and material systems capable of realizing tunable bandgaps and non-reciprocal wave transmissions.

5.2 Overall concept and example metastructure

The building block of the metastructure considered in this study is a metastable module consisting of a bistable spring and linear spring integrated in series [193] [194]. With such arrangement, the proposed module will exhibit metastability that is essential to realize the broadband non-reciprocal wave propagation and adaptation. A lab test stand is set up to explore the concept. The bistable constituent is generated by press fitting three magnets with repulsive polarization inside a 3D printed enclosure connected in parallel with a stabilizing spring realized via spring steel. Characteristic force-displacement profile of a bistable element is measured with an Instron machine, shown in Figure 28(a). The bistable element is then connected in series with a linear spring steel to form a metastable module. A characteristic force-displacement profile of the module is depicted in Figure 28 (b). As shown in Figure 28 (b), the building block exhibits a metastable range, where two metastable states (internal configurations) coexist with the same overall topology (global displacement). The experimental setup of the metastructure consists of a chain of such metastable modules connected in series horizontally, aligned with guiding rail and linear sliding bearings. Figure 28(c) depicts the top view of the experimental test bed and Figure 28 (d) shows the corresponding schematic of the metastructure in which the bistable constituents are represented with buckled beams, the linear constituents are represented with coil springs and the inertial elements are symbolized with orange and yellow circles. As denoted in Figure 28 (d), free length of the structure L_{free} is defined to be the zero force position when all the bistable elements are buckled to the left and the global displacement z is defined as the additional deformation applied to the structure starting from the free length L_{free} position. In this research, we focus on steady state wave propagation through the metastructure as the chain is harmonically driven from one end. To investigate the non-reciprocal effect, two actuation scenarios are considered: one is forward actuation with actuator on the left side of the lattice chain and the other is backward actuation with actuator on the right-hand side of the chain. The conceptual representation of the excitation scenarios is depicted in Figure 28 (e). For illustration purposes, only inertial elements denoted by orange and yellow circles are presented in Figure 28 (e) while the stiffness constituents connecting the masses are not shown. For both scenarios, harmonic displacement input x_{in} is directly applied to the mass next to the boundary of the chain indicated by square, and output signal x_{out} is measured one module away from the boundary marked with circle, Figure 28 (c) and (e). During the experiments, both input and output displacements are measured with laser vibrometers.

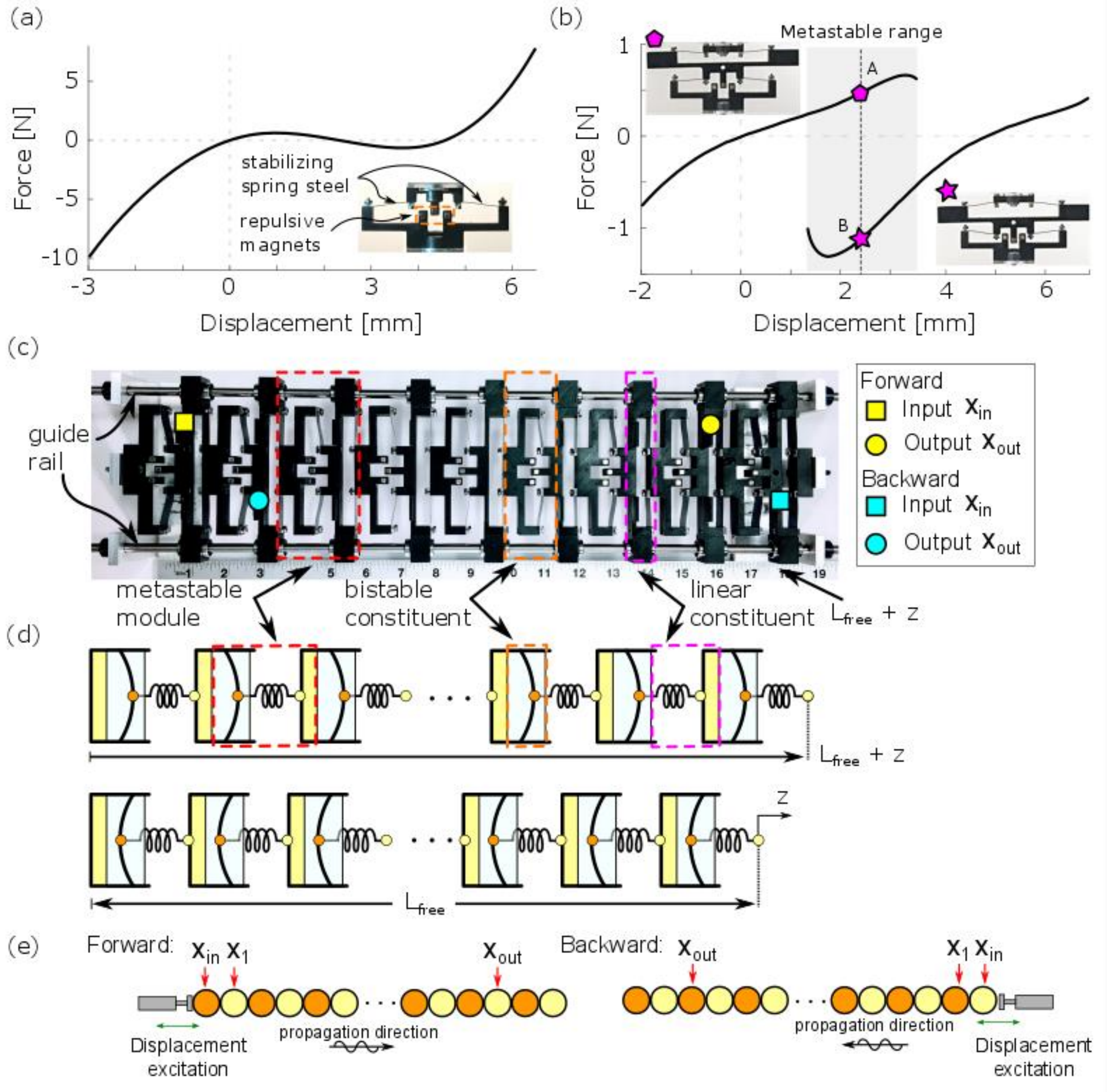

Figure 28. (a) Characteristic force displacement profile of a bistable element. (b) Characteristic force displacement profile of a metastable module. (c) and (d) Top view and corresponding schematic of the experiment setup. (e) Conceptual diagrams of metastable module assembled in series under forward (excitation from left) and backward (excitation from right) actuations.

5.3 Mathematical model and band structure analysis

5.3.1 Metastable states

Figure 29 depicts a 1D discrete lattice representation of N identical metastable modules connected in series Each metastable module, highlighted with red dashed box, consists of two masses m_1 and m_2 coupled via a linear constituent; the modules are inter-connected by bistable springs. Without loss of generality, the bistable and linear restoring forces are assumed of the form, $F_{NL} = -k_1 x + k_3 x^3$ and $F_L = k_L y$, where x and y are the deformations of bistable and linear springs respectively. The total potential energy of the metastable chain for a fixed global displacement z measured from its free length L_{free} can be expressed as:

$$U = \sum_{i=1}^{N-1}\left[\frac{k_L}{2}\left(x_{[i]2} - x_{[i]1}\right)^2 - \frac{k_1}{2}\left(x_{[i+1]1} - x_{[i]2}\right)^2 + \frac{k_3}{4}\left(x_{[i+1]1} - x_{[i]2}\right)^4\right] + \frac{k_L}{2}\left(z - x_{[N]1}\right)^2 - \frac{k_1}{2}x_{[1]1}^2 + \frac{k_3}{4}x_{[1]1}^4 \qquad \text{(Eq. 31)}$$

which is a function of internal mass displacements $x_{[i]1}$, $x_{[i]2}$, where subscript i refers to the i^{th} module. All internal displacements $x_{[i]1}$and $x_{[i]2}$ are measured from the individual positions of the free length configuration. For a fixed global displacement z, equilibrium positions of metastructure satisfy $\partial U/\partial x_{[i]1} = 0$ and $\partial U/\partial x_{[i]2} = 0$ under the constraint that $\sum_{i=1}^{N-1}\left(x_{[i]1} + x_{[i]2}\right) + x_{[N]1} = z$. According to the minimum potential energy principle [193] [194], metastable states of the chain satisfy $\partial^2 U/\partial x_{[i]k}\partial x_{[j]l} > 0$, i.e. the Hessian matrix of the potential is positive definite.

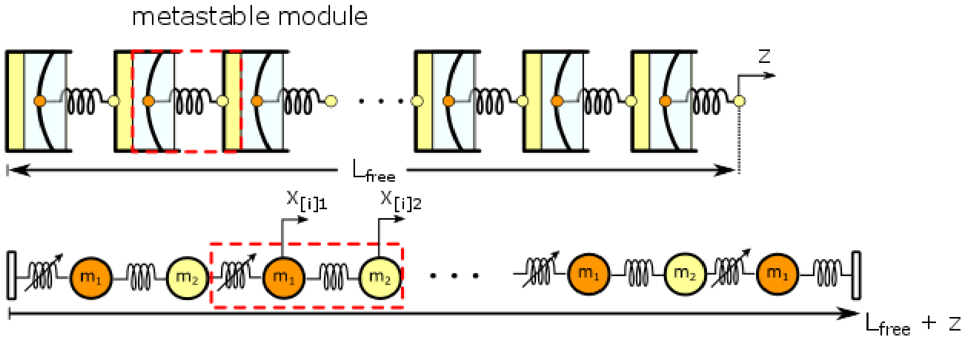

Figure 29. Schematic and discrete mass spring representation of an N metastable module assembled in series. A periodic unit cell, in this case same as the metastable module, is highlighted with red dashed box.

5.3.2 Governing equations and linear dispersion analysis

In general, for a fixed global displacement z, a chain of N metastable modules can have up to 2^N metastable states (internal configurations) with varying system properties [193] [194]. Starting from one of the metastable states, equations of motion for the i^{th} module, can be expressed as:

$$m_1\ddot{x}_{[i]1} + F_{NL}\big(x_{[i]1} - x_{[i-1]2}\big) + k_L\big(x_{[i]1} - x_{[i]2}\big) = 0 \qquad \text{(Eq. 32a)}$$

$$m_2\ddot{x}_{[i]2} + F_{NL}\big(x_{[i]2} - x_{[i+1]1}\big) + k_L\big(x_{[i]2} - x_{[i]1}\big) = 0 \qquad \text{(Eq. 32b)}$$

Eq. (32a) is applicable to $\forall i = 2$ to N and Eq. (32b) is applicable to $\forall i = 1$ to N-1. Due to the fixed boundary conditions, equations of motion for first and last mass in the chain can be modified as

$$m_1\ddot{x}_{[1]1} + F_{NL}\big(x_{[1]1}\big) + k_L\big(x_{[1]1} - x_{[1]2}\big) = 0 \qquad \text{(Eq. 33a)}$$

$$m_1\ddot{x}_{[N]1} + F_{NL}\big(x_{[N]1} - x_{[N-1]2}\big) + k_L\big(x_{[N]1} - z\big) = 0 \qquad \text{(Eq. 33b)}$$

Depending on the excitation scenarios, Figure 28 (c), external excitation will be directly applied to the first or last mass in the chain.

To establish a linear dispersion relation, we first linearize the equations of motion about its metastable state and the band structure is determined by modeling a repeating periodic unit cell of an unforced, infinite chain. For the diatomic chain depicted in Figure 29, the periodic unit cell is the same as a metastable module, and the linearized equation can be written as:

$$m_1\ddot{\zeta}_i + \tilde{k}_{NL}(\zeta_i - \eta_{i-1}) + k_L(\zeta_i - \eta_i) = 0 \qquad \text{(Eq. 34a)}$$

$$m_2\ddot{\eta}_i + \tilde{k}_{NL}(\eta_i - \zeta_{i+1}) + k_L(\eta_i - \zeta_i) = 0 \qquad \text{(Eq. 34b)}$$

where ζ_i and η_i are small perturbation of mass m_1 and m_2 around its initial positions and $\tilde{k}_{NL}$ is the corresponding linearized stiffness of the bistable spring. Assuming solutions in the form of a traveling wave, i.e, $\zeta_i = Aexp[j(\omega t - kiL)]$ and $\eta_i = Bexp[j(\omega t - k(i+1)L)]$, where k is the wave number and L is unit length, the model is reduced to a standard eigenvalue problem:

$$\begin{bmatrix} (k_L + \tilde{k}_{NL})/m_1 & -(\tilde{k}_{NL} + k_L e^{-jkL})/m_1 \\ -(\tilde{k}_{NL} + k_L e^{jkL})/m_2 & (k_L + \tilde{k}_{NL})/m_2 \end{bmatrix} \begin{bmatrix} A \\ B \end{bmatrix} = \omega^2 \begin{bmatrix} A \\ B \end{bmatrix} \tag{Eq. 35}$$

The band structure can then be determined by sweeping the wave number k from 0/L to π/L. In general, due to the existence of multiple metastable states for a chain of N metastable modules, depending on the initial configuration, periodic repeating cell should be identified and similar dispersion analysis can be carried out accordingly.

5.3.3 Analysis results of band structures

For exploration purposes and without loss of generality, parameters used in the analysis are chosen to be of arbitrary unit. With stiffness $k_1 = 1, k_3 = 1, k_L = 0.2$ and masses $m_1 = m_2 = 1$, Figure 3(a) depicts the resultant force profile of the metastructure as global displacement changes. Due to a synergistic product of assembling together metastable modules, multiplying number of different internal configurations can be afforded via transitioning amongst these metastable states for the same global displacement z [193] [194]. Since each metastable state exhibits unique system property [193] [194], the ability to reconfigure amongst these states exemplifies the broad adaptation space of the proposed metastructure for wave propagation. For instance, configurations A and B in (a) represent two possible periodic chains of the same global length with different internal configurations or metastable states. Periodic unit cells for the two configurations are highlighted with red dashed box in Figure 30(a) and the corresponding band structures for configurations A and B are depicted in Figure 30 (b) and (c) respectively. For both configurations A and B, the periodic cells consist of a single metastable module with different internal configurations, Figure 30 (a). As illustrated in Figure 30, property programmability can be realized via metastable state switching, demonstrated by the adaptation of band structures of the metastable chain. For configuration A, the two passbands are [0, 0.633] and [2, 2.098] whereas for configuration B, the first passband remains to be the same [0, 0.633] while the second passband shifts to [1.069, 1.242].

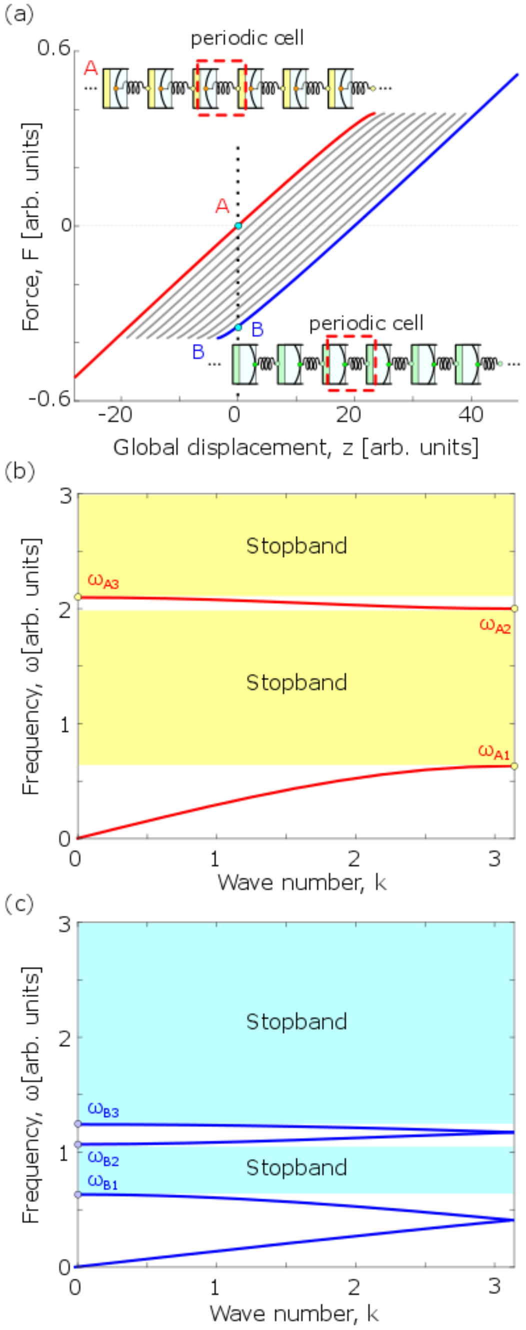

Figure 30. (a) Reaction force profile as a function global displacement for a 10 module metastable chain. Points A, B are two different configurations for the same global topology realized by internal configuration switching. (b) and (c) Corresponding band structures for configurations A and B. Passband are within $[0,\ \omega_{A1}]$, $[\omega_{A2},\ \omega_{A3}]$ and $[0,\ \omega_{B1}]$, $[\omega_{B2},\ \omega_{B3}]$ respectively, demonstrating the massive band structures tunability via internal configuration switching.

5.4 Non-reciprocal wave propagation and adaptation

5.4.1 Experimental investigation

With the same global confinement of 45.1 cm (17.75 inches), two configurations I and II of the experiment setup are depicted in Figure 31(a). The two configurations are obtained by switching between metastable states and the periodic repeating cells are highlighted with dashed boxes. To first identify the band structures, frequency sweep tests are performed for both configurations with input RMS acceleration 0.3 m/s^2 via an electromagnetic shaker. Due to limitation of the shaker, the frequency range is selected to be from 5Hz to 50Hz and the sweep rate is chosen to be 0.05 Hz/s. Figure 31 (b) depicts the displacement frequency response function (FRF) in forward actuation direction, with blue and red representing configurations I and II respectively. As depicted in Figure 31 (b), the first passband for configuration I extends to approximately 10Hz and for configuration II, the first passband ends at around 18.5Hz. Therefore, for excitation frequency in between 10Hz and 18.5Hz, wave propagation characteristics can be adaptively tuned between propagating and non-propagating as the proposed structure reconfigures between metastable states I and II. Furthermore, such adaptation can be exploited in-situ, depicted by the displacement time history in Figure 31 (c). With input RMS displacement 0.2mm and input frequency 15Hz (gray), the system starts in configuration II and at steady state the vibration energy is able to propagate through the chain since the excitation frequency is inside the passband (blue). We then switch to configuration I manually by sequentially reconfiguring two bistable constituents while the metastructure is still harmonically excited, depicted by the consecutive spikes in time history (black) in Figure 31 (c). After switching in-situ to configuration I, the excitation frequency changes from inside the passband to stopband, and as a result, the output displacement is reduced significantly to nearly zero (red). Therefore, due to band structure adaptation, we are able to in-situ create immediate change of wave propagation characteristics as system reconfigures.

To illustrate the non-reciprocal wave propagation phenomenon, metastructure is prescribed in configuration I and is excited at 15Hz. The excitation frequency is chosen such that it is inside the stopband of the linearized structure. With the same starting configuration, system is excited in forward and backward actuation scenarios individually with a fixed input amplitude and the corresponding output and input displacements are measured using laser vibrometers. Same experimental procedures are then repeated for different input excitation amplitudes. Figure 31 (d) summarize the results of transmittance ratio for different input amplitudes and the discrete points circle (triangle) for forward (backward) excitation scenarios are connected with solid (dashed) lines to illustrate the trend. The transmittance ratio (TR) is defined as the ratio of steady state output RMS displacement over input RMS displacement $TR = |\bar{x}_{out}|/|\bar{x}_{in}|$. As indicated in Figure 31 (d), with small excitation level, due to the bandgap effect, the output displacement is negligible compared to the input amplitude for both excitation directions. As input amplitude increases to 0.3mm, transmittance ratio of the backward actuation increases significantly while it remains to be low for forward actuation, depicted in Figure 31 (d), providing experimental evidence on the start of non-reciprocal wave propagation. This unidirectional energy transmission phenomenon ends at input amplitude 0.58mm, at which sudden increase in the output amplitude for the forward actuation is also made possible. Such amplitude dependent wave transmission feature corroborates with studies on supratransmission, in which energy of a signal with input frequency in the stopband is able to transmit through a nonlinear chain when input amplitude exceeds certain threshold [88] [94] [101] [105] [195] [196]. For the proposed architecture, integrating the supratransmission property of a nonlinear periodic chain with spatial asymmetry, the metastable structure is capable of attaining the onset of supratransmission at different input amplitude levels depending on actuation direction, and this threshold discrepancy creates a region that facilitates the non-reciprocal wave propagation.

In addition to non-reciprocal wave propagation, endowed with metastability, the proposed structure is also capable of exhibiting onset of supratransmission at different excitation level by internal reconfiguration. As illustrated in Figure 31 (e), the metastructure is excited under forward actuation at 20Hz for both configurations I and II. Similar to previous studies, structures are excited with fixed input amplitude for each configuration and these individual tests are connected with lines to illustrate the trend on wave propagation characteristics as input amplitude increases. Since under small excitation level, the metastructure resembles that of a linear system and energy does not transmit through the chain given that the input frequency is within the stopband for both configurations. As input amplitude increases to 0.06mm, energy starts to transmit through the chain for configuration II whereas wave propagation is still prohibited for configuration I until excitation level reaches 0.45mm, after which wave propagates through the chain for both configurations. Such adaptivity on the onset of supratransmission for different configurations is crucial to create systems with on-demand tuning of non-reciprocal wave propagation characteristics.

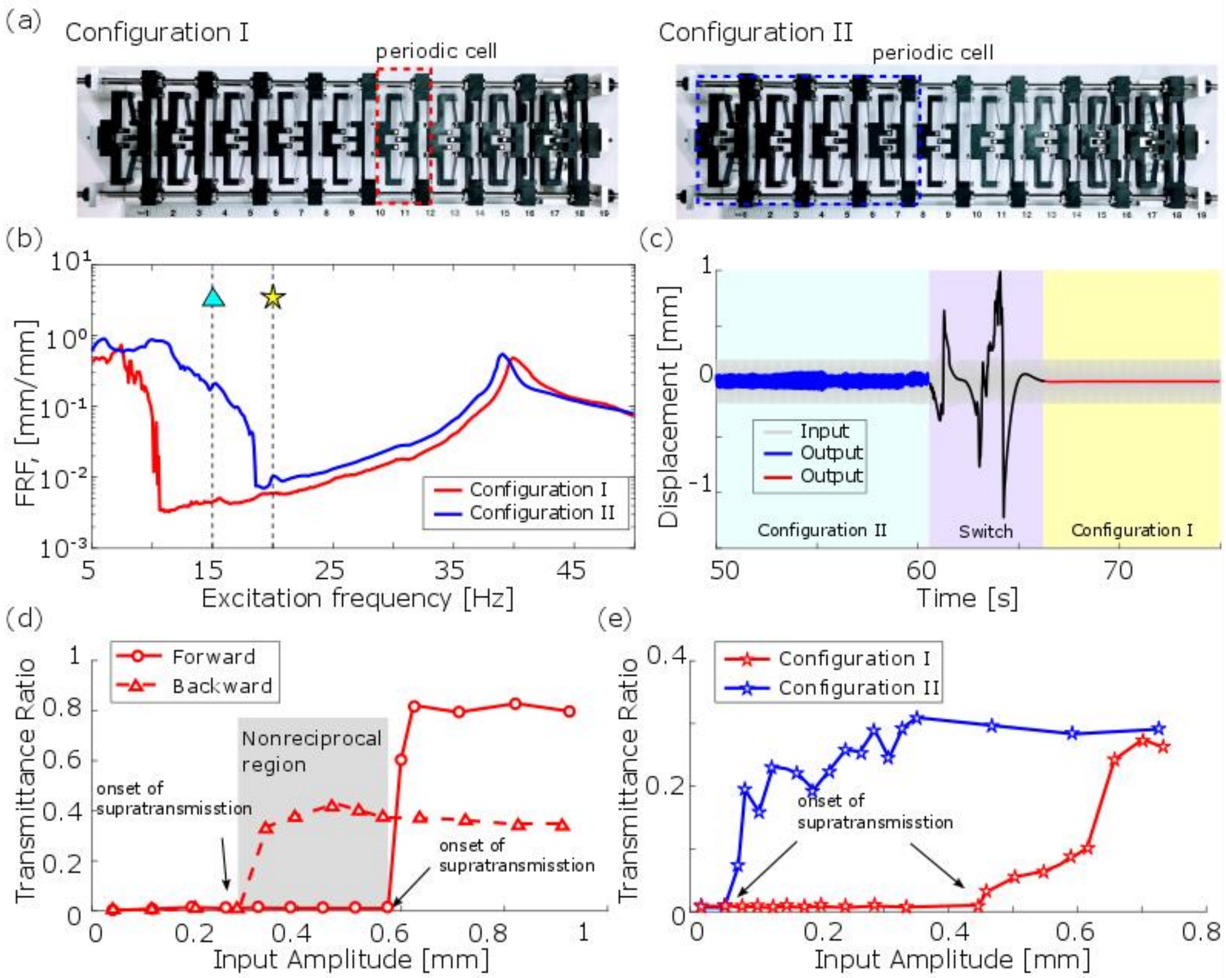

Figure 31.(a) Top view of experiment setup with two different configurations. Two configurations can be reconfigured by switching between metastable states. Periodic cell of each configuration is highlighted with dashed box. (b) FRF of output displacement over input displacement as input excitation frequency changes for configuration I (red) and configuration II (blue) with small excitation level. Frequency 15Hz (triangle) is in the passband for configuration II and stopband for configuration I and 20Hz (star) is in the stopband for both configurations. (c) Time history of output displacement with input RMS displacement 0.2 mm and input frequency at 15Hz. Signal changes in-situ from propagating to non-propagating as configuration changes from configuration II to I. (d) Transmittance ratio (TR) for forward (circles connected with solid line) and backward (triangles connected with dashed line) actuation for configuration I with input frequency at 15Hz. Shaded area denotes the region of non-reciprocal wave propagation. (e) Transmittance ratio (TR) for configurations I and II under forward actuation at 20Hz (circles connected with solid lines), demonstrating the adaptiveness of supratransmission.

5.4.2 Analysis results – generation of non-reciprocal wave propagation

To understand the mechanisms of non-reciprocal wave propagation of the proposed system, a detailed numerical analysis is performed using the same system parameters for dispersion analysis discussed in Sec. 5.3.3. Wave propagation characteristics are first explored for configuration A, defined in Figure 30, under both forward and backward actuations. Small damping coefficients $\zeta = c/\sqrt{k_1 m_1}$ = 0.001 is applied between lattices and simulations are performed for sufficiently long time ($30000\omega_1$ where ω_1 is defined as $\sqrt{k_1/m_1}$) to reach steady state. Small damping coefficients are chosen to limit the influence of energy dissipation on the transmission reduction phenomenon. Figure 32 depicts the displacement time history and FFT of corresponding velocities for input x_{in} (magenta), output x_{out} (cyan) and response of internal mass adjacent to input x_1 (gray), Figure 28(c). Driving frequency $\omega = 1.15$ is chosen to be within the attenuation band $[0.633, 2]$ of the metastructure for configuration A from dispersion analysis and two input amplitudes $\delta = 0.1$ and 0.5 are considered.

For small input amplitude $\delta = 0.1$, despite the large discrepancy on steady state amplitude of internal mass (gray) between backward and forward actuations, the output response amplitudes (cyan) are both negligible compared to that of the input (magenta), Figure 32(a) and (c). Difference in response amplitudes of the internal masses is due to the inherent spatial asymmetry of the metastable chain introduced by modules with different elastic constituents. With finite lattice length, one end of the chain is grounded via a linear constituent whereas the other end is fixed through a nonlinear constituent, Figure 1. To understand the wave propagation characteristics, FFT of the corresponding velocities are depicted in Figure 32 (b) and (d). Red dashed lines are band structure boundaries ω_{A1}, ω_{A2} and ω_{A3} determined from the linear analysis, Figure 30 (b). For both actuation scenarios, majority of the energy is localized around the fundamental driving frequency ω_d as well as its higher harmonics $2\omega_d$ and $3\omega_d$, Figure 32 (b) and (d). In complement to the time domain analysis, the FFT results also reveal that response amplitude of the internal mass for backward actuation is orders of magnitude greater than that for the case of forward actuation, due to the inherent spatial asymmetry. In fact, amplitude of the second harmonic $2\omega_d$ under backward actuation is still two times larger than the amplitude of fundamental harmonics ω_d under forward actuation. However, since these dominant frequencies reside within the stopband of the metastable lattices, majority of wave energy does not propagate through the metastable chain. As exemplified by the frequency response of output signal for both scenarios, dominant frequencies of the remaining wave energy are prominently localized inside the first passband. Yet, since the vibration amplitudes of the output signals are considerably reduced compared to that of the input, transmittance ratios are negligible.

As input amplitude increases to $x_{in} = 0.5$, wave propagation for forward excitation scenario is still largely prohibited, similar to the low amplitude actuation case, Figure 32 (e) and (f). However, comparing Figure 32 (e) and (g), the response of output signal increases substantially for backward actuation. More specifically, with large enough input amplitude, the subsequent internal masses (gray) instantly undergoes large amplitude vibration, in this case chaotic response, Figure 32 (g). Therefore, even though the driving frequency is within the non-propagating zone, input frequency is immediately redistributed amongst a broad frequency range and wave energy is transmitted through the chain with frequencies spectrum primarily inside the propagating passband, Figure 32 (h). This frequency conversion property is a classical nonlinear phenomenon and substantiates previous researches in which supratransmission is enabled via nonlinear instability and the transmitted signal becomes quasiperiodic or chaotic [88] [94] [101] [196] [197]. Hence, we can conclude that non-reciprocal wave transmission with the proposed metastructure is facilitated through the interplay of spatial asymmetry, nonlinearity and periodicity. Use the same definition of transmittance ratio (TR), it is determined that with the given parameters, TR for forward and backward actuations are 0.01 and 3.73 respectively, demonstrating more than 2 orders of magnitude increase in transmittance as excitation direction changes and providing clear evidence of non-reciprocal wave transmission.

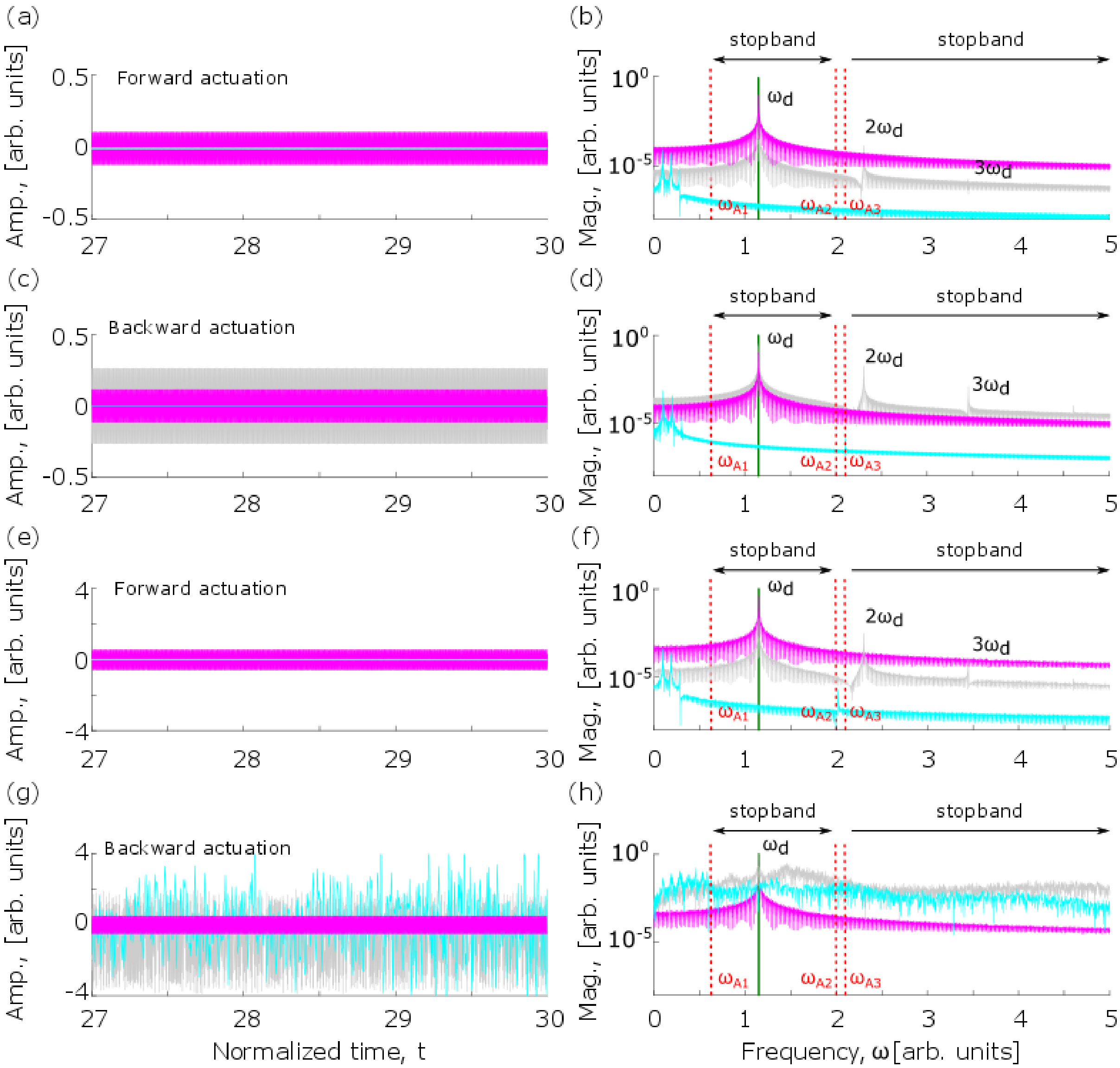

Figure 32. Steady state displacements of input (magenta), output (cyan) and internal (gray) masses for configuration A shown in Figure 3 under forward ((a) and (e)) and backward ((c) and (g)) actuation with excitation frequency $\omega_d = 1.15$

and excitation amplitude δ = 0.1 ((a) and (c)) and δ = 0.5 ((e) and (g)). (b), (d), (f) and (h), frequency domain analysis of corresponding velocities. Red dashed lines are band structure boundaries frequencies for configuration A predicted from linear analysis and green solid line is the input driving frequency. Time t is normalized with respect to the natural frequency $\omega_1 = \sqrt{k_1/m_1}$.

5.4.3 Analysis results - adaptive wave propagation

Experimental and numerical studies discussed in previous sections demonstrate the non-reciprocal wave transmission characteristics as input excitation amplitude varies. Experimental observations also indicate that such anomalous energy flow is not only a result of the nonlinearity and spatial asymmetry of metastructure, but also tightly related to the bandgaps of the periodic chain. To further investigate the influence of internal reconfiguration (change of metastable states) on the transmittance ratio (TR) and non-reciprocity of the metastable lattice, numerical analysis is performed on the same metastructure by varying both internal configuration and actuation scenarios. Figure 33(a) depicts the transmittance ratio as input amplitude changes under constant input frequency $\omega = 0.95$. This frequency is within the stopband for both configurations A and B. Similar to experiment investigations, starting in each configuration, harmonic excitation with fixed input amplitude is applied to one end of the chain depending on the excitation scenarios.

For small input amplitude, configuration A (red lines), both forward and backward actuations have small transmittance ratio, similar to previous observations. Yet, due to spatial asymmetry, as input amplitude increases to 0.3 m, transmittance ratio for backward actuation increases significantly by 2 orders of magnitude, red dashed line, whereas TR for forward actuation remains to be low, indicating the start of non-reciprocal wave transmission. Same as the experimental observation in Figure 31(d), backward actuation is able to trigger the onset of supratransmission with smaller excitation amplitude than forward actuation.

As input amplitude increases to 1.7, input energy is sufficient to trigger large amplitude vibration for forward actuation and is reflected by the large increase in transmission ratio, red solid line. Further increasing input amplitude beyond 1.7, wave energy will transmit in both directions. Hence, for configuration A, non-reciprocal wave transmission occurs for input amplitudes between 0.3 to 1.7. As the metastructure is changed to configuration B (bottom row in Figure 33 (a)) by switching between the metastable states (Figure 30(a)), with the same excitation frequency $\omega = 0.95$, amplitude range for such unidirectional energy transmission now shifts to between 0.1 to 0.2. This is due to the fact that comparing with configuration A, configuration B corresponds to a softer state, i.e. equilibrium position is at a shallower potential well, evidenced by a lower passband, Figure 30(b). Therefore, nonlinear instability is more readily attainable compared to configuration A. This demonstrates the adaptivity of non-reciprocal wave transmission characteristics as switching amongst the metastable states.

Additionally, as shown in Figure 30, alternating internal configurations can greatly affect the bandgaps of the metastable lattice, which is shown to be pivotal in manipulating frequency spectrum of the output signal, Figure 32. Hence, the effect of input frequency on the non-reciprocal wave transmission characteristics as switching amongst metastable states is investigated. Figure 6(b) illustrates the transmittance ratio as input frequency changes with constant input amplitude $\delta = 0.5$. It can be seen that for configuration A, non-reciprocal transmission exists for frequencies between [0.7, 1.7] and [2.3, 3] and is changed to [1.7, 2] and [2.5, 3] as switched to configuration B.

To further explore the adaptivity of wave propagation characteristics over a wide spectrum of input parameters, Figure 33 (c) depicts the transmittance ratio for forward and backward actuations with both configurations A and B as input frequency and amplitude varies. The transmittance ratio heat map shown in Figure 33 (c) are in log scale with lighter color region corresponds to larger TR values. As demonstrated in Figure 33 (c), for both configurations A and B, wave propagation characteristics for forward and backward actuations are considerably different for various combinations of input parameters. In fact, with the given system parameters, most of the signal transmit through the chain for backward actuation, whereas for forward actuation, wave energy does not propagate for some combinations of input frequency and amplitude in the parameter space, indicated by a greater area of dark space in Figure 33 (c). Such discrepancy in TR for two excitation directions creates region in parameter space in which non-reciprocal energy transmission exits. Additionally, this phenomenon is observed for most of the frequencies inside the stopbands. More intriguingly, as configurations switches from A to B, significant adaptation of wave propagation characteristics can be observed for forward actuations, Figure 33 (c). For instance, with input level $\delta = 1$ and frequency $\omega = 1.5$, initially blocked wave energy for configuration A can propagate through the chain as switched to configuration B. It’s also worth noting that the non-propagating zone for configuration B, indicated by the dark blue area is much smaller compared to that for configuration A, corroborating with the previously discussed fact that configuration B corresponds to a softer state. From these observations, we can conclude that the proposed metastable metastructure is invested with massive adaptivity of non-reciprocal wave propagation characteristics for a wide frequency range by switching amongst the metastable states.

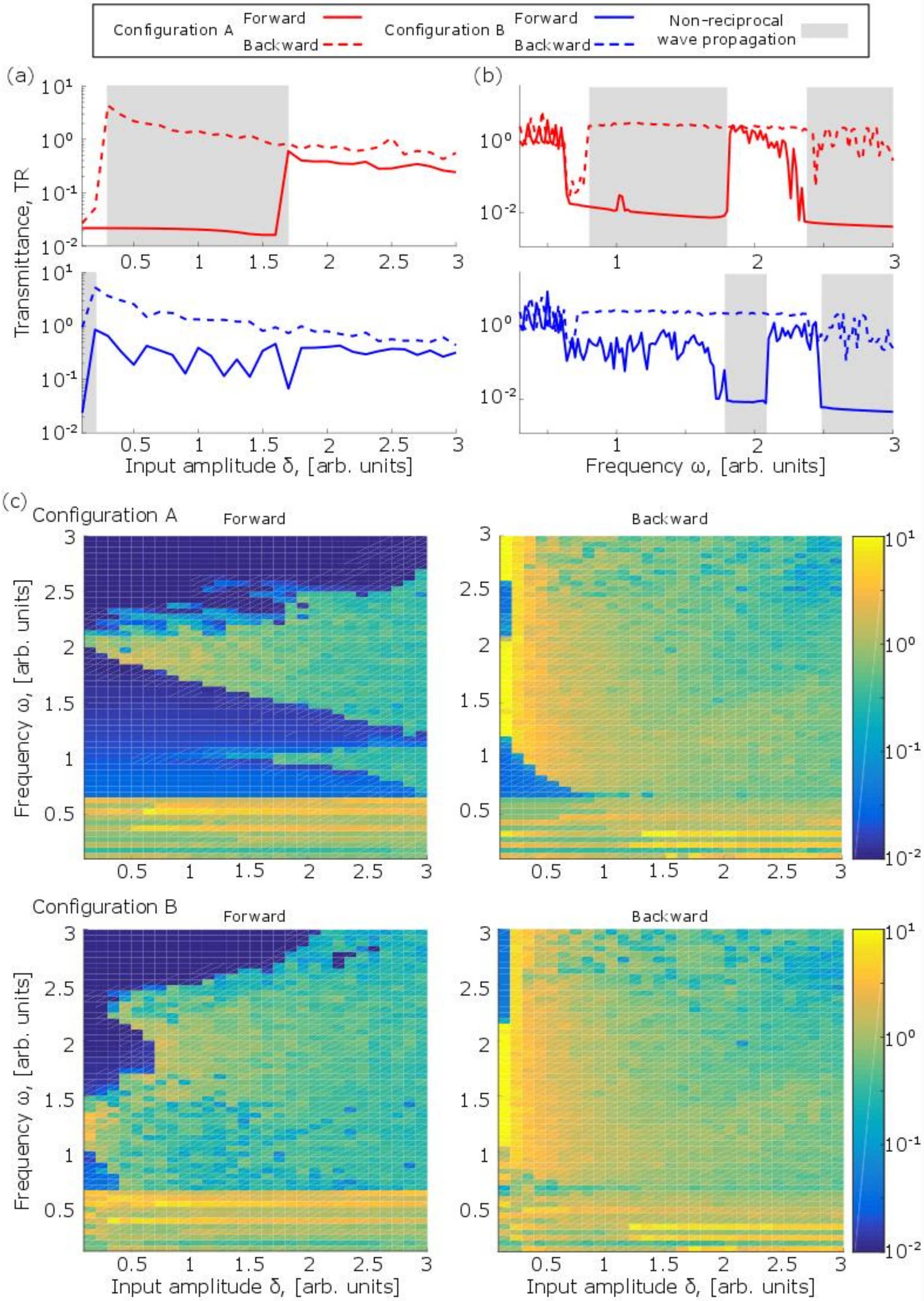
Configuration A
Forward
Backward
Configuration B
Forward
Backward
Non-reciprocal wave propagation
(a)
(b)
Transmittance, TR
Input amplitude δ, [arb. units]
Frequency ω, [arb. units]
(c)
Configuration A
Forward
Backward
Configuration B
Forward
Backward
Frequency ω, [arb. units]
Input amplitude δ, [arb. units]
10^{1}
10^{0}
10^{-1}
10^{-2}

Figure 33. (a) and (b) Transmittance ratio (TR) for metastructure under forward (solid line) and backward (dashed line) actuation for configuration A (red) and B (blue) with shaded areas denoting parameter space for non-reciprocal wave propagation. (a) Varying input amplitude with fixed frequency $\omega_d = 0.95$ and (b) Varying input frequency with fixed amplitude $\delta = 0.5$. Gray area indicates the region of non-reciprocal wave transmission. (c) Contour plot on transmittance ratio (vs. input frequency and amplitude) of forward and backward actuation for configurations A and B.

Chapter 6

Supratransmission in a Metastable Modular Metastructure

6.1 Chapter overview

From previous investigation in a metastable modular metastructure, we find that when the driving frequency is within the stopband of the periodic structure, there exists a threshold input amplitude, beyond which sudden increase in the energy transmission can be observed. This onset of transmission is due to nonlinear instability and is known as supratransmission. We show that due to spatial asymmetry of strategically configured constituents, such transmission thresholds could shift considerably when the structure is excited from different ends and therefore enabling the non-reciprocal energy transmission. While previous investigation presented a novel approach to achieve adaptable non-reciprocal wave propagation and showed great potential, in depth understanding of the mechanisms that are able to activate the onset of supratransmission and their implications on wave energy transmission potentials are not clear. Additionally, analytical tools that can provide guidelines to synthesize systems capable of attaining non-reciprocal wave propagation for desired operation ranges are lacking. Therefore, in this chapter, we aim to build upon the previous study and provide a thorough investigation and exploration on the abovementioned unresolved problems. Our goal is to advance the state of the art by providing understanding and insights on the rich and complicated dynamics in the proposed metastable modular metastructure and developing effective analytical tools for analyzing and synthesizing non-reciprocal wave energy propagation.

6.2 Route to supratransmission in the metastructure

With the same system parameters used to determine the bandgaps in Sec. 5.3.3, $k_1 = 2, k_2 = -3, k_3 = 1, k_L = 0.2$ and masses $m_1 = m_2 = 1$, wave propagation characteristics are explored using a 10 module metastructure over a wide spectrum of input parameters starting from free length configuration, i.e. $z = 0$. Given the system parameters, distance between the two equilibrium positions for the bistable constituents is 2. Small damping coefficients $\zeta = 0.001$ is applied between lattices and input $x_{in} = psin(\omega t)$ is prescribed to one end of the structure depending on excitation scenario with numerical simulations running for sufficiently long time ($30000\omega_1$ where ω_1 is defined as $\sqrt{k_1/m_1}$) to reach steady state. Small damping coefficients are chosen to limit the influence of energy dissipation on wave propagation phenomenon. To investigate the non-reciprocal effect, two actuation scenarios are considered: one is forward actuation with input x_{in} on the left side of the lattice chain and the other is backward actuation with input x_{in} on the right hand side of the chain. Discrete representations of the excitation scenarios are depicted in Figure 34. For both scenarios, displacement input x_{in} is directly applied to the mass next to the boundary of the chain and output signal x_{out} is measured one unit (two degrees of freedom) away from the other side of the boundary. Owning to asymmetry of the metastable module, periodic repeating unit for the two excitation scenarios are inherently different, highlighted with red dashed boxes respectively, Figure 34.

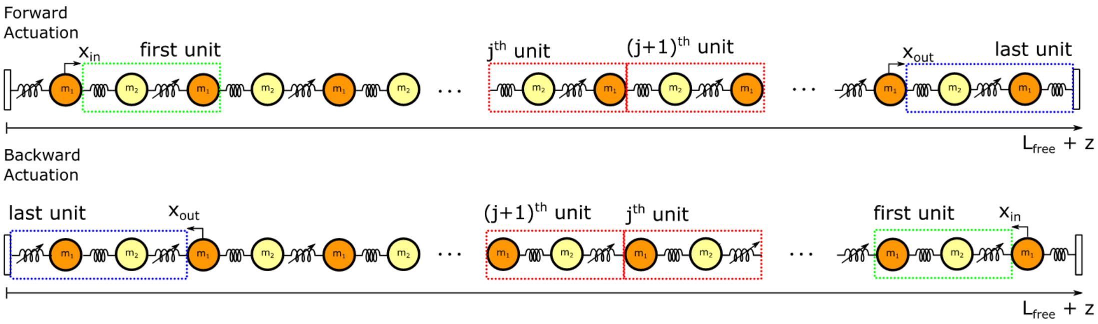

Figure 34. Conceptual diagrams of metastable module assembled in series under forward (excitation from left) and backward (excitation from right) actuations. For both scenarios, displacement input x_{in} is directly applied to the mass next to the boundary of the chain, and output signal x_{out} is measured one module away from the boundary. Repeating unit for both excitation scenarios are highlighted with red dashed box. The first and last units are highlighted with green and blue dashed boxes, respectively.

Figure 35 depicts the contour plot of the transmittance ratio (TR) of the metastructure as input frequency and amplitude varies for forward actuation scenario, Figure 34. The transmittance ratio (TR) is defined as the ratio of output RMS displacement over input RMS displacement $TR = |RMS(x_{out})|/|RMS(x_{in})|$. Hence, a higher transmittance ratio indicates more energy is transmitted through the metastructure. Contour plot is in log scale with brighter region corresponds to larger TR values. As shown in Figure 35, for input frequency inside the passband (PB) of the structure, since wave energy is able to propagate through the chain [21], transmittance ratio (TR) is always large. When excitation frequency is inside the stopband of the structure, an amplitude dependent wave transmission characteristic can be observed due to supratransmission [88] [94] [101] [198]. Upon close inspection, three distinct regions, labeled with I, II and III in Figure 35, with different input amplitude dependency can be identified when excitation frequency is inside the stopband. In this section, we will explore in detail different mechanisms that trigger the supratransmission phenomenon, which enables the energy transmission inside the bandgap.

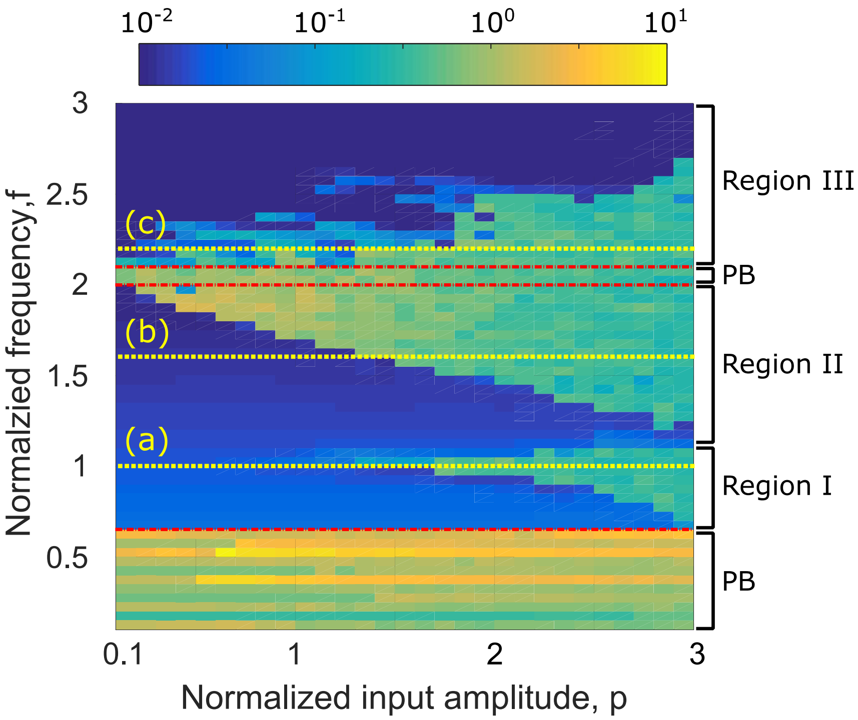

Figure 35. Contour plot on transmittance ratio (vs. input frequency and amplitude) for forward actuation from free length configuration. Passbands (PB) from dispersion analysis are within $(0, 0.632)$ and $(2, 2.098)$. Passbands are bounded by the red dash-dotted lines. For frequency inside the bandgaps, three regions, each with unique energy transmission characteristics depending on input frequency and amplitude can be identified, labeled with I, II and III. Representative frequency for each region is labeled with (a), (b) and (c) with yellow dashed lines, respectively.

6.2.1 Region I

To explore the characteristic dynamics in region I, input frequency $\omega = 1$ labeled with (a) in Figure 35 is chosen while excitation amplitude varies from 0.1 to 3 for forward actuation, Figure 34. From previous study in Chapter 5, we find that energy transmission is closely related to the dynamics of the first unit near the excitation; therefore, Figure 4 depicts both the bistable amplitude Y of the first unit and corresponding transmittance ratio as input amplitude increases. Bistable amplitude is defined to be the peak value of relative displacement between m_1 and m_2 at steady state and is chosen to represent the dynamics of the first unit. If the steady state response of the bistable constituent is periodic oscillation, bistable amplitude is represented with a single point in

Figure 36 for a fixed excitation level, whereas for aperiodic or chaotic oscillation, amplitude at steady state covers a wide range of magnitude and therefore is represented by a line. As input amplitude varies, 6 input levels $p =$ [0.15, 0.45, 0.8, 1.5, 1.77, 1.87], labeled A through F, are carefully inspected. Figure 37 depicts the phase diagram of the bistable displacement y and corresponding bistable velocity v of the first unit as well as the FFT of bistable velocity v. Bistable displacement y is defined to be the relative displacement between two masses at steady state and likewise bistable velocity v is the relative velocity. Black dots represent the equilibrium positions of the bistable constituents and red dots correspond to the stroboscopic map of the first bistable constituent.

With small excitation level $p = 0.15$, point A in Figure 36, the first bistable constituent undergoes intrawell oscillation (small amplitude oscillation around one of the equilibrium positions) with dominant frequency the same as the input frequency, Figure 37 (A). Since input frequency is inside the stopband, transmittance ratio is small as expected, Figure 36 (b), indicating that energy does not propagate through the chain. As excitation increases to for instance $p = 0.45$, point B in Figure 36, bistable amplitude bifurcates into two magnitudes. FFT of bistable velocity in Figure 37 (B) reveals that the vibration exhibits characteristics of superharmonic oscillation with dominant frequency twice as much as the driving frequency. Since all frequency spectrums with dominant magnitude are in the stopband, the TR remains to be low. Further increasing excitation level, steady state magnitude of the first bistable element becomes aperiodic. For instance, at $p = 0.8$, intrawell aperiodic oscillation occurs with frequency contents covering a broader spectrum and some of the frequency content now are inside the passband, Figure 37 (C) and hence transmittance ratio starts to increase to 0.04, indicating that vibration energy starts to propagate through the chain. As input level increases to approximately 1.3, bistable amplitude suddenly jumps and the vibration becomes chaotic interwell oscillation (large amplitude oscillation encompassing both equilibrium positions), point D and F in Figure 36. FFT of corresponding bistable velocity in Figure 37 (D) and (F) also illustrates that vibration energy of the constituent is diffused to a broader frequency spectrum with more frequency content inside the passband. Hence, such interwell chaotic oscillation leads to a noticeable increase in the transmittance ratio to 0.617 and 0.845 respectively for D and F, Figure 36 (b). Lastly, at excitation $p = 1.77$, bistable amplitude encompass a shorter range near one of its equilibrium positions at y = 2 (the other equilibrium position is at y = 0), point E in Figure 36 (a), indicating it undergoes intrawell oscillation. Phase diagram in Figure 37 (E) also corroborates this observation. From the FFT of bistable velocity, Figure 37 (E), it is determined that bistable constituent of the first unit undergoes a quasi-periodic intrawell oscillation, with more energy localized on frequency contents in the stopband compare to chaotic interwell oscillations, point D and F in Figure 36. Therefore, transmittance ratio at this excitation level drops correspondingly, point E in Figure 36 (b). These observations illustrate that the transmittance ratio is closely related to the dynamics of first unit. It is generally high when the first bistable constituent undergoes interwell or intrawell aperiodic/chaotic oscillation. Furthermore, for frequency range inside region I, supratransmission is shown to be facilitated through the nonlinear instability by transitioning from superharmonic vibration to aperiodic intrawell oscillation of the bistable constituent and transmittance ratio grows progressively as input amplitude increases.

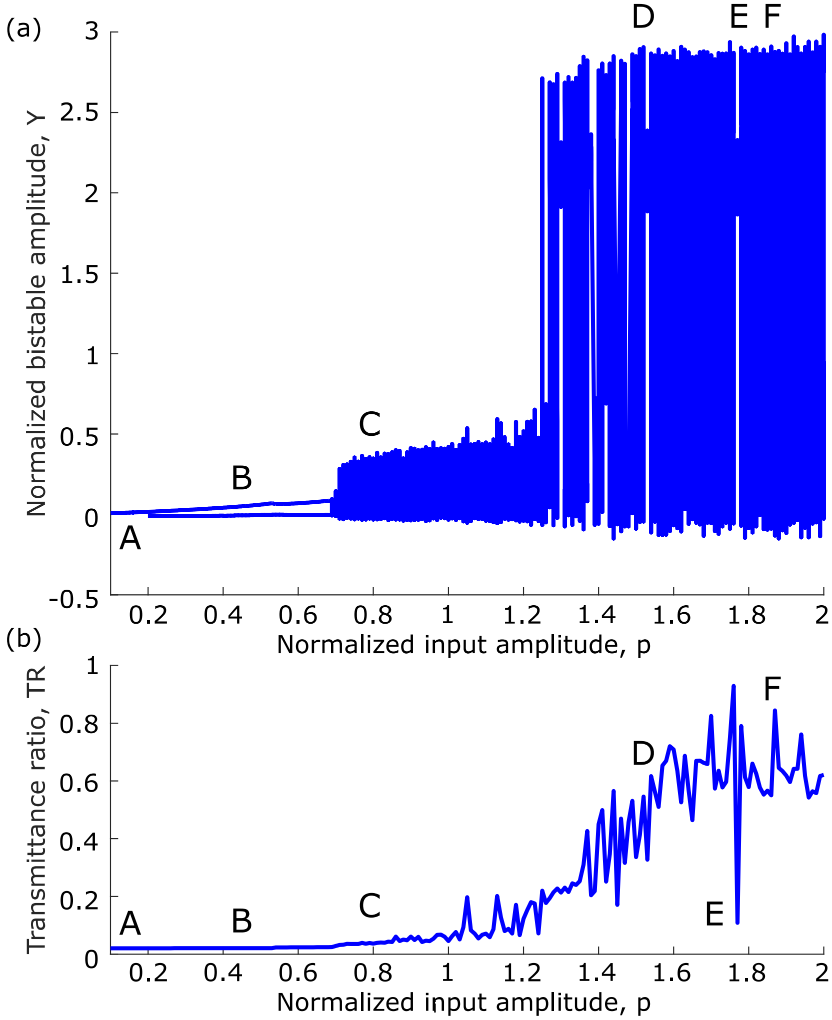

Figure 36. Normalized bistable amplitude of the first unit and corresponding transmittance ratio as input amplitude increases for forward excitation scenarios with input frequency $\omega = 1$. Bistable amplitude is determined to be the peak value of relative displacement between the two oscillators at steady state. A through F corresponds to input amplitude $p = [0.15, 0.45, 0.8, 1.5, 1.77, 1.87]$.

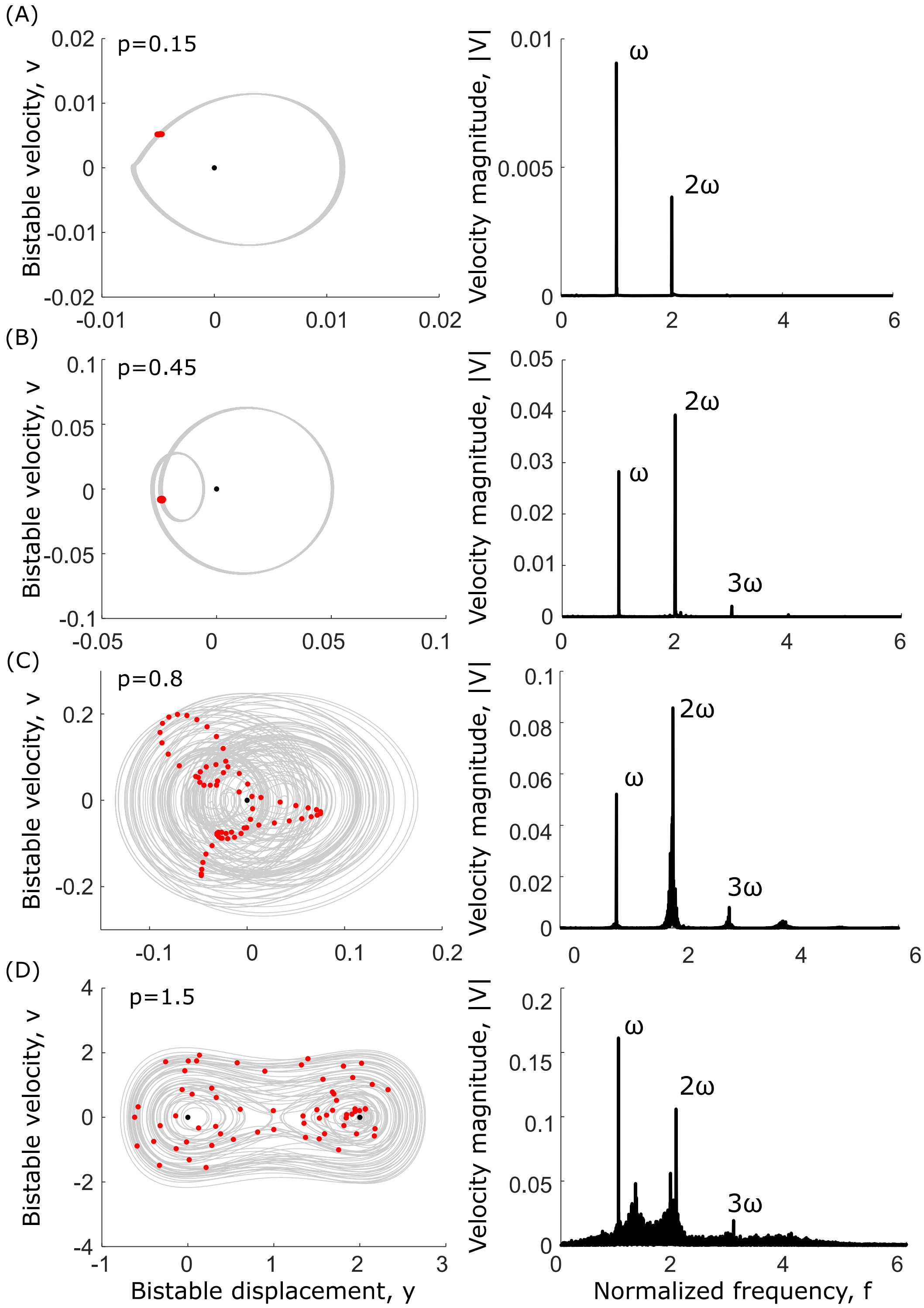

Figure 37. Phase diagram of the bistable constituent of the first unit under forward excitation, Figure 34, and corresponding FFT of the bistable velocity for different input excitation levels. (A) through (F) matches the same labels in Figure 36. Black

dots represent the equilibrium positions of the bistable constituents and red dots correspond to the stroboscopic map of the first bistable constituent. $\omega = 1$ denotes the input frequency.

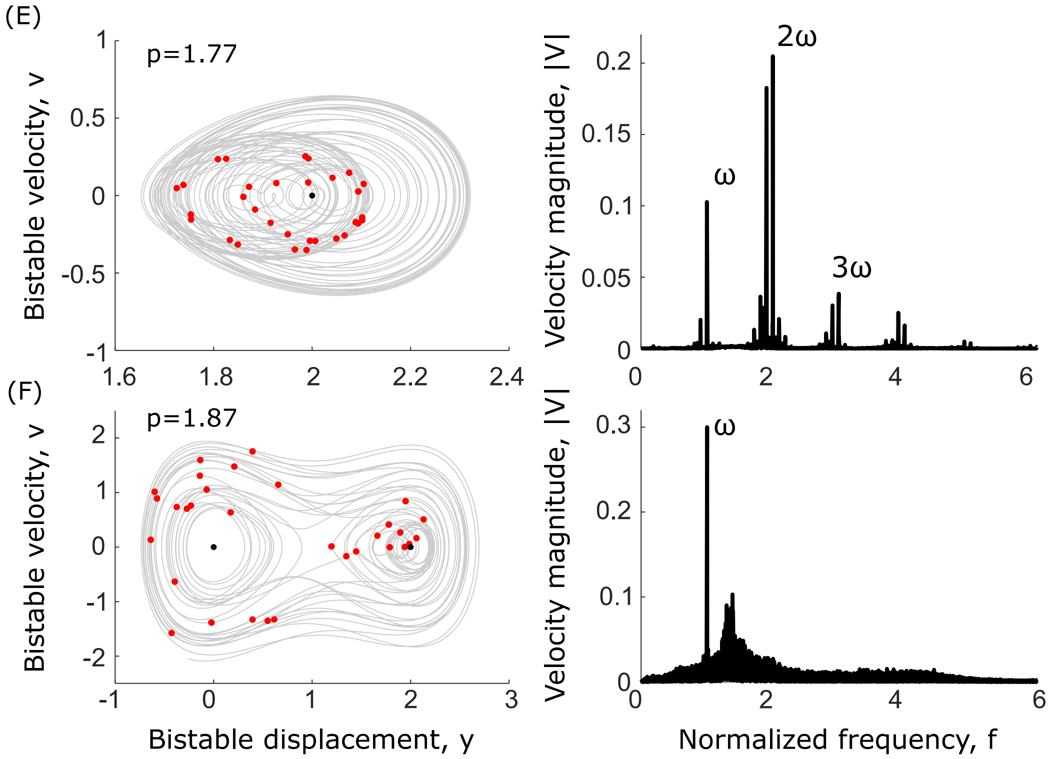

Figure 37. (Cont'd) Phase diagram of the bistable constituents of the first unit under forward excitation and corresponding FFT of the bistable velocity for different input excitation levels.

6.2.2 Region II

Similarly, to explore the characteristic dynamics in region II, input frequency $\omega = 1.6$ labeled with (b) in Figure 35 is chosen while excitation amplitude varies from 0.1 to 3 for forward actuation, Figure 34. Figure 38 depicts the bistable amplitude of the first unit and corresponding transmittance ratio as input amplitude increases. As input amplitude varies, representative input levels $p = [0.5, 1.27, 1.46, 1.85]$, are selected and labeled A through D. Figure 39 depicts the phase diagram of the bistable constituent for the first unit and FFT of corresponding bistable velocity. Red dots correspond to the stroboscopic map of the first bistable constituent.

Comparable to cases in region A, when excitation level is small, transmittance ratio is low, for instance $p = 0.5$ point A in Figure 38. As shown in Figure 38 (A), the first bistable element undergoes a small amplitude periodic intrawell oscillation with dominant frequency the same as the input frequency and corresponding transmittance ratio is only 0.01. As input amplitude increases to $p = 1.27$, vibration amplitude of the first bistable constituent increases significantly and the resultant vibration is characterized as chaotic interwell oscillation, Figure 39 (B) and (D). Correspondingly, more than two orders of magnitude increases in transmittance ratio is observed as dynamical characteristics of the first bistable constituent suddenly changes. Transitioning from intrawell to interwell oscillation for a bistable element as input amplitude increases is known to be caused by a saddle node bifurcation [138] [199] [200], therefore, for frequency range inside region II, supratransmission is triggered through the nonlinear instability of a saddle node bifurcation. Note that point C in Figure 38 corresponds to a near periodic large amplitude interwell oscillation yet the transmittance ratio is lower compared to the chaotic interwell oscillation case point B or D. This is because when first bistable element undergoes chaotic oscillation, it converts the frequency spectrum from the stopband to the passband more effectively, leading to more energy propagation through the chain and hence resulting in a higher TR [104] [198].

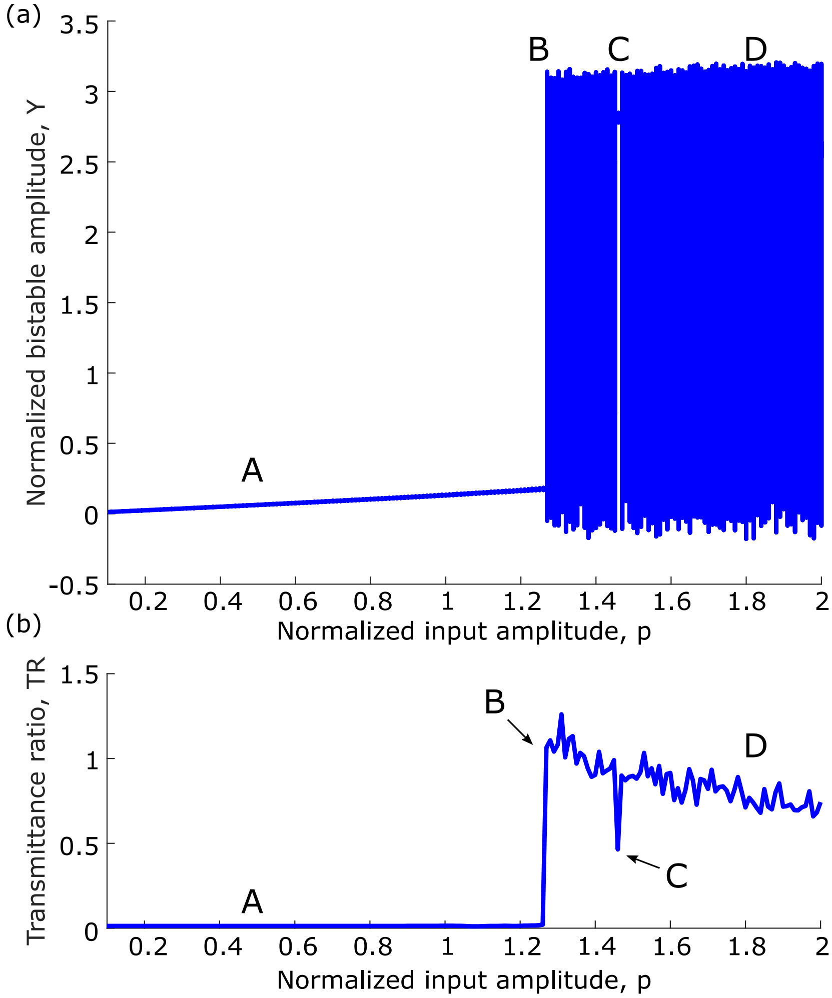

Figure 38. Normalized bistable amplitude of the first unit and corresponding transmittance ratio as input amplitude increases for forward excitation scenarios with input frequency $\omega = 1.6$. Bistable amplitude is determined to be the relative displacement amplitude between the two moving masses at steady state. A through D corresponds to input amplitude $p = [0.5, 1.27, 1.46, 1.85]$.

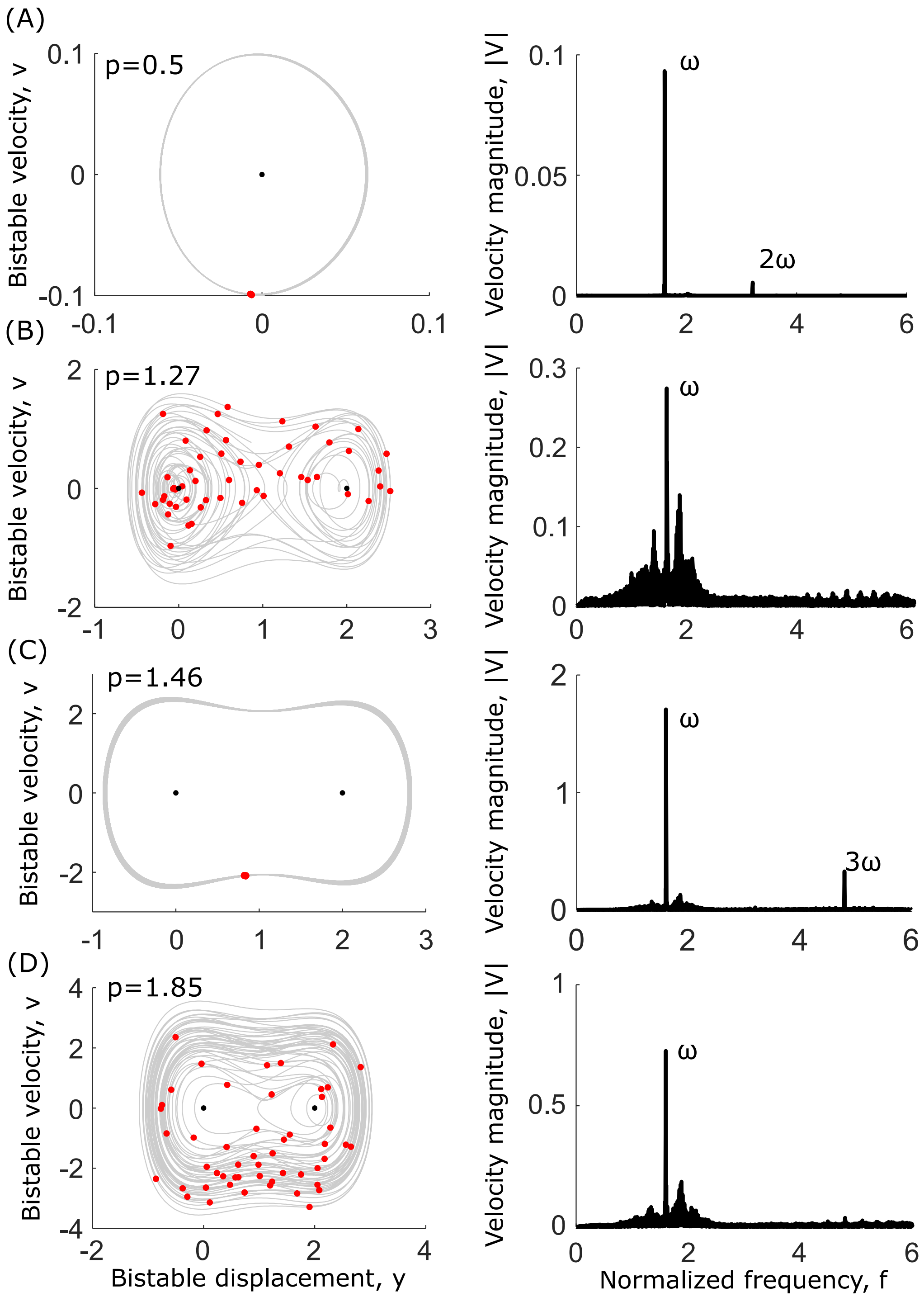

Figure 39. Phase diagram of the bistable constituents of the first unit under forward excitation Figure 34, and corresponding FFT of the bistable velocity for different input excitation levels. (A) through (D) matches the same labels in Figure 38. Black dots represent the equilibrium positions of the bistable constituents and red dots correspond to the stroboscopic map of the first bistable constituent. $\omega = 1.6$ denotes the input frequency.

6.2.3 Region III

Lastly, when excitation frequency is inside region III, we explored the characteristic dynamics with input frequency $\omega = 2.2$, labeled (c) in Figure 35. As indicated by the complicated TR pattern in Figure 40(b), for parameters in region III, we expect the dynamics of the first bistable element to be more intricate. Depicted in Figure 40(a), as input amplitude increases, dynamics of the first bistable element constantly transitions amongst periodic intrawell (point A and F), quasi-periodic intrawell (point B), aperiodic intrawell (point C), chaotic interwell (point D and G) and even subharmonic intrawell oscillation (point E). As a result, transmittance ratio frequently fluctuates up and down and is generally low for periodic intrawell and high for chaotic/aperiodic interwell/intrawell oscillations. In contrast to the previous two cases, for input frequencies in this region, there is no clear threshold on input amplitude beyond which vibration energy always propagates through the chain. However, when energy does propagate through the chain, supratransmission is still enabled via nonlinear instability, exemplified by the sudden change of vibration amplitude of the bistable element.

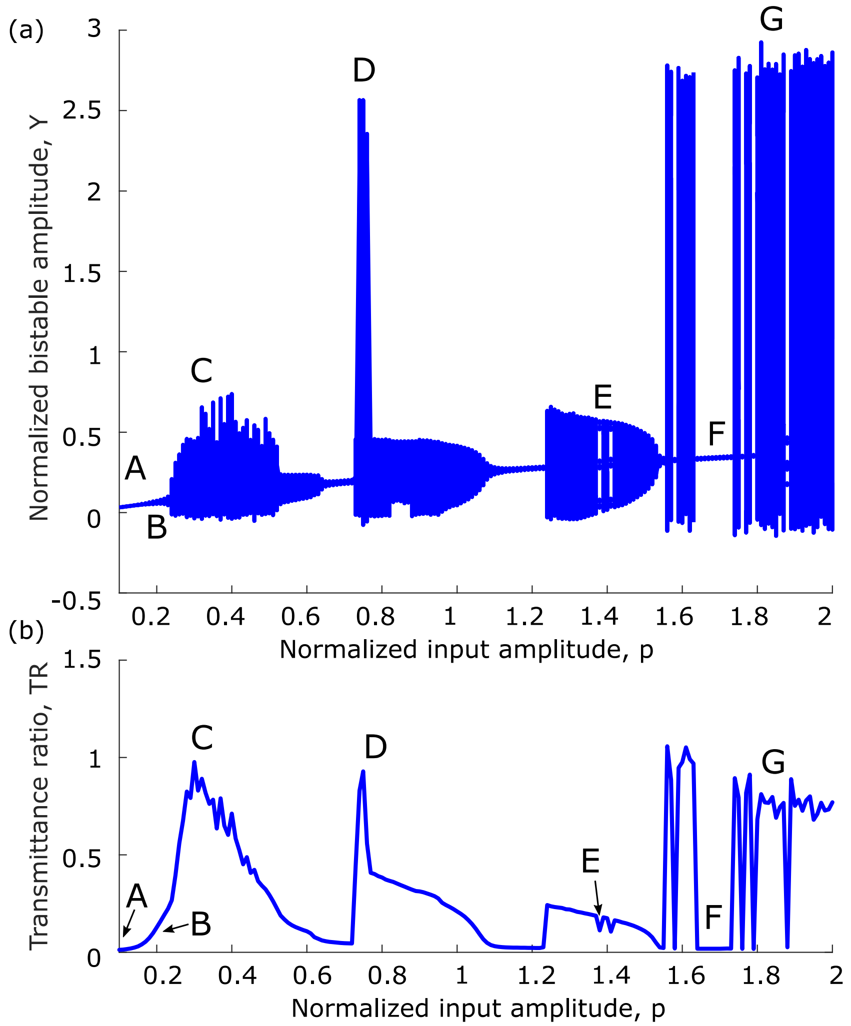

Figure 40. Normalized bistable amplitude of the first unit and corresponding transmittance ratio as input amplitude increases for forward excitation scenarios with input frequency ω=2.2. Bistable amplitude is determined to be the relative displacement amplitude between the two moving masses at steady state. A through G corresponds to input amplitude $\boldsymbol{p} = [\mathbf{0.1, 0.2, 0.3, 0.75, 1.38, 1.7\ 1.85}]$.

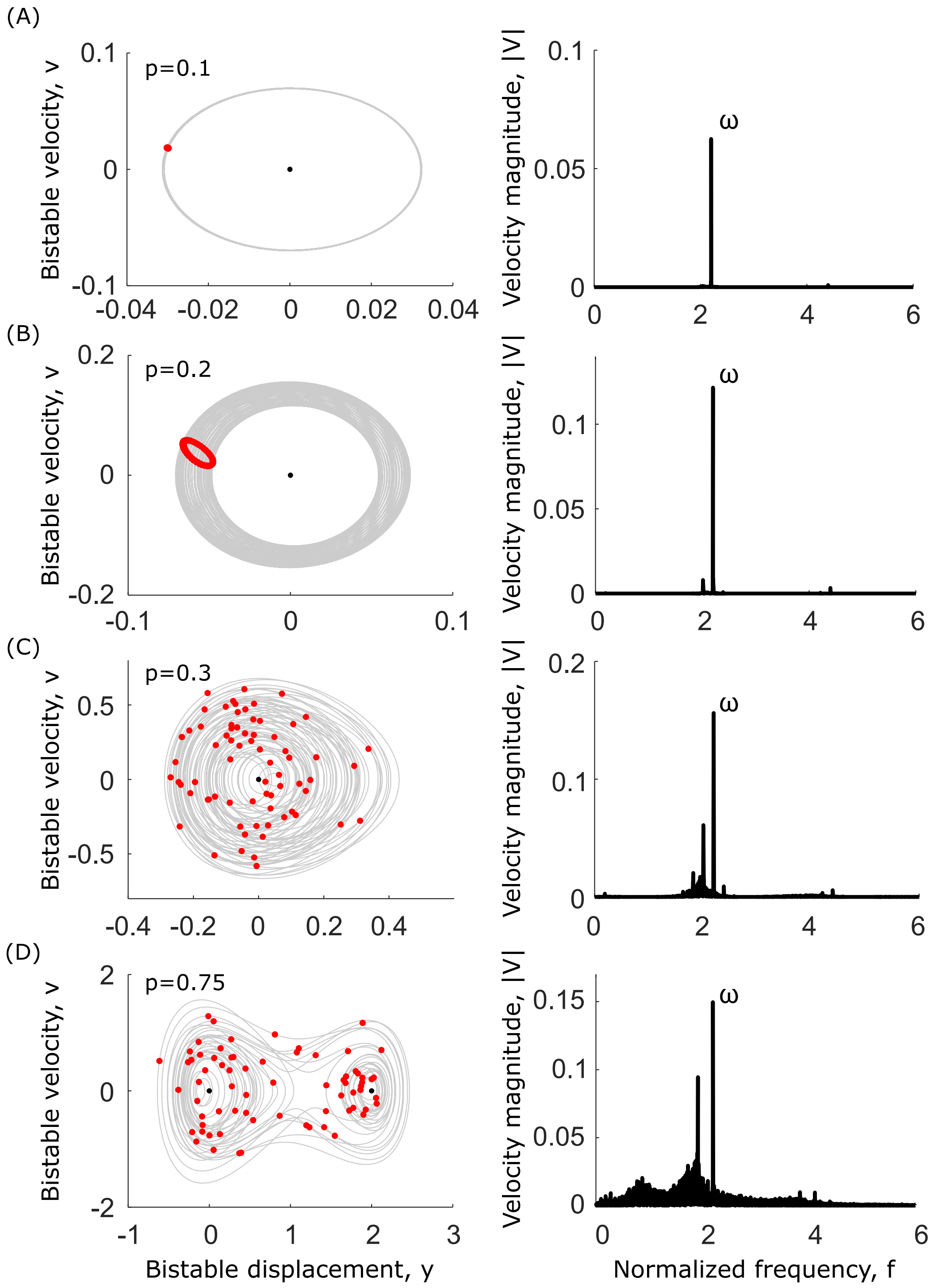

Figure 41. Phase diagram of the bistable constituents of the first unit under forward excitation, Figure 34, and corresponding FFT of the bistable velocity for different input excitation levels. (A) through (G) matches the same labels in Figure 40. Black dots represent the equilibrium positions of the bistable constituents and red dots correspond to the stroboscopic map of the first bistable constituent. $\omega = 2.2$ denotes the input frequency.

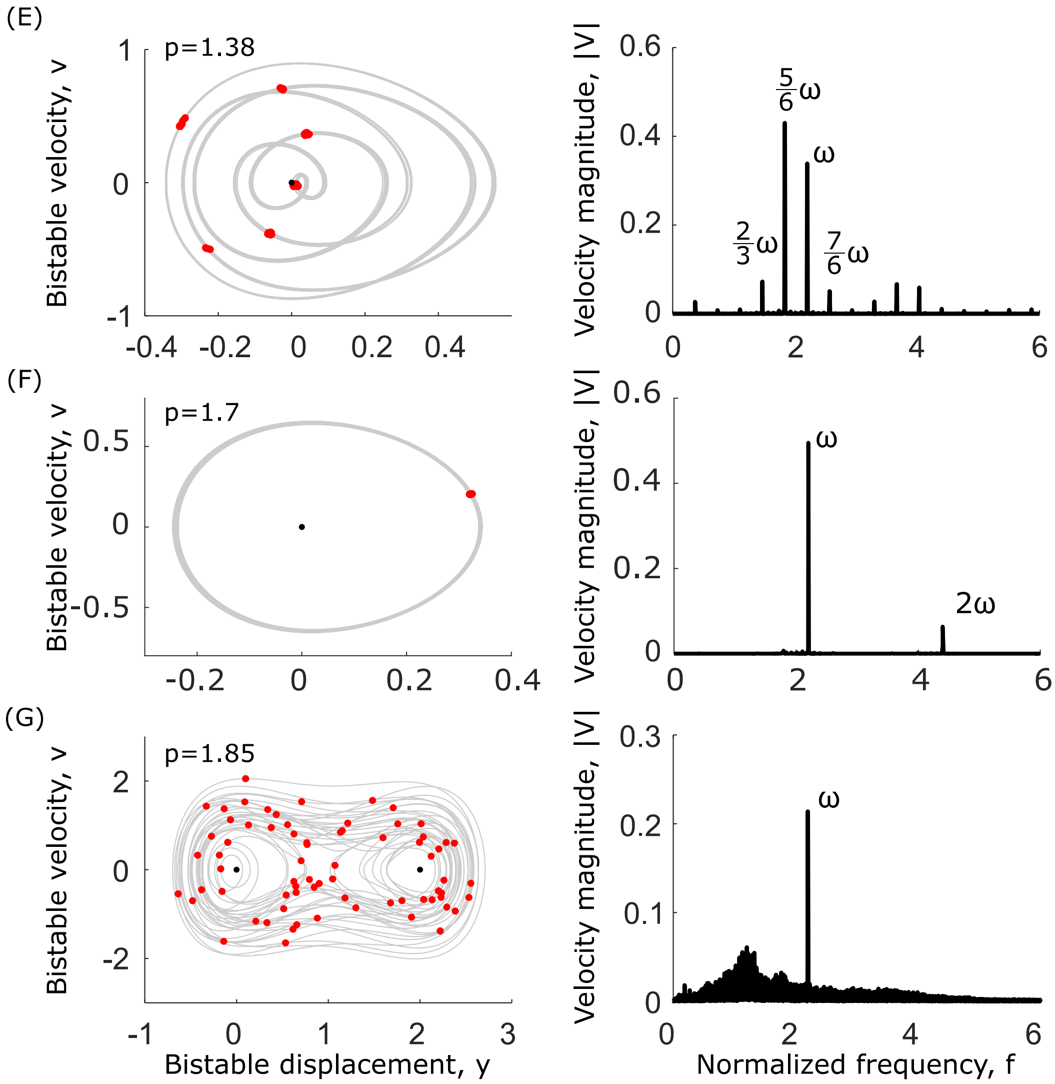

Figure 41. (Cont'd) Phase diagram of the bistable constituent of the first unit under forward excitation Figure 34, and corresponding FFT of the bistable velocity for different input excitation levels.

6.3 Predicting the onset of supratransmission and region of non-reciprocal transmission

From investigations discussed in Sec. 6.2, we noticeably observed the correlation between dynamics of the first bistable element with respect to the transmission ratio (TR) under forward actuation. This is mainly for two reasons: first is the weak coupling between the individual units (to maintain adaptable and metastable characteristics, strong coupling is not desired [193] [194]) and second is because the driving frequency is inside the stopband, vibration is prone to be localized closer to the excitation initially. Therefore, we seek to predict the onset of supratransmission by only retaining the nonlinear element of the first unit while linearizing the rest of the chain. With such a localized nonlinear-linear model, we are endowed with the opportunity to derive analytical solutions by using the transfer matrix method for the linear part [201] and interface with the harmonic balance method of the first nonlinear unit [200]. Similar concepts of treating the nonlinearity locally has been demonstrated to be effective in analyzing vibration characteristics for other nonlinear system [104] [202] [203]. Additionally, we noticed that when the first bistable element transitions from intrawell to interwell oscillation via a saddle node bifurcation (region II), a clear threshold on input amplitude can be identified beyond which drastic increase in transmittance ratio is observed. Such a rapid growth in transmittance ratio could potentially be used as a practical means for identifying regions of non-reciprocal response [198]. Therefore, in the following investigation discussed in this paper, we focus on analytically predicting the onset of supratransmission induced by the saddle-node bifurcation.

6.3.1 *Forward actuation*

Figure 42(a) depicts the schematic of the localized nonlinear-linear model for forward actuation in which nonlinearity is only preserved in the first unit. Governing equations of the j^{th} unit, Figure 42(b) can be expressed as:

$$m_1\ddot{w}_{[j+1]1} + \tilde{k}_1(w_{[j+1]1} - w_{[j]2}) + k_L(w_{[j+1]1} - w_{[j+1]2}) = 0 \qquad \text{(Eq. 36)}$$

$$m_2\ddot{w}_{[j]2} + \tilde{k}_1\left(w_{[j]2} - w_{[j+1]1}\right) + k_L(w_{[j]2} - w_{[j]1}) = 0 \qquad \text{(Eq. 37)}$$

for $1 \leq j \leq N-1$, where $\tilde{k}_1$ is the linearized stiffness of the bistable constituents and $w_{[j]1}$ and $w_{[j]2}$ are displacements from the new equilibrium positions for a fixed z and configuration.

After nondimensionalization, the governing equations become

$$\mu w''_{[j+1]1} + \tilde{\beta}_1(w_{[j+1]1} - w_{[j]2}) + (w_{[j+1]1} - w_{[j+1]2}) = 0 \quad \text{(Eq. 38)}$$

$$w''_{[j]2} + \tilde{\beta}_1\big(w_{[j]2} - w_{[j+1]1}\big) + (w_{[j]2} - w_{[j]1}) = 0 \quad \text{(Eq. 39)}$$

where the parameters are defined as

$$\omega^2 = k_{\mathrm{L}}/m_2\,;\ \mu = m_1/m_2\,;\ \tilde{\beta}_1 = \tilde{k}_1/k_{\mathrm{L}}$$

and the operator $(\quad)'$ represents a derivative with respect to nondimensional time t.

Figure 42(b) shows a schematic representation of two adjacent units in the assembled periodic structure. On both side of each unit, there is a pair of force and displacement. It should be noted that in this case $u_R^j = w_{[j+1]1}$ and $u_R^{j+1} = w_{[j+2]1}$. Balancing force at the left and right ends of the $(j+1)^{th}$ unit, we can derive the following relations:

$$u_R^{(j+1)} = \frac{-\omega^2+\tilde{\beta}_1}{\tilde{\beta}_1}u_L^{(j+1)} + \frac{\omega^2-1-\tilde{\beta}_1}{\tilde{\beta}_1}u_L^{(j+1)} = T_{11}^F u_L^{(j+1)} + T_{12}^F F_L^{(j+1)}$$

$$F_R^{(j+1)} = \frac{\mu\omega^4-\omega^2\tilde{\beta}_1(1+\mu)}{\tilde{\beta}_1}u_L^{(j+1)} + \frac{-\mu\omega^4+\omega^2(\tilde{\beta}_1+\mu+\tilde{\beta}_1\mu)-\tilde{\beta}_1}{\tilde{\beta}_1}F_L^{(j+1)} = T_{21}^F u_L^{(j+1)} + T_{22}^F F_L^{(j+1)}$$

From compatibility and force equilibrium between adjacent units we have $u_L^{(j+1)} = u_R^{(j)}$ and $F_L^{(i+1)} = -F_R^{(j)}$. The transfer matrix from j^{th} unit to $(j+1)^{th}$ unit can then be derived as:

$$\begin{bmatrix} u_R^{(j+1)} \\ F_R^{(j+1)} \end{bmatrix} = \begin{bmatrix} T_{11}^F & -T_{12}^F \\ T_{21}^F & -T_{22}^F \end{bmatrix} \begin{bmatrix} u_R^{(j)} \\ F_R^{(j)} \end{bmatrix}$$

Moving along the finite chain from the second to last unit to the first unit, we can write

$$\begin{bmatrix} u_R^{(N-2)} \\ F_R^{(N-2)} \end{bmatrix} = \begin{bmatrix} T_{11}^F & -T_{12}^F \\ T_{21}^F & -T_{22}^F \end{bmatrix}^{N-2} \begin{bmatrix} u_R^{(1)} \\ F_R^{(1)} \end{bmatrix} = \begin{bmatrix} M_{11}^F & M_{12}^F \\ M_{21}^F & M_{22}^F \end{bmatrix} \begin{bmatrix} u_R^{(1)} \\ F_R^{(1)} \end{bmatrix} \quad \text{(Eq. 40)}$$

For last unit, Figure 42(c), with fixed boundary conditions, governing equations can be expressed as:

$$\mu w''_{[N]1} + \tilde{\beta}_1(w_{[N]1} - w_{[N-1]2}) + (w_{[N]1}) = 0 \quad \text{(Eq. 41)}$$

$$w''_{[N-1]2} + \big(w_{[N-1]2} - w_{[N-1]1}\big) + \tilde{\beta}_1\big(w_{[N-1]2} - w_{[N]1}\big) = 0 \quad \text{(Eq. 42)}$$

It is then easy to get that $F_L^{(N-1)} = C_1 u_L^{(N-1)}$ where $C_1 = \frac{(\omega^4\,\mu-\omega^2\,(1+\tilde{\beta}_1+\tilde{\beta}_1\mu)+\tilde{\beta}_1)}{\omega^4\mu-\omega^2\,(1+\tilde{\beta}_1)\,(1+\mu)+(2+\tilde{\beta}_1)}$. Combining with Eq. (40), we can derive that

$$F_R^{(1)} = Cu_R^{(1)} = \frac{-C_1 M_{11}^{\mathrm{F}} - M_{21}^{F}}{(C_1 M_{12}^{\mathrm{F}} + M_{22}^{\mathrm{F}})} u_R^{(1)} \qquad \text{(Eq. 43)}$$

Lastly, governing equations for the first nonlinear unit, Figure 42(d) can be derived as:

$$\mu(x + y + x_{in})'' + \beta_1 y + \beta_2 y^2 + \beta_3 y^3 = F_R^1 \qquad \text{(Eq. 44)}$$

$$(x + x_{in})'' + (x) - (\beta_1 y + \beta_2 y^2 + \beta_3 y^3) = 0 \qquad \text{(Eq. 45)}$$

where x and y are deformations of linear and nonlinear springs and $\beta_1 = k_1/k_{\mathrm{L}}$, $\beta_2 = k_2/k_{\mathrm{L}}$, and $\beta_3 = k_3/k_{\mathrm{L}}$. Without loss of generality, we assume $\beta_1 = 2\beta_3$ and $\beta_2 = -3\beta_3$ to realize a symmetric bistable potential with distance between the two equilibria to be 2, similar to the potential profile used in previous numerical analysis.

Assuming 1-term expansion with slowly varying coefficients $x(t) = a(t)\sin(\omega t) + b(t)\cos(\omega t)$ and $y(t) = c(t)\sin(\omega t) + d(t)\cos(\omega t) + e(t)$, plugging Eq. (43), $u_R^1 = x_{in} + x(t) + y(t)$ and $x_{in} = psin(\omega t)$ into the equations of motion, eliminating higher order terms, and grouping the constant, sin(ωt) and cos(ωt) terms yields five equations for the coefficients, $a(t)$, $b(t)$, $c(t)$, d(t) and e(t)

$$2\omega b' = -p\omega^2 + (1 - \omega^2)a(t) + \left(-2 - \frac{3}{4}R_y^2 + 6e(t) - 3e(t)^2\right)\beta_3 c(t)$$

$$-2\omega a' = (1 - \omega^2)b(t) + \left(-2 - \frac{3}{4}R_y^2 + 6e(t) - 3e(t)^2\right)\beta_3 d(t)$$

$$2\mu\omega b' + 2\mu\omega e' = (-C - \mu\omega^2)p + (-C - \mu\omega^2)a(t) + \Big(2\beta_3 + \frac{3}{4}R_y^2 - C - \mu\omega^2 - 6\beta_3 e(t) +$$
$$3\beta_3 e(t)^2\Big)c(t)$$

$$-2\mu\omega c' - 2\mu\omega a' = (-C - \mu\omega^2)b(t) + \left(2\beta_3 + \frac{3}{4}R_y^2 - C - \mu\omega^2 - 6\beta_3 e(t) + 3\beta_3 e(t)^2\right)d(t)$$

$$0 = -2\beta_3 e(t) + 3\beta_3 e(t)^2 - \beta_3 e(t)^3 + \left(\frac{3}{2} - \frac{3}{2}e(t)\right)\beta_3 R_y^2$$

where R_y is the bistable amplitude with $R_y^2 = c(t)^2 + d(t)^2$

Combining the five equations, a third order polynomial in terms of $R = R_y^2$ can be derived [200]:

$$\rho_3 R^3 + \rho_2 R^2 + \rho R + \rho_0 = 0$$

where

$$\rho_3 = \frac{1}{16\,(-1+\omega^2)^2}\left(225\,C^2\,\beta_3^2 + 450\,C\,{\beta_3}^2\,(-1+(1+\mu)\omega^2) + 225\,{\beta_3}^2(-1+(1+\mu)\omega^2)^2\right)$$

$$\begin{aligned}\rho_2 = \frac{1}{16\,(-1+\omega^2)^2}(&-120\,C^2\beta_3 - 240\,C^2{\beta_3}^2 + 120\,C^2\beta_3\omega^2 - 120\,\beta_3\,(-1\\ &+(1+\mu)\omega^2)\,(-\mu\,\omega^2\,(-1+\omega^2) + 2\,\beta_3\,(-1+(1+\mu)\omega^2))\\ &-120\,C\,\beta_3\,(4\,\beta_3\,(-1+(1+\mu)\omega^2) - (-1+\omega^2)\,(-1+(1+2\,\mu)\omega^2)))\end{aligned}$$

$$\begin{aligned}\rho_1 = \frac{1}{16\,(-1+\omega^2)^2}(&64\,C^2 - 128\,C^2\omega^2 + 64\,C^2\omega^4 - 128\,C^2\beta_3 + 128\,C^2\omega^2\beta_3 + 64C^2{\beta_3}^2\\ &+16\,\left(\omega^2\,(-1+\omega^2)\mu - 2\,\beta_3\left(-1+\omega^2(1+\mu)\right)\right)^2 + 64\,C\,(-1+\omega^2\\ &+\beta_3)\,(-\omega^2\,(-1+\omega^2)\,\mu + 2\,\beta_3\,(-1+\omega^2\,(1+\mu))))\end{aligned}$$

$$\rho_0 = \frac{1}{16(-1+\omega^2)^2}(-16\mathrm{C}^2p^2 - 32\mathrm{C}p^2\mu\omega^2 - 16p^2\mu^2\omega^4)$$

This polynomial can be further simplified as $R^3 + a_2R^2 + a_1R + a_0 = 0$ with leading coefficients to be 1. Transmission threshold corresponding to a saddle-node bifurcation can then be determined by solving the equation

$$a_0 = -2 \times (P + \sqrt{Q^3}) \qquad \text{(Eq. 46)}$$

where $P = (a_2^3)/27 - (a_1a_2)/6$ and $\mathrm{Q} = (a_2^2)/9 - a_1/3$

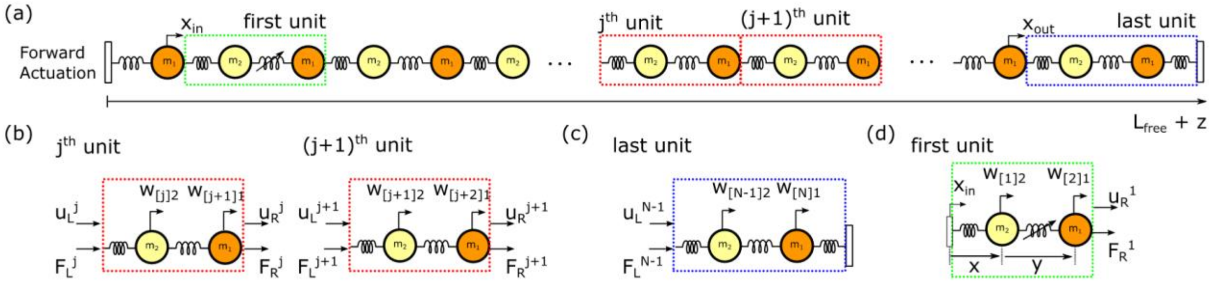

Figure 42.(a) Discrete chain of localized nonlinear-linear model for forward actuation; Only the first unit adjacent to input is nonlinear (b) Schematic of j^{th} and $(j+1)^{th}$ unit for transfer matrix analysis. Subscript in square bracket corresponds to the index of metastable module shown in Figure 34. (c) Schematic of the last unit for transfer matrix analysis. (d) Schematic of first unit for harmonic balancing analysis.

6.3.2 Backward actuation

Following the same procedure, transfer matrix from the second to last unit to the first unit for backward actuation, Figure 43, can be derived as

$$\begin{bmatrix} u_R^{(N-2)} \\ F_R^{(N-2)} \end{bmatrix} = \begin{bmatrix} T_{11}^B & -T_{12}^B \\ T_{21}^B & -T_{22}^B \end{bmatrix}^{N-2} \begin{bmatrix} u_R^{(1)} \\ F_R^{(1)} \end{bmatrix} = \begin{bmatrix} M_{11}^B & M_{12}^B \\ M_{21}^B & M_{22}^B \end{bmatrix} \begin{bmatrix} u_R^{(1)} \\ F_R^{(1)} \end{bmatrix} \qquad \text{(Eq. 47)}$$

where $T_{11}^B = -\omega^2 + 1$, $T_{12}^B = (\omega^2 - 1 - \tilde{\beta}_1)/\tilde{\beta}_1$, $T_{21}^B = \omega^4\mu - \omega^2(1+\mu)$, and $T_{22}^B = (-\omega^4\mu + \omega^2(1 + \mu + \tilde{\beta}_1\mu) + \tilde{\beta}_1)/\tilde{\beta}_1$. With fixed boundary conditions, we can derive that

$$F_R^{(1)} = Cu_R^{(1)} = \frac{-C_1 M_{11}^{\mathrm{F}} - M_{21}^F}{(C_1 M_{12}^{\mathrm{F}} + M_{22}^{\mathrm{F}})} u_R^{(1)} \qquad \text{(Eq. 48)}$$

where $C_1 = \frac{\tilde{\beta}_1 \left(\tilde{\beta}_1 + \omega^4\mu - \omega^2(1 + \tilde{\beta}_1 + \mu)\right)}{(\tilde{\beta}_1\,(2 + \tilde{\beta}_1) + \omega^4\mu - \omega^2(1 + \tilde{\beta}_1)\,(1+\mu))}$.

For the first nonlinear unit, Figure 43(d), assuming 1-term expansion with slowly varying coefficients $x(t) = a(t)\sin(\omega t) + b(t)\cos(\omega t)$ and $y(t) = c(t)\sin(\omega t) + d(t)\cos(\omega t) + e(t)$, plugging Eq. (47), $u_R^1 = x_{in} + x(t) + y(t)$ and $x_{in} = psin(\omega t)$ into equations of motion, eliminating higher order terms, grouping the constant, sin(ωt) and cos(ωt) terms and combining the equations, a third order polynomial can be similarly derived for $R = R_y^2$ where R_y is the bistable amplitude with $R_y^2 = c(t)^2 + d(t)^2$:

$$\rho_3 R^3 + \rho_2 R^2 + \rho R + \rho_0 = 0$$

where

$$\rho_3 = \frac{225}{16}\beta_3^2$$

$$\rho_2 = \frac{1}{16\,(-1 + C + \omega^2\mu)^2}\left(120\,\beta\,(-1 + C + \omega^2\mu)\,(C(-1 + \omega^2 - 2\,\beta) + 2\,\beta + \omega^4\mu - \omega^2(1 + \mu + 2\,\beta\,\mu))\right)$$

$$\rho_1 = \frac{1}{16\,(-1 + C + \omega^2\mu)^2}\left(16\left(C(-1 + \omega^2 - 2\,\beta) + 2\,\beta + \omega^4\,\mu - \omega^2\,(1 + \mu + 2\,\beta\,\mu)\right)^2\right)$$

$$\rho_0 = \frac{1}{16\,(-1 + C + \omega^2\mu)^2}\left(-16\,p^2\left(C(-1 + \omega^2) + \omega^2\,(-1 + (-1 + \omega^2)\mu)\right)^2\right)$$

This polynomial can be further simplified as $R^3 + a_2R^2 + a_1R + a_0 = 0$ with leading coefficients to be 1. Transmission threshold of the bifurcation can then be determined by solving the same Eq.(46) with newly derived coefficients a_1, a_2 and a_3 for backward actuation.

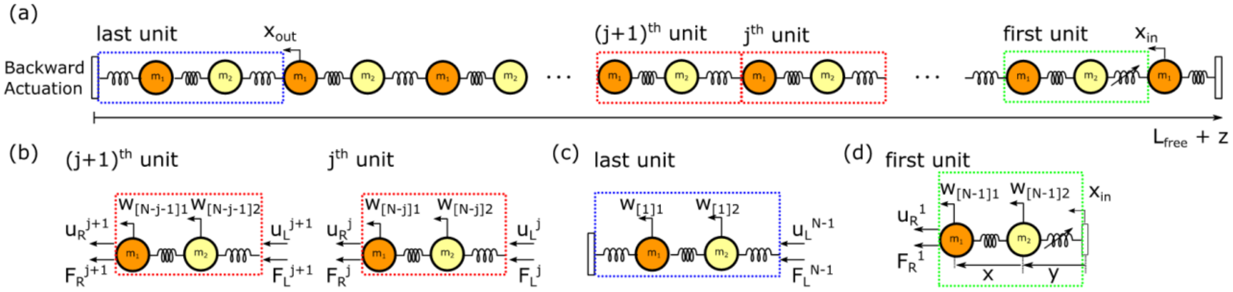

Figure 43.(a) Discrete chain of localized nonlinear-linear model for backward actuation; Only the first unit adjacent to input is nonlinear (b) Schematic of j^{th} and $(j+1)^{th}$ unit for transfer matrix analysis. Subscript in square bracket corresponds to the index of metastable module shown in Figure 34. (c) Schematic of the last unit for transfer matrix analysis. (d) Schematic of first unit for harmonic balancing analysis.

6.3.3 *Analytical results*

With the localized nonlinear-linear method described in Sec 6.3.1 and 6.3.2 for forward and backward actuations, we compare the analytical results with numerical investigations to evaluate the effectiveness of the analytical method. Parameters used for simulations are the same as in Sec. 6.2. Figure 44 depicts the contour plot on transmittance ratio as input frequency and amplitude varies for both forward and backward actuations, with dark area corresponds to non-propagation zone. Therefore, the boundaries of supratransmission in the parameter space correspond to the transitions of color from dark to bright. Solid red and black lines are analytical predicted onset of supratransmission for forward and backward actuations, respectively. As shown in Figure 44(a), the proposed method is able to predict accurately the onset of the supratransmission induced by the saddle-node bifurcation in region II discussed in Sec. 6.2 for forward actuation over a range of the parameters investigated. For backward actuation, analytical predicted boundary (black lines) also closely resembles the trend of the numerical simulation: input amplitude level required to facilitate the onset of supratransmission increases as input frequency decreases. Combining the two predicted boundaries, Figure 44(b), since it predicts that wave energy can only propagate through the chain with input parameters above the red (black) line for forward (backward) actuation scenario, there exists a region in parameter space that are bounded by the two predicted transition boundaries such that wave energy can only transmit in one direction. This demonstrates that the proposed metastable structure is capable of attaining supratransmission at different excitation level depending on the excitation directions.

In summary, by combining the supratransmission property of a nonlinear periodic chain with spatial asymmetry, we are able to enable non-reciprocal wave propagation and predict the non-reciprocal region using the proposed analytical approach. Overall, the localized nonlinear-linear model and prediction method proposed in the study are beneficial for identifying the unidirectional wave propagation region in the input parameter space, which can greatly reduce the computational time and complexity. It should be noted that in this study, as a proof of concept, we have focused on analytically predicting the onset of supratransmission induced mainly by the saddle-node bifurcation. On the other hand, as discussed in Sec. 6.2, onset of supratransmission can be facilitated through other intricate nonlinear instabilities as well, which could be predicted using similar approach. That is, utilizing the same principle of localized nonlinear-linear model, we could adopt different forms of harmonic expansion for the first nonlinear unit to derive other supratransmission boundaries of interest [204] [205] [206] [207].

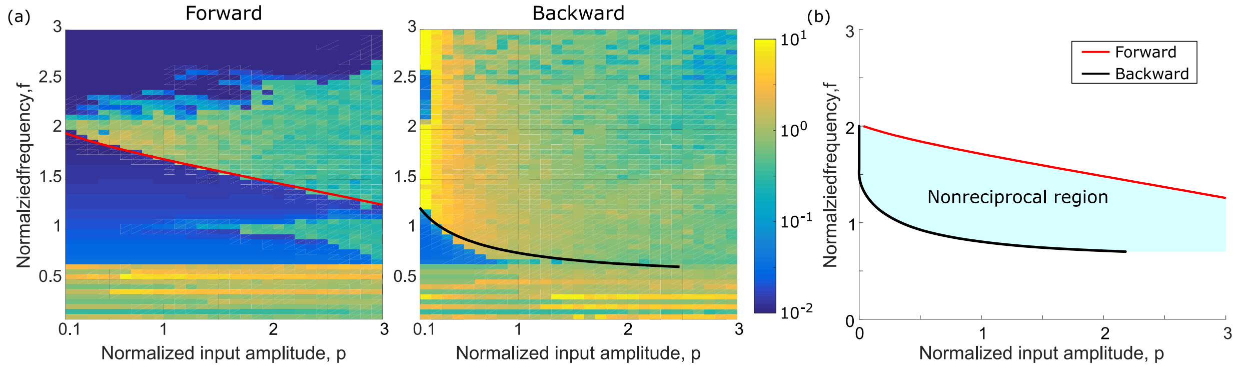

Figure 44. (a) Contour plot on transmittance ratio (vs. input frequency and amplitude) of forward and backward actuations for free length configuration with analytically predicted supratransmission boundaries. (b) Non-reciprocal region is bounded in between the two analytically predicted boundaries.

6.4 Parametric studies on supratransmission threshold

From both numerical and analytical investigations in Sec. 6.2 and 6.4, we find that when the excitation frequency is within the stopband of the metastructure, there exhibits a threshold input amplitude beyond which wave energy is able to propagate through the chain due to supratransmission. Additionally, when this onset of supratransmission is induced by saddle-node bifurcation, a drastic increase in transmittance ratio can be observed as input amplitude exceeds the threshold value and this sudden change could potentially be used as a practical means to design non-reciprocal regions. Therefore, in the following sections, we seek to explore influences of important parameters on the threshold amplitude to trigger supratransmission and to provide more insight for synthesizing systems with desired non-reciprocal characteristics.

6.4.1 Influence of damping coefficient

In this section, the influence of damping coefficients ζ on the threshold amplitude is studied. System parameters used are the same as in Sec 3 and 4 and excitation frequency is chosen to be $\omega = 1.6$. For exploration purposes, the metastructure is actuated under forward excitation scenario with damping coefficients ζ varying from 0.001, 0.005, 0.01, 0.05 to 0.1.

Figure 45 depicts the transmittance ratio as input amplitude increases for different damping coefficients. With small damping coefficients, $\zeta = 0.001$, $\zeta = 0.005$, and $\zeta = 0.01$, threshold amplitudes to trigger the onset of supratransmission gradually increase from $p = 1.27$ to $p = 1.28$ and $p = 1.31$. Additionally, due to the increased damping coefficient, energy transmitted through the structure in general decreases hence the transmittance ratio also decreases. As the damping ratio further increases to $\zeta = 0.05$ and $\zeta = 0.1$, the threshold amplitude required to enable supratransmission increases to 1.54 and 1.75 respectively and the transmitted energy drops drastically with transmittance ratio (TR) decreases from more than 1 to approximately 0.26. Therefore, increasing damping coefficients will increase the threshold amplitude required to trigger the onset of supratransmission and decrease the amount of energy propagated through the structure.

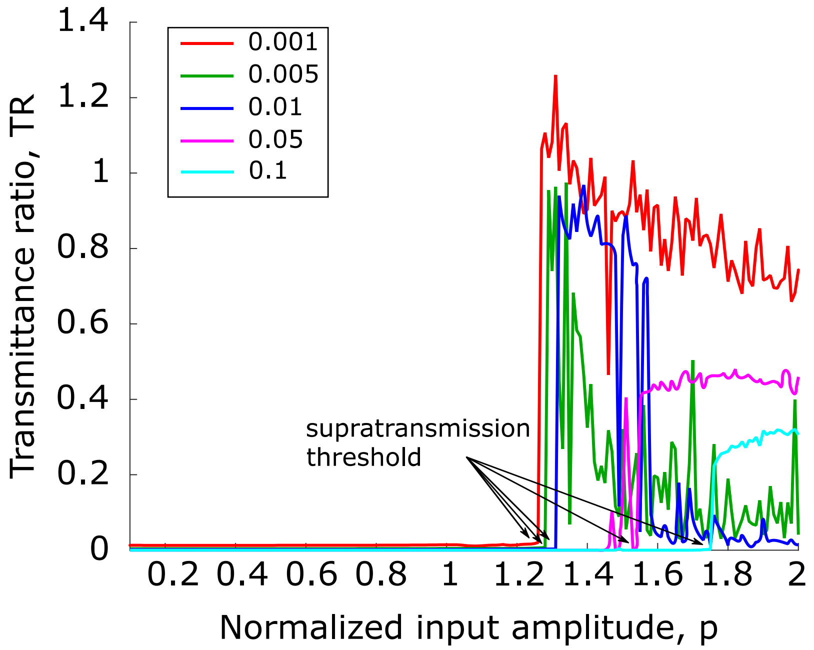

Figure 45. Transmittance ratio of metastructure under forward excitation as input amplitude increases for different damping coefficients $\zeta = [0.001, 0.01, 0.056, 0.1]$.

6.4.2 Influence of the number of modules

Results presented in the previous sections are all based on a 10 module assembly, in this section, the influence of module number N on the threshold amplitude is studied. System parameters used are the same as those used in Sec 6.2 and 6.3 with damping coefficients $\zeta = 0.001$. Again, for exploration purposes, the metastructue is actuated only under the forward excitation scenario.

Figure 46 depicts the threshold amplitude that enables supratransmission as module number increases from 5, 10, 20, 50 to 100 for a range of frequencies inside Region II, Figure 35. For a fixed excitation frequency, threshold amplitude initially may fluctuates with small module number and as the number of modules increases, this value becomes constant and is invariant of module number. Such an invariant characteristic is similarly observed in other nonlinear metamaterials [208]. Additionally, form the study of the 10 module assembly, we noticed that as the input frequency increases, the threshold amplitude to trigger supratransmission deceases, Figure 44. This trend is also true as module number changes from 5 to 100, that is, the threshold amplitude requires to facilitate supratransmission always decreases as frequency increases.

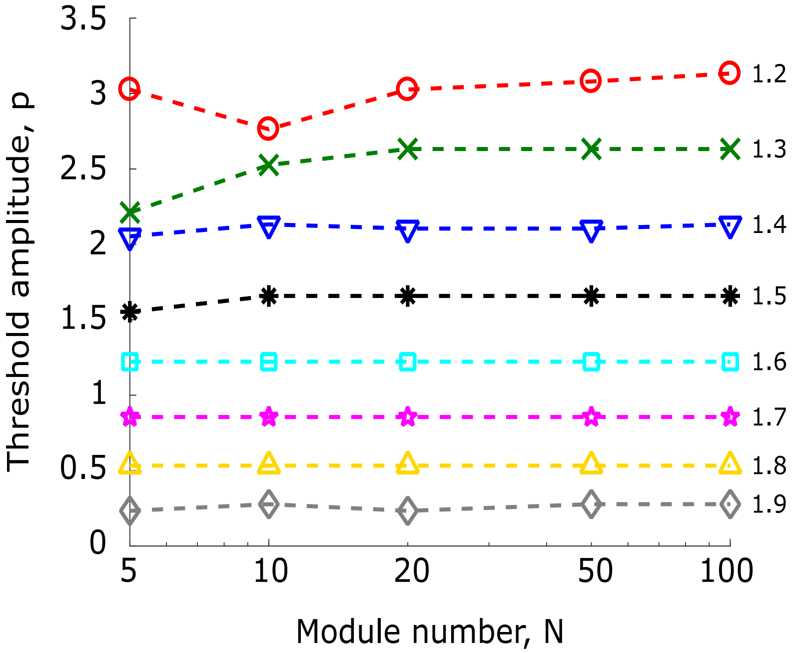

Figure 46. Threshold amplitude of metastructure under forward excitation for module number $\boldsymbol{N} = [\mathbf{5}, \mathbf{10}, \mathbf{20}, \mathbf{50}, \mathbf{100}]$ and excitation frequency $\boldsymbol{\omega} = [\mathbf{1.2}, \mathbf{1.3}, \mathbf{1.4}, \mathbf{1.5}, \mathbf{1.6}, \mathbf{1.7}, \mathbf{1.8}, \mathbf{1.9}]$.

Chapter 7

Concluding Remarks

7.1 Summary

This thesis presents the investigation of multifunctional adaptive structures by exploring and harnessing metastable modular mechanics and dynamics. Modular architected structures are studied and are referred to as “metastructure” as they behave in a way beyond the characteristics of their constituents. The critical features of the modular platform are the exploitation of multiple coexistent metastable states engendered via the strategic module design. By transitioning amongst the many metastable states, such a metastructure can concurrently achieve multiple programmable functionalities, including mechanical property tuning, topology adaptation, adaptive vibration and wave transmission controls.

Investigation using parallel assembly as testbed shows that modularity in an assembled structural system invests direct means to create and harness the metastable states of metastructures for programmable properties adaptivity. Experimental and analytical results exemplify that near-continuous properties adaptivity and stable topology change are effected as the number of assembled modules increases. The measurements also uncover opportunities to realize adjustable hysteresis (hence, energy dissipation) by harnessing the vast number of metastable states. Although the development of multi-module metastructures poses interesting design-based challenges, the incorporation of the analytical model into a novel GA routine demonstrates that the achievement of target global metastructure performance characteristics are met for preferred statistical distributions of key design variables at the local level, thereby closing the open-endedness of the design problem and guiding future assembly strategies.

Next, we explore the vibration and wave transmission control of a metastructure consisting of the metastable module assembled in series. The novel approach is able to realize the on-demand band structures and non-reciprocal wave propagation adaptation. We found that due to the inherent spatial asymmetry of the metastructure, the proposed nonlinear chain is able to trigger the onset of supratransmission at different excitation levels for forward and backward excitation scenarios, creating a region in parameter space in which unidirectional wave propagation can be realized. Additionally, exploiting the programmable properties facilitated via reconfiguring amongst the numerous modules and corresponding metastable states, the proposed metastructure exhibits unprecedented broadband non-reciprocal wave propagation and adaptation.

Since the proposed approach depends primarily on scale-independent principles, it could foster a new generation of reconfigurable structural and material systems with unconventional vibration control and wave transmission characteristics that are applicable to vastly different length scales for a wide spectrum of applications.

7.2 Research contributions

The following contributions are made to the understanding of metastructures:

1. Introduce metastable modules that can be synergistically assembled and individually tuned to create paradigm shift for multi-functional adaptive metastructures

2. Realize near continuous mechanical property adaptation using adaptive-passive approach by leveraging the synergistic interactions amongst large number of metastable states.
3. Illustrate the intricate nonlinear dynamics afforded by the metastructure and elucidate different kinds of nonlinear instabilities that facilitate the onset of supratransmission, a bandgap transmission phenomenon pertained to nonlinear periodic metastructure.
4. Utilizing this novel mechanism, supratransmission, together with inherent spatial asymmetry of strategically configured constituents to facilitate unprecedented broadband non-reciprocal vibration and wave transmission and on-demand adaptation.
5. Develop analysis and synthesis tools unique to the system by combining harmonic balancing and transfer matrix method to analytically determine the input threshold amplitude required to trigger supratransmission and estimate the range of excitation parameters for unidirectional vibration and wave transmission.

7.3 Recommendations for future work

7.3.1 High dimensional system

The metastructure studied in this thesis is a 1D mono-coupled periodic structure, meaning that the coupling between adjacent units is only one degree of freedom. While results of the assembly is capable of demonstrating the working principles behind the desired adaptive functionalities, mechanical property as well as vibration and wave transmission in multi-coupled higher dimensional (2-D and 3-D) systems is more complicated and is yet to be investigated. Therefore, building upon the insight learned and expanding from the 1-D principle, we will investigate the metastability and the synergistic effect of higher dimensional modules and systems; develop methodology that can holistically analyze and synthesize the desired system properties by strategically assembling the modules.

7.3.2 Reconfiguration mechanism

Currently, transitioning amongst metastable states is done manually. Hence another ongoing task will be exploring actuation methods to effectively reconfigure amongst the metastable states. One actuation approach is through direct local actuation, Figure 47(a). Targeted switching of internal states can be realized using magnetic/electric field-driven active materials [209] [210] [211] embedded in the bistable elements. Comparing to other responsive materials [212] [213] [214] [215], the electric and magnetic field responsive materials have advantages such as fast actuation speed, large actuation strain as well as high fracture toughness [211] [216] [217] [218]. The structure will be able to reconfigure amongst metastable states by activating electro- and magneto-active polymers, such as electrostrictive relaxor ferroelectric polymers, dielectric elastomers and magnetorheological elastomers that are responsive to electric or magnetic field and embedded in the constituents. Another approach is using global boundary control. For instance, in Figure 47(b), to change the metastable states from point 1 to point 2, we can first load and stretch the metastructure from d (point 1) to $d + s_2$ (point 3). Next, by turning off the load the metastructure will spontaneously return back to the stable position (point 4) with $d + s_1$. Then by compressing the structure to d, the internal states are transitioned from point 1 to point 2. Such reconfigurations can be realized by simple boundary controls. It should be noted that both proposed actuations can be readily extended, refined and applied to higher-dimensional systems.

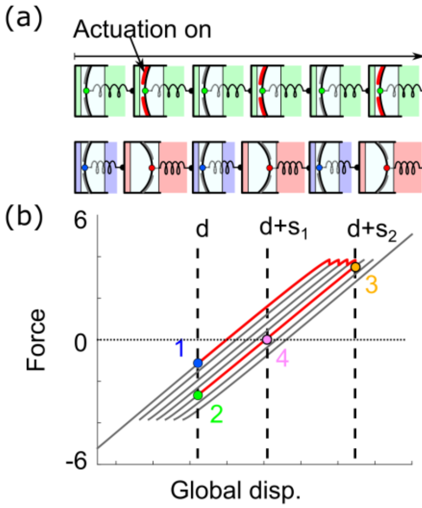

Figure 47. Illustration of switching amongst metastable states by either (a) internal local control or (b) global actuation

7.3.3 Band-limited excitation

The supratransmisson phenomenon studied in this thesis is triggered with single frequency spectrum. In real-world applications, it is not uncommon to encounter situations where excitation frequencies span a range of values [219] [220]. For excitations with entire frequency bandwidth within the stop band, one would expect phenomenon similar to supratransmission to occur. That is a sudden increase in the transmitted energy is expected to occur with excitation amplitude greater than a threshold. With single frequency spectrum, we observed that the non-reciprocal range decreases as excitation frequency increases, Sec. 6.3.3. This poses a potential limitation on the effectiveness of obtaining non-reciprocal wave energy propagation for a broad operation range. It remains unknown yet interesting to explore whether under the band-limited excitation, the proposed metastructure will exhibit similar characteristics or a uniform non-reciprocal range that is more robust to disturbance and desirable for real world applications.

7.3.4 Disorder effects

In Chapter 3, we observed that heterogeneity plays an important role in terms of expanding the number of distinct mechanical properties of the assembled metastructure. However, it’s well known that vibration and wave transmission within a linear periodic structure can be significantly influenced in the presence of disorder, known as Anderson localization [111] [112] [113] [114] [115] [116]. Therefore, in the disordered metastable metastructure, there potentially exhibits two competing factors for vibration and wave transmission. On one hand, aperiodicity tend to generate localized mode that prevents energy transmission. On the other hand, nonlinearity induces supratransmission that can enable bandgap transmission. Hence, it remains unexplored on how the two factors interact with each other for various excitation conditions.

Bibliography

[1] G. Tortora and B. Derrickson, Principles of anatomy and physiology, New York: John Wiley & Sons, Inc, 2006.

[2] M. Caruel, J. M. Allain and L. Truskinovsky, "Muscle as a metamaterial operating near a critical point," *Physical Review Letter,* vol. 110, no. 24, p. 248103, 2013.

[3] M. J. Buehler and T. Ackbarow, "Nanomechanical strength mechanisms of hierarchical biological materials and tissues," *Computer Methods in Biomechanics and Biomedical Engineering,* vol. 11, no. 6, pp. 595-607, 2008.

[4] L. Truskinovsky and A. Vainchtein, "Kinetics of martensitic phase transitions: Lattice model," *SIAM Journal on Applied Mathematics,* vol. 66, no. 2, pp. 533-553, 2005.

[5] H. N. Wadley, "Multifunctional periodic cellular metals," *Philosophical Transactions of the Royal Society A: Mathematical, Physical and Engineering Sciences,* vol. 364, no. 1838, pp. 31-68, 2006.

[6] N. Fleck, V. Deshpande and M. Ashby, "Micro-architectured materials: Past, present and future," *Proceedings of the Royal Society of London A:Mathematical, Physical and Engineering Sciences,* vol. 466, no. 2121, pp. 2495-2516, 2010.

[7] L. Gibson and M. Ashby, Cellular solids: Structure and properties, Cambridge university press, 1999.

[8] P. Deymier, Acoustic metamaterials and phononic crystals, ser. Springer Series in Solid-State Sciences., Springer, 2013.

[9] J. Vasseur, O. Matar, J. Robillard, A.-C. Hladky-Hennion and P. Deymier, "Band structures tunability of bulk 2d phononic crystals made of magneto-elastic materials," *AIP Advances,* vol. 1, no. 4, p. 041904, 2011.

[10] G. Greaves, A. Greer, R. Lakes and T. Rouxel, "Poisson's ratio and modern materials," *Nature Materials,* vol. 10, pp. 823-837, 2011.

[11] D. Wagg, I. Bond, P. Weaver and M. Friswell, Adaptive structures: Engineering applications, Chichester: John Wiley and Sons, Inc., 2007.

[12] J. Shim, S. Shan, A. Košmrlj, S. Kang, E. Chen, J. Weaver and K. Bertoldi, "Harnessing instabilities for design of soft reconfigurable auxetic/chiral materials," *Soft Matter,* vol. 9, pp. 8198-8202, 2013.

[13] M. Schenk and S. Guest, "Geometry of Miura-folded metamaterials," *Proceedings of the National Academy of Sciences,* vol. 110, pp. 3276-3281, 2013.

[14] R. Lakes, T. Lee, A. Bersie and Y. Wang, " Extreme damping in composite materials with negative-stiffness inclusions," *Nature,* vol. 410, pp. 565-567, 2001.

[15] Z. Nicolaou and A. Motter, "Mechanical metamaterials with negative compressibility transitions," *Nature Materials,* vol. 11, pp. 608-613, 2012.

[16] C. A. Steeves, S. L. d. S. e. Lucato, M. He, E. Antinucci, J. W. Hutchinson and A. G. Evans, "Concepts for structurally robust materials that combine low thermal expansion with high stiffness," *Journal of the Mechanics and Physics of Solids,* vol. 55, no. 9, pp. 1803-1822, 2007.

[17] K. R. Olympio and F. Gandhi, "Flexible skins for morphing aircraft using cellular honeycomb cores," *Journal of Intelligent Material Systems and Structures,* vol. 21, pp. 1719-1735, 2010.

[18] A. A. Zadpoor, "Mechanical meta-materials," *Materials Horizons,* vol. 3, pp. 371-381, 2016.

[19] I. Kuder, A. Arrieta, W. Rathier and P. Ermanni, "Variable stiffness material and structural concepts for morphing applications," *Progress in Aerospace Sciences,* vol. 63, pp. 33-55, 2013.

[20] M. Kadic, T. Bückmann, R. Schittny and M. Wegener, "Metamaterials beyond electromagnetism," *Reports on Progress in Physics* , vol. 76, p. 126501, 2013.

[21] L. Brillouin, Wave propagation in periodic structures, Dover Publications, 1953.

[22] B. J. Olson, S. W. Shaw, C. Shi, C. Pierre and R. G. Parker, "Circulant matrices and their application to vibration analysis," *Applied Mechanics Reviews,* vol. 66, no. 4, p. 040803, 2014.

[23] G. Memoli, M. Caleap, M. Asakawa, D. R. Sahoo, B. W. Drinkwater and S. Subramanian, "Metamaterial bricks and quantization of meta-surfaces," *Nature Communication,* vol. 8, p. 14608, 2016.

[24] M. Carrara, M. R. Cacan, M. J. Leamy, M. Ruzzene and A. Erturk, "Dramatic enhancement of structure-borne wave energy harvesting using an elliptical acoustic mirror," *Applied Physics Letters,* vol. 100, p. 204105, 2012.

[25] A. N. Norris, "Acoustic cloaking," *Acoustics Today,* vol. 11, no. 1, pp. 38-46, 2015.

[26] M. I. Hussein, M. J. Leamy and M. Ruzzene, "Dynamics of phononic materials and structures: Historical origins, recent progress, and future outlook," *Applied Mechanics Reviews,* vol. 66, no. 4, p. 040802, 2014.

[27] Y. Pennec, J. O. Vasseur, B. Djafari-Rouhani, L. Dobrzynski and P. A. Deymier, "Two-dimensional phononic crystals: Examples and applications," *Surface Science Reports,* vol. 65, no. 8, pp. 229-291, 2010.

[28] S. A. Cummer, J. Christensen and A. Alu, "Controlling sound with acoustic metamaterials," *Nature Reviews Materials,* vol. 1, p. 16001, 2016.

[29] G. Ma and P. Sheng, "Acoustic metamaterials: From local resonances to broad horizons," *Science Advances,* vol. 2, p. e1501595, 2016.

[30] C. Goffaux and J. P. Vigneron, "Theoretical study of a tunable phononic band gap system," *Physical Review B,* vol. 64, p. 075118, 2001.

[31] P. Wang, F. Casadei, S. Shan, J. C. Weaver and K. Bertoldi, "Harnessing buckling to design tunable locally resonant acoustic metamaterials," *Physical Review Letters,* vol. 113, p. 014301, 2014.

[32] J.-Y. Yeh, "Control analysis of the tunable phononic crystal with electrorheological material," *Physica B: Condensed Matter,* vol. 400, pp. 137-144, 2007.

[33] J.-F. Robillard, O. B. Matar, J. O. Vasseur, P. A. Deymier, M. Stippinger, A.-C. Hladky-Hennion, Y. Pennec and B. Djafari-Rouhani, "Tunable magnetoelastic phononic crystals," *Applied Physics Letters,* vol. 95, p. 124104, 2009.

[34] J. P. Turpin, J. A. Bossard, K. L. Morgan, D. H. Werner and P. L. Werner, "Reconfigurable and tunable metamaterials: A review of the theory and applications," *International Journal of Antennas and Propagation,* vol. 2014, p. 429837, 2014.

[35] C. Rizza, A. Ciattoni, F. Paulis, E. Palange, A. Orlandi, L. Columbo and F. Prati, "Reconfigurable photoinduced metamaterials in the microwave regime," *Journal of Physics D: Applied Physics,* vol. 48, p. 135103, 2015.

[36] A. D. Boardman, V. V. Grimalsky, Y. S. Kivshar, S. V. Koshevaya, M. Lapine, N. M. Litchinitser, V. N. Malnev, M. Noginov, Y. G. Rapoport and V. M. Shalaev, "Active and tunable metamaterials," *Laser & Photonics Reviews,* vol. 5, pp. 287-307, 2010.

[37] N. I. Zheludev and E. Plum, "Reconfigurable nanomechanical photonic metamaterials," *Nature Nanotechnology,* vol. 11, pp. 16-22, 2016.

[38] H.-T. Chen, A. Taylor and N. Yu, "A review of metasurfaces: Physics and applications," *Reports on Progress in Physics,* vol. 79, p. 076401, 2016.

[39] S. Walia, C. M. Shah, P. Gutruf, H. Nili, D. R. Chowdhury, W. Withayachumnankul, M. Bhaskaran and S. Sriram, "Flexible metasurfaces and metamaterials: A review of materials and fabrication processes at micro- and nano-scales," *Applied Physics Reviews,* vol. 2, p. 011303, 2015.

[40] F. Dai, H. Li and S. Du, "A multi-stable lattice structures and its snap-through behavior among multiple states," *Composite Structures,* vol. 97, pp. 56-63, 2013.

[41] S. Daynes, R. Trask and P. Weaver, "Bio-inspired structural bistability employing elastomeric origami for morphing applications," *Smart Materials and Structures,* vol. 23, p. 125011, 2014.

[42] L. Bowen, K. Springsteen, H. Feldstein, M. Frecker, T. Simpson and P. von Lockette, "Development and validation of a dynamic model of magneto-active elastomer actuation of the origami waterbomb base," *Journal of Mechanisms and Robots,* vol. 7, p. 011010, 2015.

[43] S. Li and K. Wang, "Fluidic origami: A plant-inspired adaptive structure with shape morphing and stiffness tuning," *Smart Materials and Structures,* vol. 24, p. 105031, 2015.

[44] M. Schaeffer and M. Ruzzene, "Wave propagation in multistable magneto-elastic lattices," *International Journal of Solids and Structures,* Vols. 56-57, pp. 78-95, 2015.

[45] B. Haghpanah, L. Salari-Sharif, P. Pourrajab, J. Hopkins and L. Valdevit, "Multistable shape-reconfigurable architected materials," *Advanced Materials,* vol. 28, pp. 7915-7920, 2016.

[46] A. Rafsanjani, A. Akbarzadeh and D. Pasini, "Snapping mechanical metamaterials under tension," *Advanced Materials,* vol. 27, pp. 5931-5935, 2015.

[47] K. Bertoldi, V. Vitelli, J. Christensen and M. v. Hecke, "Flexible mechanical metamaterials," *Nature Reviews Materials,* vol. 2, p. 17066, 2017.

[48] K. Bertoldi, "Harnessing instabilities to design tunable architected cellular materials," *Annual Review of Materials Research,* vol. 47, pp. 51-61, 2017.

[49] D. M. Kochmann and K. Bertoldi, "Exploiting microstructural instabilities in solids and structures: From metamaterials to structural transitions," *Applied Mechanics Reviews,* vol. 5, p. 05081, 2017.

[50] R. L. Harne and K. W. Wang, "A review of the recent research on vibration energy harvesting via bistable systems," *Smart Materials and Structures,* vol. 22, p. 023001, 2013.

[51] M. Remoissenet, Waves called solitons: Concepts and experiments, Springer Science & Business Media, Germany, 2003.

[52] T. Dauxois and M. Peyrard, Physics of solitons, Cambridge University Press, U.K., 2006.

[53] G. Whitham, Linear and nonlinear waves, John Wiley & Sons, 1976.

[54] B.-F. Feng and T. Kawahara, "Discrete breathers in two-dimensional nonlinear lattices," *Wave Motion,* vol. 45, pp. 68-82, 2007.

[55] M. Sato, B. E. Hubbard and A. J. Sievers, "Colloquium: Nonlinear energy localization and its manipulation in micromechanical oscillator arrays," *Reviews of Modern Physics,* vol. 78, pp. 137-157, 2006.

[56] J. Page, "Asymptotic solutions for localized vibrational modes in strongly anharmonic periodic systems," *Physical Review B,* vol. 41, p. 7835, 1990.

[57] T. Rössler and J. B. Page, "Optical creation of vibrational intrinsic localized modes in anharmonic lattices with realistic interatomic potentials," *Physical Review B,* vol. 62, p. 11460, 2000.

[58] R. F. Wallis, D. L. Mills and A. D. Boardman, "Intrinsic localized spin modes in ferromagnetic chains with on-site anisotropy," *Physical Review B,* vol. 52, p. R3828(R), 1995.

[59] R. Lai and A. J. Sievers, "Nonlinear nanoscale localization of magnetic excitations in atomic lattices," *Physics Reports,* vol. 314, pp. 147-236, 1999.

[60] W. Z. Wang, A. R. Bishop, J. T. Gammel and R. N. Silver, "Quantum breathers in electron-phonon systems," *Physical Review Letters,* vol. 80, pp. 3284-3287, 1998.

[61] H. Fehske, J. Loos and G. Wellein, "Lattice polaron formation: Effects of nonscreened electron-phonon interaction," *Physical Review B,* vol. 61, p. 8016, 2000.

[62] O. Bang and P. D. Miller, "Exploiting discreteness for switching in waveguide arrays," *Optics Letters,* vol. 21, pp. 1105-1107, 1996.

[63] A. R. McGurn and R. M. Fitzgerald, "Enhancement of phase-coherent electromagnetic scattering from a random array of identical resonant dielectric ridges placed upon a dielectric substrate," *Physical Review B,* vol. 65, p. 155414, 2002.

[64] A. Dick, B. Balachandran and C. Mote, "Intrinsic localized modes in microresonator arrays and their relationship to nonlinear vibration modes," *Nonlinear Dynamics,* vol. 54, pp. 13-29, 2008.

[65] M. Sato, B. E. Hubbard, L. Q. English, A. J. Sievers, B. Ilic, D. A. Czaplewski and H. G. Craighead, "Study of intrinsic localized vibrational modes in micromechanical oscillator arrays," *Chaos,* vol. 13, pp. 702-715, 2003.

[66] S. Flach and A. V. Gorbach, "Discrete breathers - advances in theory and applications," *Physics Reports,* vol. 467, pp. 1-116, 2008.

[67] D. Hennig and G. Tsironis, "Wave transmission in nonlinear lattices," *Physics Reports,* vol. 307, pp. 333-432, 1999.

[68] M. A. Porter, P. G. Kevrekidis and C. Daraio, "Granular crystals: Nonlinear dynamics meets materials engineering," *Physics Today,* vol. 68, pp. 44-50, 2015.

[69] V. F. Nesterenko, A. N. Lazaridi and E. B. Sibiryakov, "The decay of soliton at the contact of two “acoustic vacuums”," *Journal of Applied Mechanics and Technical Physics,* vol. 36, pp. 166-168, 1995.

[70] R. S. Sinkovits and S. Sen, "Nonlinear dynamics in granular columns," *Physical Review Letters,* vol. 74, p. 2686, 1995.

[71] C. Coste, E. Falcon and S. Fauve, "Solitary waves in a chain of beads under Hertz contact," *Physical Review E,* vol. 56, pp. 6104-6117, 1997.

[72] S. Sen, M. Manciu and J. D. Wright, "Solitonlike pulses in perturbed and driven Hertzian chains and their possible applications in detecting buried impurities," *Physical Review E,* vol. 57, p. 2386, 1998.

[73] C. Daraio, V. F. Nesterenko, E. B. Herbold and S. Jin, "Energy trapping and shock disintegration in a composite granular medium," *Physical Review Letter,* vol. 96, p. 058002, 2006.

[74] S. Job, F. Santibanez, F. Tapia and F. Melo, "Nonlinear waves in dry and wet Hertzian granular chains," *Ultrasonics,* vol. 48, pp. 506-514, 2008.

[75] E. Herbold, J. Kim, V. F. Nesterenko, S. Y. Wang and C. Daraio, "Pulse propagation in a linear and nonlinear diatomic periodic chain: effects of acoustic frequency band-gap," *Acta Mechanica,* vol. 205, pp. 85-103, 2009.

[76] C. Daraio, D. Ngo, V. F. Nesterenko and F. Fraternali, "Highly nonlinear pulse splitting and recombination in a two-dimensional granular network," *Physical Review E,* vol. 82, p. 036603, 2010.

[77] A. M. Tichler, L. R. Gómez, N. Upadhyaya, X. Campman, V. F. Nesterenko and V. Vitelli, "Transmission and reflection of strongly nonlinear solitary waves at granular interfaces," *Physical Review Letters,* vol. 111, p. 048001, 2013.

[78] R. Ganesh and S. Gonella, "Spectro-spatial wave features as detectors and classifiers of nonlinearity in periodic chains," *Wave Motion,* vol. 50, pp. 821-835, 2013.

[79] W.-S. Duan, Z.-B. Zhang and L. Yang, "Shock wave in a one-dimensional granular chain under Hertz contact," *Physical Review E,* vol. 94, p. 052906, 2016.

[80] M. A. Hasan and S. Nemat-Nasser, "Universal relations for solitary waves in granular crystals under shocks with finite rise and decay times," *Physical Review E,* vol. 93, p. 042905, 2016.

[81] G. Chakraborty and A. Mallik, "Dynamics of a weakly non-linear periodic chain," *International Journal of Non-Linear Mechanics,* vol. 36, pp. 375-389, 2001.

[82] A. F. Vakakis and M. E. King, "Nonlinear wave transmission in a monocoupled elastic periodic system," *The Journal of the Acoustical Society of America*, vol. 98, pp. 1534-1546, 1995.

[83] R. K. Narisetti, M. J. Leamy and M. Ruzzene, " A perturbation approach for predicting wave propagation in one-dimensional nonlinear periodic structures," *Journal of Vibration and Acoustics,* vol. 132, p. 031001, 2010.

[84] R. K. Narisetti, M. Ruzzene and M. Leamy, "A perturbation approach for analyzing dispersion and group velocities in two-dimensional nonlinear periodic lattices," *Journal of Vibration and Acoustics,* vol. 133, p. 061120, 2011.

[85] B. Lazarov and J. Jensen, "Low-frequency band gaps in chains with attached non-linear oscillators," *International Journal of Non-Linear Mechanics,* vol. 42, pp. 1186-1193, 2007.

[86] J. M. Manimala and C. T. Sun, "Numerical investigation of amplitude-dependent dynamic response in acoustic metamaterials with nonlinear oscillators," *The Journal of the Acoustical Society of America,* vol. 139, pp. 3365-3372, 2016.

[87] T. Yang, Z.-G. Song, E. Clerkin, Y.-W. Zhang, J.-H. Sun, Y.-S. Su, L.-Q. Chen and P. Hagedorn, "A programmable nonlinear acoustic metamaterial," *AIP Advances,* vol. 7, p. 095323, 2017.

[88] J. Lydon, G. Theocharis and C. Daraio, "Nonlinear resonances and energy transfer in finite granular chains," *Physical Review E,* vol. 91, p. 023208, 2015.

[89] P. Maniadis, G. Kopidakis and S. Aubry, "Energy dissipation threshold and self-induced transparency in systems with discrete breathers," *Physica D: Nonlinear Phenomena,* vol. 216, pp. 121-135, 2006.

[90] H. Susanto, "Boundary driven waveguide arrays: Supratransmission and saddle-node bifurcation," *SIAM Journal on Applied Mathematics,* vol. 69, p. 111–125, 2008.

[91] K. Oh and A. H. Nayfeh, "Nonlinear combination resonances in cantilever composite plates," *Nonlinear Dynamics ,* vol. 11, pp. 143-169, 1996.

[92] A. H. Nayfeh and D. T. Mook, Nonlinear oscillations, John Wiley & Sons, 2008.

[93] A. Marchionne and P. Ditlevsen, "Three types of nonlinear resonances," *arXiv:1605.00858 [math.DS]*.

[94] F. Geniet and J. Leon, "Energy transmission in the forbidden band gap of a nonlinear chain," *Physical Review Letters,* vol. 89, p. 134102, 2002.

[95] J. Leon, "Nonlinear supratransision as a fundamental instability," *Physics Letters A,* vol. 319, pp. 130-136, 2003.

[96] J. E. Macías-Díaz, "Numerical study of the transmission of energy in discrete arrays of sine-Gordon equations," *Physical Review E,* vol. 77, p. 016602, 2008.

[97] J. Macías-Díaz and A. Puri, "On the propagation of binary signals in damped mechanical systems of oscillators," *Physica D: Nonlinear Phenomena,* vol. 228, pp. 112-121, 2007.

[98] P. Anghel-Vasilescu, J. Dorignac, F. Geniet, J. Leon and M. Taki, "Nonlinear supratransmission in multicomponent systems," *Physical Review Letters,* vol. 105, p. 074101, 2010.

[99] D. Chevriaux, R. Khomeriki and J. Leon, "Theory of a Josephson junction parallel array detector sensitive to very weak signals," *Physical Review B,* vol. 73, p. 214516, 2006.

[100] R. Khomeriki, S. Lepri and S. Ruffo, "Pattern formation and localization in the forced-damped Fermi-Pasta-Ulam lattice," *Physical Review E,* vol. 64, p. 056606, 2001.

[101] R. Khomeriki, S. Lepri and S. Ruffo, "Nonlinear supratransmission and bistability in the Fermi-Pasta-Ulam model," *Physical Review E,* vol. 70, p. 066626, 2004.

[102] N. Boechler, G. Theocharis and C. Daraio, "Bifurcation-based acoustic switching and rectification," *Nature Materials,* vol. 10, pp. 665-668, 2011.

[103] C. Hoogeboom, Y. Man, N. Boechler, G. Theocharis, P. G. Kevrekidis, I. G. Kevrekidis and C. Daraio, "Hysteresis loops and multi-stability: From periodic orbits to chaotic dynamics (and back) in diatomic granular crystals," *Europhysics Letters,* vol. 101, p. 44003, 2013.

[104] B. Yousefzadeh and A. S. P. Phani, "Supratransmission in a disordered nonlinear periodic structure," *Journal of Sound and Vibration,* vol. 380, pp. 242-266, 2016.

[105] M. J. Frazier and D. M. Kochmann, "Band gap transmission in periodic bistable mechanical," *Journal of Sound and Vibration,* vol. 388, pp. 315-326, 2017.

[106] H. Cho, B. Jeong, M.-F. Yu, A. F. Vakakis, D. M. McFarland and L. A. Bergman, "Nonlinear hardening and softening resonances in micromechanical cantilever-nanotube systems originated from nanoscale geometric nonlinearities," *International Journal of Solids and Structures,* vol. 49, pp. 2059-2065, 2012.

[107] V. Rothos and A. Vakakis, "Dynamic interactions of traveling waves propagating in a linear chain with an local essentially nonlinear attachment," *Wave Motion,* vol. 46, pp. 174-188, 2009.

[108] A. Vakakis, M. AL-Shudeifat and M. Hasan, "Interactions of propagating waves in a one-dimensional chain of linear oscillators with a strongly nonlinear local attachment," *Meccanica,* vol. 49, pp. 2375-2397, 2014.

[109] X. Fang, J. Wen, J. Yin and D. Yu, "Wave propagation in nonlinear metamaterial multi-atomic chains based on homotopy method," *AIP Advances,* vol. 6, p. 121706, 2016.

[110] A. J. Martínez, H. Yasuda, E. Kim, P. G. Kevrekidis, M. A. Porter and J. Yang, "Scattering of waves by impurities in precompressed granular chains," *Physical Review E,* vol. 93, p. 052224, 2016.

[111] P. W. Anderson, "Absence of diffusion in certain random lattices," *Physical Review,* vol. 109, pp. 1492-1958, 1958.

[112] C. Hodges, "Confinement of vibration by structural irregularity," *Journal of Sound and Vibration,* vol. 82, pp. 411-424, 1982.

[113] C. Pierre, "Weak and strong vibration localization in disordered structures: A statistical investigation," *Journal of Sound and Vibration,* vol. 139, pp. 111-132, 1990.

[114] M. P. Castanier and C. Pierre, "Individual and interactive mechanisms for localization and dissipation in a mono-coupled nearly-periodic structure," *Journal of Sound and Vibration,* vol. 168, pp. 479-505, 1993.

[115] S. Tietsche and A. Pikovsky, "Chaotic destruction of Anderson localization in a nonlinear lattice," *Europhysics Letters,* vol. 48, p. 10006, 2008.

[116] A. Lagendijk, B. v. Tiggelen and D. S. Wiersma, "Fifty years of Anderson localization," *Physics Today,* vol. 62, pp. 24-29, 2009.

[117] S. Barbarino, O. Bilgen, R. Ajaj, M. Friswell and D. Inman, "A review of morphing aircraft," *Journal of Intelligent Material Systems and Structures,* vol. 22, pp. 823-877, 2011.

[118] G. McKnight, R. Doty, A. Keefe, G. Herrera and C. Henry, "Segmented reinforcement variable stiffness materials for reconfigurable surfaces," *Journal of Intelligent Material Systems and Structures,* vol. 21, pp. 1783-1793, November 2010.

[119] W. S. Oates, H. Wang and R. L. Sierakowski, "Unusual field-coupled nonlinear continuum mechanics of smart materials," *Journal of Intelligent Material Systems and Structures,* vol. 23, pp. 487-504, 2012.

[120] J. Gomez and E. Garcia, "Morphing unmanned aerial vehicles," *Smart Materials and Structures,* vol. 20, p. 103001, 2011.

[121] Y. Liu, H. Du, L. Liu and J. Leng, "Shape memory polymers and their composites in aerospace applications: A review," *Smart Materials and Structures,* vol. 23, p. 023001, 2014.

[122] S. Daynes, A. Grisdale, A. Seddon and R. Trask, "Morphing structures using soft polymers for active deployment," *Smart Materials and Structures,* vol. 23, p. 012001, 2014.

[123] E. A. Peraza-Hernandez, D. J. Hartl, R. J. Malak Jr and D. C. Lagoudas, "Origami-inspired active structures: A synthesis and review," *Smart Materials and Structures,* vol. 23, p. 094001, 2014.

[124] S. Barbarino, E. I. S. Flores, R. M. Ajaj, I. Dayyani and M. I. Friswell, "A review on shape memory alloys with applications to morphing aircraft," *Smart Materials and Structures,* vol. 23, p. 063001, 2014.

[125] B. Li, L. Wang and G. Casati, "Thermal diode: Rectification of heat flux," *Physical Review Letters,* p. 18430193, 2004.

[126] B. Hu, L. Yang and Y. Zhang, "Asymmetric heat conduction in nonlinear lattices," *Physical Review Letters,* vol. 97, p. 124302, 2006.

[127] W. Kobayashi, Y. Teraoka and I. Terasaki, "An oxide thermal rectifier," *Applied Physics Letters,* vol. 95, p. 171905, 2009.

[128] M. Maldovan, "Sound and heat revolutions in phononics," *Nature,* vol. 503, pp. 209-217, 2013.

[129] B. Liang, X. S. Guo, J. Tu, D. Zhang and J. C. Cheng, "An acoustic rectifier," *Nature Materials,* vol. 9, pp. 989-992, 2010.

[130] M. Tocci, M. Bloemer, M. Scalora, J. P. Dowling and C. M. Bowden, "Thin-film nonlinear optical diode," *Applied Physics Letters,* vol. 66, p. 2324, 1995.

[131] J. Y. Chin, T. Steinle, T. Wehlus, D. Dregely, T. Weiss, V. I. Belotelov, B. Stritzker and H. Giessen, "Nonreciprocal plasmonics enables giant enhancement of thin-film Faraday rotation," *Nature Communications,* vol. 4, p. 1599, 2013.

[132] R. Fleury, D. L. Sounas, C. F. Sieck, M. R. Haberman and A. Alù, "Sound isolation and giant linear nonreciprocity in a compact acoustic circulator," *Science,* vol. 343, pp. 516-519, 2014.

[133] N. Swinteck, S. Matsuo, K. Runge, J. O. Vasseur, P. Lucas and P. A. Deymier, "Bulk elastic waves with unidirectional backscattering-immune topological states in a time-dependent superlattice," *Journal of Applied Physics,* vol. 118, p. 063103, 2015.

[134] D.-W. Wang, H.-T. Zhou, M.-J. Guo, J.-X. Zhang, J. Evers and S.-Y. Zhu, "Optical diode made from a moving photonic crystal," *Physical Review Letters,* vol. 110, p. 093901, 2013.

[135] B. I. Popa and S. A. Cummer, "Non-reciprocal and highly nonlinear active acoustic metamaterials," *Nature Communications,* vol. 5, p. 3398, 2014.

[136] N. Nadkarni, A. F. Arrieta, C. Chong, D. M. Kochmann and C. Daraio, "Unidirectional transition waves in bistable lattices," *Physical Review Letters,* vol. 116, p. 244501, 2016.

[137] N. Nadkarni, C. Daraio and D. M. Kochmann, "Dynamics of periodic mechanical structures containing bistable elastic elements: From elastic to solitary wave propagation," *Physical Review E,* vol. 90, p. 023204, 2014.

[138] R. L. Harne and K. W. Wang, Harnessing bistable structural dynamics: For vibration control, energy harvesting, and sensing, John Wiley and Sons, ISBN: 978-1-119-12804-5, 408 pages, 2017.

[139] R. Fleury, D. Sounas, M. R. Haberman and A. Alù, "Nonreciprocal acoustics," *Acoustics Today,* vol. 11, pp. 14-21, 2015.

[140] Z.-G. Chen and Y. Wu, "Tunable topological phononic crystals," *Physical Review Applied,* vol. 5, p. 054021, 2016.

[141] J. R. Raney, N. Nadkarni, C. Daraio, D. M. Kochmann, J. A. Lewis and K. Bertoldi, "Stable propagation of mechanical signals in soft media using stored elastic energy," *Proceedings of the National Academy of Sciences,* vol. 113, pp. 9722-9727, 2016.

[142] L. Marcucci and L. Truskinovsky, "Mechanics of the power stroke in myosin II," *Physical Review E,* vol. 81, p. 051915, 2010.

[143] M. Caruel, J. Allain and L. Truskinovsky, "Mechanics of collective unfolding," *Journal of the Mechanics and Physics of Solids,* vol. 76, pp. 237-259, 2015.

[144] I. Kovacic and M. J. Brennan, The Duffing equation: Nonlinear oscillators and their behaviour, I. Kovacic and M. Brennan, Eds., Chichester: John Wiley & Sons, 2011.

[145] A. Allahverdyan and Q. Wang, "Adaptive machine and its thermodynamic costs," *Physical Review E,* vol. 87, p. 032139, 2013.

[146] D. Holmes and A. Crosby, "Snapping surfaces," *Advanced Materials,* vol. 19, pp. 3589-3593, 2007.

[147] G. Lan, P. Sartori, S. Neumann, V. Sourjik and Y. Tu, "The energy-speed-accuracy trade-off in sensory adaptation," *Nature Physics,* vol. 8, pp. 422-428, 2012.

[148] R. Lakes, T. Lee, A. Bersie and Y. Wang, "Extreme damping in composite materials with negative-stiffness inclusions," *Nature,* vol. 410, pp. 565-567, 2001.

[149] T. Klatt and M. Haberman, "A nonlinear negative stiffness metamaterial unit cell and small-on-large multiscale material model," *Journal of Applied Physics,* vol. 114, p. 033503, 2013.

[150] D. Holmes, B. Tavakol, G. Froehlicher and H. Stone, "Control and manipulation of microfluidic flow via elastic deformations," *Soft Matter,* vol. 9, pp. 7049-7053, 2013.

[151] R. Lakes and W. Drugan, "Dramatically stiffer elastic composite materials due to a negative stiffness phase?," *Journal of the Mechanics and Physics of Solids,* vol. 50, pp. 979-1009, 2002.

[152] G. Puglisi and L. Truskinovsky, "Mechanics of a discrete chain with bi-stable elements," *Journal of the Mechanics and Physics of Solids,* vol. 48, pp. 1-27, 2000.

[153] Y. Shan, M. Philen, A. Lotfi, S. Li, C. Bakis, C. Rahn and K. Wang, "Variable stiffness structures utilizing fluidic flexible matrix composites," *Journal of Intelligent Material Systems and Structures,* vol. 20, pp. 443-456, 2009.

[154] K. Virk, A. Monti, T. Trehard, M. Marsh, K. Hazra, K. Boba, C. Remillat, F. Scarpa and I. Farrow, "SILICOMB PEEK Kirigami cellular structures: mechanical response and energy dissipation through zero and negative stiffness," *Smart Materials and Structures,* vol. 22, p. 084014, 2013.

[155] J. Valasek, Morphing aerospace vehicles and structures, Chichester: John Wiley & Sons, 2012.

[156] M. Philen, "On the applicability of fluidic flexible matrix composite variable impedance materials for prosthetic and orthotic devices," *Smart Materials and Structures,* vol. 18, p. 104023, 2009.

[157] F. Fritzen and D. Kochmann, "Material instability-induced extreme damping in composites: a computational study," *International Journal of Solids and Structures,* vol. 51, pp. 4101-4112, 2014.

[158] M. Schenk and S. Guest, "On zero stiffness," *Proceedings of the Institution of Mechanical Engineers, Part C: Journal of Mechanical Engineering Science,* vol. 228, pp. 1701-1714, 2014.

[159] G. Puglisi and L. Truskinovsky, "A mechanism of transformational plasticity," *Continuum Mechanics and Thermodynamics,* vol. 14, pp. 437-457, 2002.

[160] G. Holst, G. Teichert and B. Jensen, "Modeling and experiments of buckling modes and deflection of fixed-guided beams in compliant mechanisms," *Journal of Mechanical Design,* vol. 133, p. 051002, 2011.

[161] Y. Chen and C. Lan, "An adjustable constant-force mechanism for adaptive end-effector operations," *Journal of Mechanical Design,* vol. 134, p. 031005, 2012.

[162] N. Kidambi, R. Harne and K. Wang, "Adaptation of energy dissipation in a mechanical metastable module excited near resonance," *Journal of Vibration and Acoustics,* vol. 138, p. 011001, 2015.

[163] F. Romeo, G. Sigalov, L. Bergman and A. Vakakis, "Dynamics of a linear oscillator coupled to a bistable light attachment: numerical study," *Journal of Computational and Nonlinear Dynamics,* vol. 10, p. 011007, 2015.

[164] N. Biggs, "The roots of combinatorics," *Historia Mathematica,* vol. 6, pp. 109-136, 1979.

[165] B. Florijn, C. Coulais and M. van Hecke, "Programmable mechanical metamaterials," *Physical Review Letters,* vol. 113, p. 175503, 2014.

[166] I. Antoniadis, D. Chronopoulos, V. Spitas and D. Koulocheris, "Hyper-damping peroperties of a stiff and stable linear oscillator with a negative stiffness element," *Journal of Sound and Vibration,* vol. 346, pp. 37-52, 2015.

[167] R. Haupt and S. Haupt, Practical genetic algorithms, Hoboken: Wiley, 1998.

[168] R. Freund, W. Wilson and D. Mohr, Statistical methods, Burlington: Academic Press, 2010.

[169] C. Tipton, E. Han and T. Mullin, "Magneto-elastic buckling of a soft cellular solid," *Soft Matter,* vol. 8, pp. 6880-6883, 2012.

[170] S. Shan, S. Kang, J. Raney, P. Wang, L. Fang, F. Candido, J. Lewis and K. Bertoldi, "Multistable architected materials for trapping elastic strain energy," *Advanced Materials,* vol. 27, pp. 4296-4301, 2015.

[171] N. Kryloff and N. Bogoliuboff, Introduction to non-linear mechanics, New Jersey: Princeton University Press, 1950.

[172] M. Urabe, "Galerkin's procedure for nonlinear periodic systems," *Archive for Rational Mechanics and Analysis,* vol. 20, pp. 120-152, 1965.

[173] K. Sze, S. Chen and J. Huang, "The incremental harmonic balance method for nonlinear vibration of axially moving beams," *Journal of Sound and Vibration,* vol. 281, pp. 611-626, 2005.

[174] V. Jaumouillé, J.-J. Sinou and B. Petitjean, "An adaptive harmonic balance method for predicting the nonlinear dynamic responses of mechanical systems - application to bolted structures," *Journal of Sound and Vibration,* vol. 329, pp. 4048-4067, 2010.

[175] G. v. Groll and D. Ewins, "The harmonic balance method with arc-length continuation in rotor/stator contact problems," *Journal of Sound and Vibration,* vol. 241, pp. 223-233, 2001.

[176] K. Kundert and A. Sangiovanni-Vincentell, "Simulation of nonlinear circuits in the frequency domain," *IEEE Transactions on Computer-Aided Design of Integrated Circuits and Systems,* vol. 5, pp. 521-535, 1986.

[177] R. Genesio and A. Tesi, "Harmonic balance methods for the analysis of chaotic dynamics in nonlinear systems," *Automatica,* vol. 28, pp. 531-548, 1992.

[178] S. C. Stanton, B. A. Owens and B. P. Mann, "Harmonic balance analysis of the bistable piezoelectric inertial generator," *Journal of Sound and Vibration,* vol. 331, pp. 3617-3627, 2012.

[179] C.-C. Fang, "Critical conditions for a class of switched linear systems based on harmonic balance: applications to DC-DC converters," *Nonlinear Dynamics,* vol. 70, pp. 1767-1789, 2012.

[180] S. Shen, "An approximate analysis of nonlinear flutter problems," *Journal of Aeronautical Sciences* , vol. 26, no. 1, pp. 25-32, 2003.

[181] L. Liu and E. H. Dowell, "Harmonic balance approach for an airfoil with a freeplay control surface," *AIAA Journal,* vol. 4, pp. 802-815, 2005.

[182] B. Lee, L. Liu and K. Chung, "Airfoil motion in subsonic flow with strong cubic nonlinear restoring forces," *Journal of Sound and Vibration,* vol. 281, pp. 699-717, 2005.

[183] G. Dimitriadis, "Continuation of higher-order harmonic balance solutions for nonlinear aeroelastic systems," *Journal of Aircraft,* vol. 45, pp. 523-537, 2008.

[184] K. C. Hall, J. P. Thomas and W. S. Clark, "Computation of unsteady nonlinear flows in cascades using a harmonic balance technique," *AIAA Journal,* vol. 40, pp. 879-886, 2002.

[185] S. T. Clark, F. M. Besem, R. E. Kielb and J. P. Thomas, "Developing a reduced-order model of nonsynchronous vibration in turbomachinery using proper-orthogonal decomposition methods," *Journal of Engineering for Gas Turbines and Powe,* vol. 137, p. 052501, 2015.

[186] K. Ekici, K. C. Hall and E. H. Dowell, "Computationally fast harmonic balance methods for unsteady aerodynamic predictions of helicopter rotors," *Journal of Computational Physics,* vol. 227, pp. 6206-6225, 2008.

[187] E. P. Petrov and D. J. Ewins, "Analytical formulation of friction interface elements for analysis of nonlinear multi-harmonic vibrations of bladed disks," *Journal of Turbomachinery,* vol. 125, pp. 364-371, 2003.

[188] S. Peter, P. Reuss and L. Gaul, "Identification of sub- and higher harmonic vibrations in vibro-impact systems," *Nonlinear Dynamics,* vol. 2, pp. 131-140, 2014.

[189] W.-Y. Tseng and J. Dugundji, "Nonlinear vibrations of a buckled beam under harmonic excitation," *Journal of Applied Mechanics,* vol. 38, pp. 467-476, 1971.

[190] W. Szemplińska-Stupnicka and J. Rudowsk, "Steady states in the twin-well potential oscillator: Computer simulations and approximate analytical studies," *Chaos: An Interdisciplinary Journal of Nonlinear Science,* vol. 3, pp. 375-385, 1993.

[191] R. K. Narisettia, M. Ruzzenea and M. J. Leamy, "Study of wave propagation in strongly nonlinear periodic lattices using a harmonic balance approach," *Wave Motion,* vol. 49, pp. 394-410, 2012.

[192] A. Marathe and A. Chatterjee, "Wave attenuation in nonlinear periodic structures using harmonic balance and multiple scales," *Journal of Sound and Vibration,* vol. 289, pp. 871-888, 2006.

[193] Z. Wu, R. L. Harne and K. W. Wang, "Exploring a modular adaptive metastructure concept inspired by muscle’s cross-bridge," *Journal of Intelligent Material Systems and Structures,* vol. 27, pp. 1189-1202, 2016.

[194] R. L. Harne, Z. Wu and K. W. Wang, "Designing and harnessing the metastable states of a modular metastructure for programmable mechanical properties adaptation," *Journal of Mechanical Design,* vol. 138, p. 021402, 2015.

[195] B. Yousefzadeh and A. S. Phani, "Energy transmission in finite dissipative nonlinear periodic structures from excitation within a stop band," *Journal of Sound and Vibration,* vol. 354, pp. 180-195, 2015.

[196] S. B. Yamgoué, S. Morfu and P. Marquié, "Noise effects on gap wave propagation in a nonlinear discrete LC transmission line," *Physical review E,* vol. 75, p. 036211, 2007.

[197] X. Fang, J. Wen, J. Yin, D. Yu and Y. Xiao, "Broadband and tunable one-dimensional strongly nonlinear acoustic metamaterials: Theoretical study," *Physical Review E,* vol. 94, p. 052206, 2016.

[198] Z. Wu, Y. Zheng and K. W. Wang, "Metastable modular metastructures for on-demand reconfiguration of band structures and nonreciprocal wave propagation," *Physical Review E,* vol. 97, p. 022209, 2018.

[199] R. L. Harne, M. Thota and K. Wang, "Concise and high-fidelity predictive criteria for maximizing performance and robustness of bistable energy harvesters," *Applied Physics Letters,* vol. 102, no. 5, p. 053903, 2013.

[200] Z. Wu, L. R. Harne and K. Wang, "Energy harvester synthesis via coupled linear-bistable system with multistable dynamics," *Journal of Applied Mechanics,* vol. 81, no. 6, p. 061005, 2014.

[201] D. Mead, "Wave propagation in continuous periodic structures: research contributions from southampton," *Journal of Sound and Vibration,* vol. 190, no. 3, pp. 495-524, 1996.

[202] T. Butlin and R. Langley, "An efficient model of drillstring dynamics," *Journal of Sound and Vibration,* vol. 356, pp. 100-123, 2015.

[203] R. Khajehtourian and M. Hussein, "Dispersion characteristics of a nonlinear elastic metamaterial," *AIP Advances,* vol. 4, p. 124308, 2014.

[204] J. Summers, "Variable-coefficient harmonic balance for periodically forced nonlinear oscillators," *Nonlinear Dynamics,* vol. 7, pp. 11-35, 1995.

[205] G. R. Itovich and J. L. Moiola, "On period doubling bifurcations of cycles and the harmonic balance method," *Chaos, Solitons and Fractals,* vol. 27, p. 647–665, 2006.

[206] M. Guskov and F. Thouverez, "Harmonic balance-based approach for quasi-periodic motions and stability analysis," *Journal of Vibration and Acoustics,* vol. 134, p. 031003, 2012.

[207] T. Detroux, L. Renson, L. Masset and G. Kerschen, "The harmonic balance method for bifurcation analysis of large-scale nonlinear mechanical systems," *Computer Methods in Applied Mechanics and Engineering,* vol. 296, pp. 18-38, 2015.

[208] X. Fang, J. Wen, B. Bonello, J. Yin and D. Yu, "Wave propagation in one-dimensional nonlinear acoustic," *New Journal of Physics,* vol. 19, p. 053007, 2017.

[209] S. Ahmed, Z. Ounaies and M. Frecker, "Investigating the performance and properties of dielectric elastomer actuators as a potential means to actuate origami structures," *Smart Materials and Structures,* vol. 23, no. 9, p. 094003, 2014.

[210] F. Carpi, C. Salaris and D. D. Rossi, "Folded dielectric elastomer actuators," *Smart Materials and Structures ,* vol. 16, pp. S300 - S305, 2007.

[211] A. O'Halloran, F. O'Malley and P. McHugh, "A review on dielectric elastomer actuators, technology, applications, and challenges," *Journal of applied physics,* vol. 104, p. 071101, 2008.

[212] J. Ryu, M. D'Amato, X. Cui, K. N. Long, H. Jerry Qi and M. L. Dunn, "Photo-origami—Bending and folding polymers with light," *Applied Physics Letters,* vol. 100, no. 16, p. 161908, 2012.

[213] Y. Liu, J. K. Boyles, J. Genzer and M. D. Dickey, "Self-folding of polymer sheets using local light absorption," *Soft Matter,* vol. 8, no. 6, p. 1764–1769, 2012.

[214] M. A. C. Stuart, W. T. S. Huck, J. Genzer, M. Müller, C. Ober, M. Stamm, G. B. Sukhorukov, I. Szleifer, V. V. Tsukruk, M. Urban, F. Winnik, S. Zauscher, I. Luzinov and S. Minko, "Emerging applications of stimuli-responsive polymer materials," *Nature Materials,* vol. 9, pp. 101-113, 2010.

[215] F.-X. Coudert, "Responsive metal-organic frameworks and framework materials: Under pressure, taking the heat, in the spotlight, with friends," *Chemistry of Materials,* vol. 27, pp. 1905-1916, 2015.

[216] M. Piñeirua, J. Bico and B. Roman, "Capillary origami controlled by an electric field," *Soft Matter,* vol. 6, no. 18, p. 4491, 2010.

[217] S. M. Felton, M. T. Tolley, B. Shin, C. D. Onal, E. D. Demaine, D. Rus and R. J. Wood, "Self-folding with shape memory composites," *Soft Matter,* vol. 9, no. 32, p. 7688, 2013.

[218] J. Thévenot, H. Oliveira, O. Sandre and S. Lecommandoux, "Magnetic responsive polymer composite materials," *Chemical Society Reviews*, vol. 42, pp. 7099-7166, 2013.

[219] S. Zhao and A. Erturk, "Deterministic and band-limited stochastic energy harvesting from uniaxial excitation of a multilayer piezoelectric stack," *Sensors and Actuators A: Physical*, vol. 214, pp. 58-65, 2014.

[220] D. Meimukhin, N. Cohen and I. Bucher, "On the advantage of a bistable energy harvesting oscillator under bandlimited stochastic excitation," *Journal of Intelligent Material Systems and Structures*, vol. 24, no. 14, pp. 1736-1746, 2013.